Cranfield University

Marco Luigi Longana

Design, Modelling and Testing of a Novel Energy Harvesting Device

School of Applied Sciences

MSc by Research in Microsystems and Nanotechnology

Cranfield University

School of Applied Sciences

MSc by Research Thesis

September 2009

Marco Luigi Longana

Design, Modelling and Testing of a Novel Energy Harvesting Device

Supervisors: Dr. Meiling Zhu and Dr. James Njuguna

Academic Year: 2008 - 2009

This thesis is submitted in partial fulfilment of the requirements for the degree of MSc by Research in Microsystems and Nanotechnology
(NB. This section can be removed if the award of the degree is based solely on examination of the thesis)

Abstract

This work is a feasibility study to develop a novel energy harvesting device. Energy harvesting devices capture energy in various forms from the surrounding and transform it into usable electrical energy. These devices do not require any refuelling or recharging and are virtually a never ending source of energy. The energy harvesting devices rely on different mechanisms of energy conversion, depending on the energy source. This work focuses on conversion of mechanical energy from vibrations into electric energy using piezoelectric materials. Most of the existing devices are shaped like a cantilever beam, thus limiting the tunability to a single resonance frequency. It is believed that by modifying the geometry of the energy harvesting device and applying a pre-load to the active material (piezoelectric), a variable tunability can be achieved. Also, the application of an axial compressive pre-load helps to further increase the power output of the device. Therefore, in this present work, the performance of a simply supported beam shaped energy harvesting device is investigated both numerically and experimentally.

For the numerical analyses finite element simulations are carried out using ANSYS. An electro-mechanical model of the simply supported beam has been developed through a series of approaching models with increasing complexity, starting from an analytical solution. The final three-dimensional model was used as a base to create a model of the beam that has been used during the experimental tests. Shape optimization studies were carried out on this finite element model to analyse the power output of the device. It has been observed, through pre-stressed modal analyses, that the axial pre-load decreases the resonance frequency of the beam, thereby giving the beam the ability to be tuned. Also,it has been observed that an optimisation of the beam footprint shape can increase the power output by almost 40%.

The experimental work focussed on the investigation of the harmonic behaviour of the simply supported beam under different pre-load conditions. It was observed that the experimental results were in disagreement with the finite element simulations and also with the reference literature. The disagreement was identified to be due to the hinge design that does not ensure the alignment of the two tips of the beam and therefore the application of a perfectly axial pre-load.

From the work presented here it emerges that the possibility to develop a simply supported beam shaped energy harvesting device that rely on the application of an axial pre-load to obtain tunability and an higher power output is promising. The finite element simulations gave good results on the beam behaviour and on the possibility to further increase its output by optimising the shape of its footprint. The experimental work allowed to identify the hinge design as a problem area to design a profitable device.

Acknowledgements

I want to thank my supervisors Dr. Meiling Zhu and Dr. James Njuguna for their help and guidance.

I also wish to thank Emma Worthington and all the office mate, for the helpful advices, and all the technicians who helped me all through this work.

I gratefully acknowledge the financial support from the Cranfield Innovative Manufacturing Research Centre via EPSRC entitled Design and Manufacturing of a Novel EHDs for Self Powered Sensors and ICT Applications (IMRC-137).

This thesis is written with LaTeX.

Contents

1 Introduction **1**

1.1 Thesis background 1

1.2 Aims of the thesis 2

1.3 Objectives 2

1.4 Outline of the thesis structure 3

2 Literature Review **4**

2.1 Introduction 5

2.1.1 Sources of energy and energy transducer 5

2.2 Piezoelectric energy harvesting devices 8

2.2.1 Working principles 8

2.2.2 Available devices 11

2.2.3 Background of the proposed device 16

2.3 Conclusions 19

3 Methodology **21**

3.1 Preliminary dimensioning and conceptual design 22

3.1.1 Material selection 23

3.1.2 Mixture law 24

3.1.3 Buckling analysis 26

3.1.4 Critical buckling stress 28

3.1.5 Modal analysis 29

3.2 Finite element modelling 29

3.3 Experimental work 30

4 Finite Element Modelling **32**
4.1 Approaching models . . . 33
4.1.1 Models descriptions . . . 34
4.1.2 Analyses description . . . 35
4.1.3 Results . . . 38
4.2 Final model description . . . 52
4.2.1 Used elements . . . 53
4.2.2 Material data . . . 53
4.2.3 Meshing . . . 55
4.2.4 Voltage output calculation . . . 55
4.2.5 Analyses description . . . 56
4.3 Testing beam model . . . 56
4.3.1 Analysis results . . . 58
4.3.2 Considerations about the testing beam modelling . . . 68
4.4 Beam footprint optimisation . . . 68
4.4.1 Geometry . . . 69
4.4.2 Analysis results . . . 70

5 Experimental Work **81**
5.1 Beam manufacture process . . . 82
5.2 Beam electromechanical response test . . . 86
5.2.1 General test bed layout . . . 86
5.2.2 Testing procedures . . . 91
5.2.3 Test results . . . 92
5.3 Snap through experiments . . . 98
5.3.1 Beam dimensions . . . 99
5.3.2 General test-bed layout . . . 100
5.3.3 Testing procedure . . . 105
5.3.4 Test results . . . 105

6 Discussion **108**
6.1 Finite element modelling results . . . 109
6.1.1 Approaching models . . . 109

6.1.2 Testing beam model 109
6.1.3 Shape optimisation analysis 112
6.2 Experimental work 116
6.2.1 Beam manufacture process 116
6.2.2 Beam electromechanical response test 117
6.2.3 Snap through experiments 121
6.2.4 Testing jig design 122
6.3 Finite elements vs experimental results 123
6.3.1 Beam response 124

7 Conclusions and Suggestions for Further Work 126
7.1 Conclusions 127
7.1.1 Axial pre-load effect 127
7.1.2 Shape optimisation 128
7.1.3 Testing jig 128
7.1.4 Feasibility 128
7.2 Suggestions for further work 129
7.2.1 Finite element modelling 129
7.2.2 Experimental work 129

Appendices 136

A ANSYS models 136
A.1 BEAM3 model 136
A.2 SHELL93 model 138
A.3 SHELL91 model 140
A.4 SOLID45 model 143
A.5 Layered SOLID45 and SOLID5 model 145
A.6 Testing beam model 150
A.7 Beam footprint optimization model 157

B Jig Drawings 164

List of Figures

2.1 Energy harvesting device scheme 6
2.2 Direct and converse piezoelectric effect [24] 9
2.3 Conventional direction in a piezoelectric material 10
2.4 Beam shapes and connections: a) bimorph in series b) bimorph in parallel c) unimorph 14

3.1 Beam dimensions 22
3.2 Euler buckling shapes depending on the boundary conditions: 1) K = 2 2) K = 0.5 3) K = 0.6999 4) K = 1 27
3.3 Buckling of a simply supported column 28

4.1 Developing of the Finite Element model 33
4.2 Results for the buckling analysis 38
4.3 Results for the modal analysis 40
4.4 Mode shapes for BEAM3 and SHELL91 models 43
4.5 X and Z displacements. 44
4.6 Results of the pre-stressed modal analysis for BEAM3 model . 46
4.7 Results of the pre-stressed modal analysis for SHELL93 model 47
4.8 Results of the pre-stressed modal analysis for SOLID45 model 48
4.9 Results of the pre-stressed modal analysis for SHELL91 model 49
4.10 Results of the pre-stressed modal analysis for SOLID45 & SOLID5 model 50
4.11 First resonance frequency at different pre-stress 51
4.12 Results for the harmonic analysis 52
4.13 Sketch of the electrical connection of the beam 56

4.14 Testing Beam 57
4.15 Finite element model of the testing beam 57
4.16 Results for the buckling analysis 58
4.17 Results for the modal analysis 59
4.18 Mode shapes for the testing beam model 60
4.19 Static displacement 61
4.20 Von Mises stress distribution 62
4.21 Results of the pre-stressed modal analysis without extra mass 63
4.22 Results of the pre-stressed modal analysis with 13 g extra mass 64
4.23 Results of the pre-stressed modal analysis with 22 g extra mass 65
4.24 First resonance frequency at different pre-stress 66
4.25 Results for the harmonic analysis 66
4.26 Results for the harmonic analysis 67
4.27 Beam footprints plane views: a) rectangular footprint b) lozenge-shaped, hexagonal, footprint 69
4.28 Results of the buckling analysis 71
4.29 Results of the modal analysis 72
4.30 Mode shapes for for the 20-20 mm and the 2-38 mm footprint 73
4.31 Static displacement for the 20 - 20 mm footprint shape 74
4.32 Static displacement for the 2 - 38 mm footprint shape 76
4.33 Von Mises stress distribution for the 20 - 20 mm footprint shape 77
4.34 Von Mises stress distribution for the 2 - 38 mm footprint shape 78
4.35 Results for the harmonic analysis 79
4.36 Results for the harmonic analysis 79

5.1 Materials used to realize the bimorph beam 82
5.2 Gluing of the piezoelectric material to the substrate with silver epoxy 83
5.3 The materials stack ready for curing 84
5.4 Gluing of the stiffeners with Araldite 85
5.5 Cutting of the laminate with a meter saw, the clamping absorbs the vibrations 86
5.6 Diagram of the experimental set-up 87

5.7 Experimental set-up 88
5.8 Testing Jig 89
5.9 Mass profile: designed to reduce the contasct area between beam and mass 90
5.10 Recorded Results without extra mass 93
5.11 Post-processed results without extra mass 94
5.12 Recorded Results with 13g of extra mass 95
5.13 Post-processed results with 13g of extra mass 95
5.14 Recorded Results with 22g of extra mass 96
5.15 Post-processed results with 22g of extra mass 97
5.16 System acceleration response 98
5.17 Extra 30 g mass added to the centre of the beam. The contact area is minimised to reduced the stiffened area. 100
5.18 Diagram of the experimental set-up 101
5.19 Test set up for the snap trough experiment. One accelerometer is fitted on the testing jig and one on the inertial mass glued to the centre of the beam. 102
5.20 Hinged constrain 103
5.21 Fixed constrain 104
5.22 Resonance frequency of the simply supported beam versus the beam tip displacement for the different beam size 106
5.23 Resonance frequency of the fixed-fixed beam versus the beam tip displacement for the different beam size 106

6.1 electrical connections of the beam 111
6.2 Power output calculated from the harmonic analysis results for the different beam shapes with R = R_{opt} 115
6.3 Power output calculated from the harmonic analysis results for the different beam shapes with R = 5 $k\Omega$ 115
6.4 Power output peaks and trend line for optimised and constant resistance 116
6.5 Natural Frequency of the beam versus the beam tip displacement with different extra masses 117

6.6 Beam output versus the beam tip displacement with different extra masses 118
6.7 Schematic comparison of the hinge design: a) first attempt b) modified design 123

B.1 Connection plate 164
B.2 Short bearing support column 165
B.3 Long bearing support column 165
B.4 Beam support rod 166
B.5 Testing jig assembly drawing 166
B.6 Mass drawing 167

List of Tables

2.1 Acceleration magnitude and frequency of fundamental vibration from [21] 7
2.2 Comparison of the relative merits of three primary types of converters from [21] 8

3.1 Characteristics of PSI-5H4E 24

4.1 Results for the buckling analysis 39
4.2 Results for the modal analysis 41
4.3 Results of the large displacement static analysis 45
4.4 Results of the pre-stressed modal analysis for BEAM3 model . 46
4.5 Results of the pre-stressed modal analysis for SHELL93 model 47
4.6 Results of the pre-stressed modal analysis for SOLID45 model 48
4.7 Results of the pre-stressed modal analysis for SHELL91 model 49
4.8 Results of the pre-stressed modal analysis for SOLID45 & SOLID5 model 50
4.9 Results for the buckling analysis 58
4.10 Results for the modal analysis 59
4.11 Results of the large displacement static analysis 61
4.12 Results of the pre-stressed modal analysis without extra mass 63
4.13 Results of the pre-stressed modal analysis with 13 g extra mass 64
4.14 Results of the pre-stressed modal analysis with 22 g extra mass 65
4.15 Results of the harmonic analysis 67
4.16 Results of the harmonic analysis 68
4.17 Measures of tip and centre width. 70

4.18 Results of the buckling analysis 70
4.19 Results of the modal analysis 71
4.20 Results of the large displacement static analysis 75
4.21 Results of the harmonic analysis 80

5.1 Results of the test without extra mass 94
5.2 Results of the test with 13g of extra mass 96
5.3 Results of the test with 22g of extra mass 97
5.4 Dimensions of the beam for the snap through test 99

6.1 Testing beam model outputs calculated from the harmonic analysis results 112
6.2 Shape optimisation models outputs calculated from the harmonic analysis results 114
6.3 Beam without extra mass outputs calculated from the electromechanical response test results 120
6.4 Beam with 13 g of extra mass outputs calculated from the electromechanical response test results 120
6.5 Beam with 22 g of outputs calculated from the electromechanical response test results 121
6.6 First resonance frequency 124

Chapter 1

Introduction

1.1 Thesis background

The new low-power-consumption electronic technologies lead to a significant reduction in the power consumption of electronic devices that can now work with only a few thousandths of Watts. This amount of power can be obtained by collecting energy, in various forms, from the environment and transforming it into a usable source of power, this process is called *energy harvesting*.

Almost all the available portable electronic devices are powered by batteries that put a time limit to the devices' usability. A battery powered device is dependent on external power sources if the batteries need to be recharged. On the other hand, if the batteries need to be replaced the devices have to be stopped for periodic servicing. Also, the disposal of used batteries raise the issue of highly pollutant elements. For inaccessible devices like implantable medical devices or embedded sensors, it is often very difficult to attend to regular maintenance without invasive procedures. In transport industry the availability of self powered devices will bring about significant weight and cost reduction by eliminating batteries and wires. With the development of wireless data transmission, the possibility to have sensors that can harvest environmental energy and transform it into usable power will allow the use of purely wireless and virtually everlasting sensors.

Therefore, the development of new energy harvesting devices which are able to convert the energy collected from the environment more efficiently and generate higher power output can contribute immensely to modern technology.

1.2 Aims of the thesis

The aim of this thesis is to design, model, manufacture and test a prototype of a novel energy harvesting device. This device will use piezoelectric materials to convert vibration-based environmental energy to usable electric energy. The prototype, realized in the macro scale, is a simply supported bimorph beam. The output of this device, when fully developed, is expected to be sufficient to supply energy to sensors, or to recharge batteries, opening the way to fully wireless sensing systems. In this thesis the device will be modelled and tested. Also, consideration about its feasibility and suggestions for further studies for its optimisation will be presented.

1.3 Objectives

This thesis is a feasibility study. The objective is to design a device that can be used as a profitable source of energy for low power consumption applications. The novelty of the design consists in the exploitation of an axial pre-load to achieve the tunability and a higher power output of the device. This concept will be investigated with finite element simulations and experimental work. It is also believed that a shape optimisation can lead to a further increase of the power output, this hypothesis will be looked into with finite element simulations.

1.4 Outline of the thesis structure

The thesis begins with a literature review in chapter 2 about the working principles of energy harvesting devices. A survey of the available piezoelectric based energy harvesting devices is then carried in order to identify the conceptual foundations on which the present design of the device can be based.

Chapter 3 describes the methodology used during this research work. The preliminary analytical design is presented in detail. Also, the chapter presents an overview of the finite element modelling and the experimental work.

Chapter 4 describes the development of the finite element model of the energy harvesting device through different models with increasing steps of complexity. Furthermore, it presents the results of the finite elements simulations for the model of the testing beam and for the beam footprint optimisation model.

Chapter 5 describes the experimental part of this research work. The production of the beam is detailed in this chapter as well as the development of the test-bed and different test procedures. The test results are also presented in this chapter.

Chapter 6 reports the discussion about the results of the finite element simulations and of the experimental work.

Chapter 7 concludes the work with considerations about the feasibility of this energy harvesting device and presents the design requirements of a bimorph, simply supported bi-stable beam based energy harvesting device.

Chapter 2

Literature Review

This chapter gives an introduction to the principles of energy harvesting, followed by an overview of the energy harvesting devices described in literature, and concludes with the definition of the practical and theoretical basis of the new concepts used to design the energy harvesting device presented here.

2.1 Introduction

Energy harvesting devices (also known as energy scavenging devices) capture energy, in various forms, from their surroundings and transform it into usable electric energy. The energy harvesting devices do not require any refuelling or recharging and are a virtually never ending source of energy. For this reason the interest in these devices has improved in the last years for several industrial and every day life applications:

1. Wireless self powered sensors that could be placed in remote locations, contaminated areas and even embedded into materials without having to consider issues such as cabling or battery replacing.

2. The implantable medical devices will not need an energy supply from batteries but will harvest the energy needed for their functioning from the patient himself.

3. The opportunity to auto recharge the batteries of electronic portable devices while using them will bring about truly wireless systems.

2.1.1 Sources of energy and energy transducer

An energy harvesting device is composed of three main parts as also shown in Figure 2.1:

1. the *generator* that converts the energy harvested from the environment into electrical energy;

2. the *conditioning circuitry* that increase and regulates the generated voltage;

3. the *storage element* that collect and store the power. The storage element can be replaced by a user.

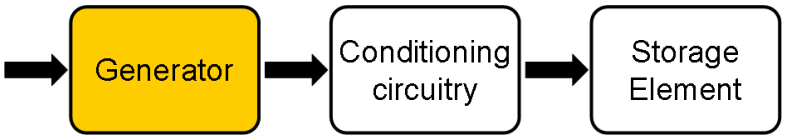

Figure 2.1: Energy harvesting device scheme

This work is centred on the generator part of the energy harvesting device.

There are many micro-generators for energy harvesting and their working principles depend on the sources of energy available:

1. Mechanical Energy: from sources such as mechanical stress, strain and vibration.
2. Light Energy: photo-voltaic cells can transform ambient light into electricity.
3. Thermal Energy: the Peltier-Seebeck effect is exploited to generate electricity from a temperature gradient between opposite segments of a conducing material.
4. Electromagnetic Energy: a particular kind of rectifying antenna, called rectenna, is used to convert microwave energy into DC electricity.
5. Human Body: the energy harvested from the human body can be classified in two different categories:
   (a) actively harvested energy: when the user has to intentionally perform a specific task or work to supply the energy source to the energy harvesting device
   (b) passively harvested energy: when the energy source is provided by the everyday activities of the user

In this research work the chosen energy source is mechanical energy in the form of vibration. This kind of environmental solicitation can be found in almost any industrial or transport application. Roundy et al. [21] made a study on the potential of environmental vibration as a potential power source.

The authors present a survey on the possible sources of vibration, measuring a variety of commonly occurring vibrations. Two important characteristics common to virtually all of the sources measured were identified:

1. there is a large peak in magnitude somewhere below 200 Hz, which can be referred to as the fundamental mode;

2. the acceleration spectrum is relatively flat with frequency

Table 2.1 presents the results obtained by their survey, showing acceleration magnitude and frequency of fundamental vibration mode from various sources.

Table 2.1: Acceleration magnitude and frequency of fundamental vibration from [21]

Vibration Sources	A(m/s^2)	f(Hz)
Car engine compartment	12	200
Base of 3 axis machine tool	10	70
Blender casing	6.4	121
Clothes dryer	3.5	121
Person nervously tapping their heel	3	1
Car instrument panel	3	13
Door frame just after door closes	3	125
Small microwave oven	2.5	121
HVAC vents in office building	0.2-1.5	60
Windows next to a busy road	0.7	100
CD on notebook computer	0.6	75
Second story floor of busy office	0.2	100

The authors conclude that the vibration that could have an interest for energy harvesting designers have a fundamental mode in the order of 100 Hz, and maximum acceleration magnitudes in the range of 0.5 to 5 m/s^2.

In the same article the three main ‘vibration to electricity‘ conversion mechanisms are investigated and compared as shown in Table 2.2.

Table 2.2: Comparison of the relative merits of three primary types of converters from [21]

Mechanism	Advantages	Disadvantages
Piezoelectric	No voltage source needed Output voltage is 38 V	More difficult to integrate in microsystems
Electrostatic	Easier to integrate in microsystems	Separate voltage source needed Practical difficulties
Electromagnetic	No voltage source needed	Output voltage is 0.1-0.2 V

The authors conclude that piezoelectric converters, beside the advantages already underlined in Table 2.2, have a higher energy conversion potentiality than electrostatic and electromagnetic converters.

In their review article, Beeby et al. [4] present the state of the art in vibration energy harvesting for wireless self powered microsystems considering energy harvesting devices that base their transduction mechanisms on piezoelectricity, electromagnetism and electrostaticy. The authors conclude that piezoelectric converters offer the simplest approach for energy harvesting devices: the electroded piezoelectric material can directly convert the structural vibration into a relatively high voltage output and low electrical current. From a mechanical point of view they don't require complex geometries or numerous additional components, and are the simplest to fabricate. This devices are quite adaptive to different application environments due to the wide range of piezoelectric materials available.

2.2 Piezoelectric energy harvesting devices

2.2.1 Working principles

When a piezoelectric material (notably crystals and certain ceramics) is subjected to a mechanical stress, a charge separation appears across the crystal

lattice. If the material is not short circuited, the applied charge induces a voltage across it. This phenomenon is known as direct piezoelectric effect. Equally a converse piezoelectric effect can be possible: if a voltage is applied across the crystal lattice, a strain or a mechanical stress, depending on how the material is constrained, appears in the material.

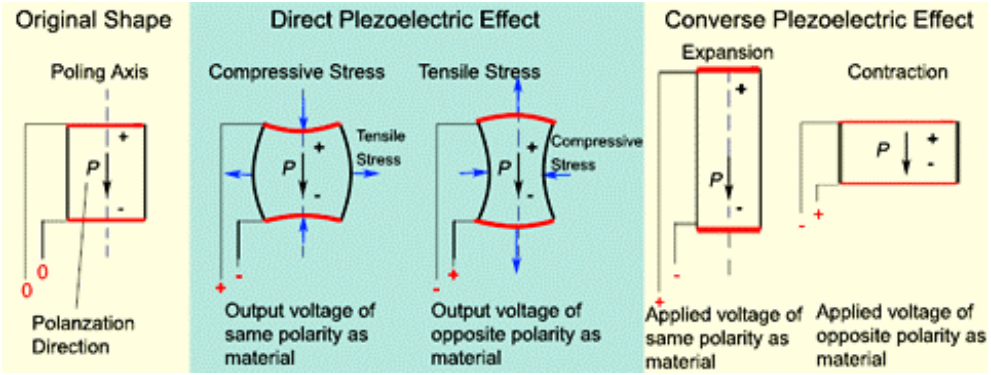

Figure 2.2: Direct and converse piezoelectric effect [24]

In the crystal lattice of piezoelectric material the positive and negative electrical charges are separated but symmetrically distributed, so that the crystal is overall electrically neutral. Each of these charged sites forms an electric dipole, and dipoles near each other tend to be aligned in regions called Weiss domains. These domains are usually randomly oriented, but they can be aligned by applying a strong electric field across the material at elevated temperatures. This process is known as *poling*.

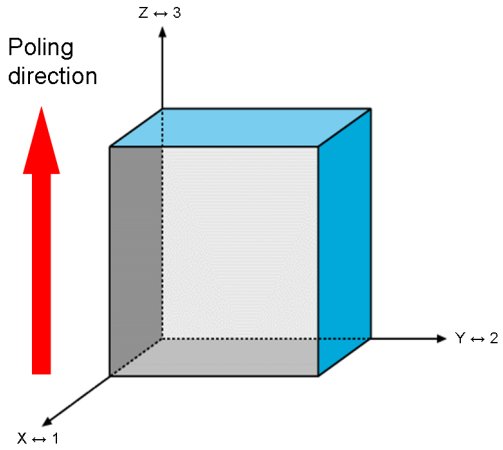

Figure 2.3: Conventional direction in a piezoelectric material

In a Cartesian three dimensional space, as shown in Figure 2.3, labelling x, y and z axes as 1, 2 and 3 axes, and assuming that the piezoelectric material is poled in direction 3 the mechanical strain is usually applied in direction 3 or direction 1. If the mechanical solicitation is parallel to the poling the piezoelectric material is said to be working in 33 mode, similarly if the mechanical solicitation is perpendicular to the poling the piezoelectric material is said to be working in 31 mode.

In piezoelectric materials the electrical and mechanical behaviour are directly related as described by equations 2.2 and 2.1 [26]:

$$\{S\} = [s^E]\{T\} + [d^t]\{E\} \tag{2.1}$$

$$\{D\} = [d]\{T\} + [\epsilon^T]\{E\} \tag{2.2}$$

where S is the mechanical strain, D is the electric charge density displacement, T is the mechanical stress, E is electric field strength, $[\epsilon^T]$ is the permittivity in a constant or zero stress field, $[s^E]$ is the compliance in a constant or zero electric field and finally d and d^t are the matrix for direct and inverse piezoelectric effect.

The coupling between the mechanical and electrical behaviour of piezoelectric materials is the foundation of the energy harvesting devices.

Currently the piezoelectric materials suitable for energy harvesting purposes are:

1. Lead Zirconate Titanate, a piezo-ceramic, known as PZT. PZT is the most commonly used energy harvesting material. However the piezo-ceramic's fragility causes limitations in the strain or stress bearable by the material. Moreover the piezo-ceramics, when subjected to high frequency cyclic loading, are prone to fatigue crack growth.

2. Polyvinylidenefluoride or PVDF, a piezoelectric polymer that exhibits considerable flexibility when compared to PZT.

3. Piezo-fibres: a fibre based piezoelectric material consisting of PZT fibres of various diameters (15, 45, 120, and 250 μm) aligned, laminated, and moulded in an epoxy resin.

2.2.2 Available devices

A good amount of review articles are available in the literature about the energy harvesting technology, such as, in chronological order from the newest to the oldest:

1. *Overview of the Modern State of the Vibration Energy Harvesting Devices* from Pereyma [18];

2. *A review of power harvesting using piezoelectric materials (2003-2006)* from Anton and Sodano [2];

3. *Energy harvesting vibration sources for microsystems applications* form Beeby et al. [4];

4. *A Review of Power Harvesting from Vibration using Piezoelectric Materials* [23] and *Comparison of Piezoelectric Energy Harvesting Devices for Recharging Batteries* [22] from Sodano et al. ;

5. *Review of energy harvesting techniques and applications for microelectronics* from Mateu and Moll[12].

One way to classify the energy harvesting devices relies on the working mode:

1. 33 mode: the force is applied in the same direction as the poling direction;

2. 31 mode: the force is applied perpendicularly to the poling direction.

Although the 31 mode yields a lower coupling coefficient, k, than the 33 mode, it is the one most commonly used in energy harvesting devices. An explanation for this can be found in the work of Baker et al. [3]: even though the 33 coupling mode is three times more efficient than the 31 mode at converting the strain into energy, inducing strain in this mode is difficult. Two different energy harvesting device were modelled, one relying on 33 mode and one on 31 mode, keeping equal the volume of the piezoelectric material, the volume of the device and the force applied, to compare the two working modes. From the calculation, the power output of the 31 mode device was two orders of magnitude bigger than the 33 mode device. The authors conclude that the 31 mode is more suitable for small force and low vibration level environments. At the same time a device that works in 31 mode has a less rigid structure: this makes it easier to match the resonance frequency of the device with the environmental vibration. The 33 mode devices are more suitable for high force environments: they are used for impact coupled devices, thank to their robustness and efficiency. The goal of this research work is to create a device that can harvest energy from environmental vibrations with a fundamental mode lower than 200 Hz and maximum acceleration magnitudes in the range of 0.5 to 5 m/s^2. For this reason the devices that use 33 mode will not be taken into consideration any further.

Another way to classify the energy harvesting devices is the shape of the transducer part:

1. circular

2. beam shaped:

   (a) cantilever beam;

   (b) simply supported;

The circularly shaped energy harvesting systems were first studied by Ericka et al. [6] to harvest electrical energy from mechanical vibrations in a dynamic environment thanks to a circular piezoelectric membrane transducer. The transducer used was an unimorph membrane consisting of a circular brass layer with a slightly smaller circular PZT layer bonded to its surface. The experimental results of this study show that the power harvested from this device can be increased by operating at its resonance frequency, by subjecting the device to high accelerations, and especially by matching the electrical load resistance.
The shape of the diaphragm was also studied by Minazara et al. [13] using a generator built with a piezoelectric unimorph diaphragm structure operating in flexural mode.
A further improvement in the usage of circularly shaped sensors for energy harvesting was given by Kim et al. [8] introducing the concept of 'cymbal', consisting of a piezoelectric ceramic disk sandwiched between two concave metal end caps. The cymbal configuration optimises the efficiency of the power harvesting, distributing the stress evenly throughout the piezo-ceramic material, allowing a larger amount of the material to actively generate energy. Experimental results show that cymbal transducers are capable of withstanding high force applications while producing usable power.
These kind of transducers offer an interesting model for energy harvesting devices, but they are not interesting for the purposes of this research work because of their limited possibility to be actively tuned on the system's frequencies.

The beam shapes can present two different configurations:

1. bimorph: two bonded piezoelectric layers, often with a substrate between them, in bending mode, and connected in two different ways:

(a) series (Figure 2.4 a));

(b) parallel (Figure 2.4 b));

2. unimorph: a single piezoelectric layer in bending mode (Figure 2.4 c)).

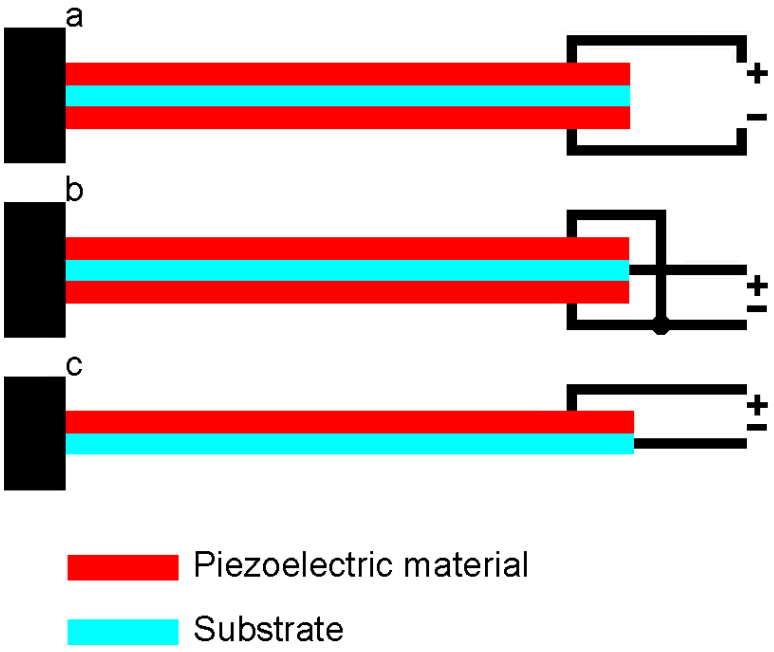

Figure 2.4: Beam shapes and connections:
a) bimorph in series
b) bimorph in parallel
c) unimorph

A comparison between the different beam configuration and connection is presented by Ng and Liao [16] [17]:

1. the unimorph generated the highest power under low load resistances and excitation frequencies.

2. the bimorph connected in parallel had the highest power output under medium load resistances and frequencies

3. the bimorph connected in series produced the greatest power under high load resistances and frequencies

Mateu [11] analyses several bending beam structures suitable for energy harvesting and obtains the resultant strain for each type as a function of their geometrical parameters and material properties:

1. a homogeneous bimorph without a substrate,
2. a heterogeneous bimorph bonded to an elastic substrate,
3. a heterogeneous unimorph bonded to an elastic substrate.

It was determined that, for harvesters with the same piezoelectric material volume, the heterogeneous unimorph generated the most power because the piezoelectric material was furthest away from the neutral bending axis, thus causing higher strains in the active material and greater energy generation.

The configuration that is mainly investigated for energy harvesting is the cantilever beam. In their work Roundy and Wright [20] put the bases for the design of energy harvesting devices that rely on piezoelectric materials. In their paper they discuss the modelling, design, and optimisation of a piezoelectric generator based on a two layer bending element. The energy harvesting device is firstly studied with an analytical model, based on the electrical equivalent circuit to describe the bimorph beam. The model, in addition to providing intuitive design insight, has been used as the basis for design optimisation and provides some design intuition:

1. The system should be designed with its frequency tuned with the dominant driving frequency of the target vibrations.
2. The power output is proportional to the proof mass attached to the system. Therefore the proof mass optimisation process must take into account the resonance frequency and strain limits.
3. Power output is inversely related to the driving and resonance frequency. Therefore, designing for lower frequency peaks in the vibration spectrum is preferred as long as they have equivalent or higher acceleration magnitude than higher frequency peaks.

4. The energy removed by the electrical load appears to have a damping effect on the mechanical system. The load can be designed such that the level of effective electrically induced damping maximizes power transfer to the load.

A different approach to the modelling of the bimorph beam, based on a combination of the Euler-Bernoulli beam theory and the Timoshenko beam equations, is proposed by Ajitsaria et al [1]. The calculations employed for the deflection of a thermal bimorph proposed by Timoshenko are used for the static analysis of a piezoelectric cantilever beam. The bimorph is modelled as a piezoelectric heterogeneous bimorph, where two piezoelectric layers are bonded on both sides of a purely elastic layer. The principle is based on the strain compatibility between three cantilever beams joined along the bending axis. Due to forces applied by one or all of the layers, the deflection of the three layer structure is derived from a static equilibrium state. On the other hand, Euler-Bernoulli beam theory describes the relationship between the deformed structure and the applied forces. The combination of the two approaches leads to a mathematical formula for the produced voltage.

From the literature survey the main research topic under the structural point of view is the footprint of the cantilever beam. An optimisation of the shape can take to a more uniform and effective stress distribution along the beam and so to a much higher energy output [3].

2.2.3 Background of the proposed device

The cantilever beam configuration is not the only one available for use in energy harvesting device. In their work, Mossi et al. [14] studied a thin unimorph pre-stressed bender. This sensor consists of a top metal layer, a PZT layer and a metal backing layer. The device is constrained through hinges to its support.

In their work Baker et al. [3] proposed a new configuration for an energy

harvesting device: a piezoelectric bimorph beam is compressed and fixed at both ends with hinged constraints. The beam is loaded up to the critical buckling load. This so called *bistable* device generates power by snapping from one stable mode to another, and a force magnification occurs due to a constant compressive force in the structure. The authors conclude that the bistable mechanism is a superior design in applications of uncertain or changing fundamental frequency because the bistable mechanism can relax the tight constraint of frequency matching, and create a more universal solution for energy harvesting devices.

The same configuration is studied by Leland and Wright [9] who use the buckling load to tune the resonance frequency of a vibrating energy harvesting device. The axial pre-load can reduce the resonance frequency of a simply supported buckled beam up to 24% and increase the coupling coefficient up to 25%. The energy harvesting device can be tuned to several working frequencies to make it always work at its optimum power output condition.

The theoretical foundation of this research work can be found in the article from Lesieture and Davis [10]. As said before, the electromechanical coupling coefficient is defined as the effectiveness with which the energy is converted from mechanical to electrical and vice versa by a piezoelectric material or by a device employing such active material. The electromechanical coupling coefficients of a piezoelectric material are multiple, corresponding to different modes of excitation and response. In the same way a device, that employs piezoelectric as active material, has a coupling coefficient, that is dependent from the material coupling factor but is also influenced by the device geometry and working principles. The device coupling coefficient is generally lower than the material coupling coefficient.
Going deeper in the analysis the author defines the coupling coefficient, in the same way for materials and devices, with a simple strain/electric field

pattern, as:

$$k^2 = \frac{e^2}{(c^E \epsilon^S + e^2)} \tag{2.3}$$

where e is the piezoelectric coefficient, c^E is the short circuit stiffness, and ϵ^S is the dielectric permittivity.
It's clear that the coupling factor can be increased if the device stiffness is reduced without affecting the capacitance. Considering the elastic stability of structures the author identifies the buckling load as a destabilizing load that has the ability to reduce the structural stiffness.
The author gives also a theoretical demonstration with simply supported bimorph piezoelectric beam: the effective lateral stiffness of the device is reduced by an axial destabilizing pre-load defined as a geometrical stiffness:

$$K_G = P \left(\frac{\pi}{L}\right)^2 \frac{L}{2} \tag{2.4}$$

Where P is the axial pre-load and L is the length of the beam.
Depending on how the axial destabilizing pre-load is treated, the coupling coefficients has two different definition:

1. when the axial destabilizing pre-load is considered as a simple reduction of the effective lateral stiffness of the device an apparent coupling coefficient is defined as:

$$k_{app}^2 = \frac{p^2}{p^2 + (K^E - K_G)C^S} \tag{2.5}$$

   where p is the piezoelectric coupling factor, K^E is the effective lateral stiffness of the device, K_G is the geometrical stiffness, and C^S is the capacitance.
   In this case it's easy to observe that if the axial destabilizing approaches the buckling load the apparent coefficient approaches the unit.

2. when the axial destabilizing pre-load is considered as a mechanical

input to the system a proper coupling factor is defined as:

$$k^2_{proper} = \frac{p^2}{p^2 \left(\frac{K^E}{K^E - K^E}\right) + (K^E - K^E)C^S} \tag{2.6}$$

This coefficient has a maximum value as

$$k^2_{proper_{MAX}} = \frac{1}{2}\left(\frac{p^2}{K^E C^S}\right)^{1/2} \tag{2.7}$$

when the axial destabilizing pre-load approaches the buckling load the coefficient is 0.

The author concludes that even at modest axial destabilizing pre-load the device coupling factor can be higher than the unloaded device coupling factor and even exceed the coupling factor of the active material.

2.3 Conclusions

From the literature survey the following guidelines are identified in order to design a state-of-the art piezoelectric energy harvesting device suitable to test the effects of the application of an axial pre-load to the active material:

- the device should be beam shaped;
- the piezoelectric material should work in the 31 mode;
- the device should be a bimorph beam with parallel connection
- the beam should be constrained at both the ends to allow the application of the pre-load;
- the device should exploit the snap-through effect of buckled beams under harmonic solicitation to:
  - allow the tuning of the device to the environmental vibration;

– increase the energy output.

The articles from Baker, Roundy and Wright [3], Leland and Wright [9] and Lesieture and Davis [10] are basis for the development of the novel energy harvesting device presented in this thesis. It has been decided to develop a device that will exploit the usage of buckled structures and snap through mechanism to control the resonance frequency of the energy harvesting device and tune it to the environmental vibration frequency. The axial buckling load will also increase the internal stresses and at the same time the energy output. Some design enhancements, such as the hinge design and inertial mass shape, will be tested. The beam footprint will be studied to understand if there is the possibility to increase the voltage and power of the device.

Further useful elements emerged from the literature review: the energy harvesting device will have to be tuned to an environmental vibration with a fundamental mode in the order of 100 Hz, and maximum acceleration magnitudes in the range of 0.5 to 5 m/s^2. This is in contrast with the results obtained by Baker et al. [3] who observed the snap through with more than 4 g of acceleration. It is believed that an improvement of the hinge design can lead to a reduction of the required acceleration.

Chapter 3

Methodology

This Chapter describes the methodology used during this research. The first section details the preliminary analytical design. Section 3.2 and 3.3 give a quick overview of the aims of finite elements modelling and of the experimental work.

3.1 Preliminary dimensioning and conceptual design

Accordingly to the conclusion of the literature review a bimorph, simply supported bi-stable beam-based energy harvesting device is designed.

The beam dimensions are chosen in order to create a slender beam big enough to use off-the-shelves materials to build the beam itself and the testing jigs.

The dimension of the beam are described in Figure 3.1

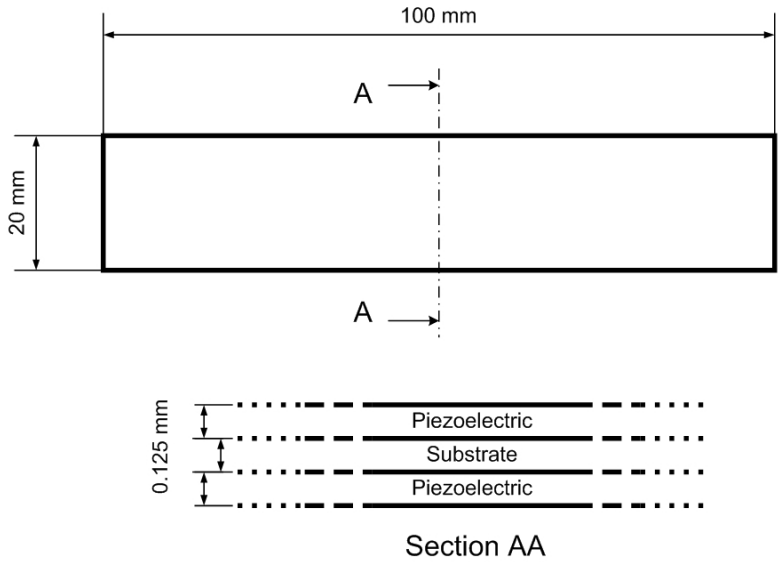

Figure 3.1: Beam dimensions

Preliminary calculations have been done to estimate the buckling load, the natural frequency and a first approximation of the stress in the beam. In order to simplify the bimorph configuration of the beam for the use in a simple analytical model the mixture law has been used to calculate a homogenized Young's modulus and density.

3.1.1 Material selection

Substrate

The characteristics required to the substrate material are:

- high mechanical strength: it has to sustain the active material and transmit to it the pre-load;
- flexibility, it must ensure that the vibration will be damped as little as possible;
- conductivity, it has to collect and conduct the current produced by the electrodes.

Accordingly to these characteristics the stainless steel AISI 316 has been chosen. This material also has good corrosion resistance characteristics and is biocompatible.

Piezoelectric Material

Several materials are currently available in the market, but their dimensions and shapes are limited. Piezo System is able to provide a sheet of piezoelectric material that could be manufactured into beams of the required shape and dimensions. The selected material is a Navy type VI lead zirconate titanate named PSI-5H4E. This material is provided in 74 mm square sheets and its characteristics are summarized in Table 3.1.

Table 3.1: Characteristics of PSI-5H4E

Property	Value	Unit
Relative dielectric constant	3800	
d_{33} coefficient	$650 \cdot 10^{-12}$	m/V
d_{31} coefficient	$-320 \cdot 10^{-12}$	m/V
g_{33} coefficient	$19 \cdot 10^{-3}$	m^2/C
g_{31} coefficient	$-9.5 \cdot 10^{-3}$	m^2/C
Coupling coefficient k_{33}	0.75	
Coupling coefficient k_{31}	0.44	
Y_1^E	$6.2 \cdot 10^{10}$	Pa
Y_3^E	$5 \cdot 10^{10}$	Pa
Mechanical Q	32	

3.1.2 Mixture law

Considering a bimorph structure like the one shown in Figure 3.1 the hypothesis of the mixture law are the following:

1. the materials are both isotropic;
2. there is perfect adhesion between the two different materials:

$$\epsilon_{TOT} = \epsilon_{SUB} = \epsilon_{PZT} \tag{3.1}$$

   where ϵ is the strain, the subscript TOT refers to the whole structure, PZT to the piezoelectric material and SUB to the substrate.

3. the materials have a linear elastic behaviour:

$$\sigma_{TOT} = E_{TOT} \cdot \epsilon_{TOT} \tag{3.2}$$

$$\sigma_{PZT} = E_{PZT} \cdot \epsilon_{PZT} \tag{3.3}$$

$$\sigma_{SUB} = E_{SUB} \cdot \epsilon_{SUB} \tag{3.4}$$

   where σ is the stress and E is the Young's modulus.

4. the equilibrium condition is respected:

$$\sigma_{PZT} \cdot A_{PZT} + \sigma_{SUB} \cdot A_{SUB} = \sigma_{TOT} \cdot A_{TOT} \tag{3.5}$$

where A is the area on what the stress is applied.

Considering that:

$$A_{PZT}/A_{TOT} = Q_{PZT} \tag{3.6}$$

and

$$A_{SUB}/A_{TOT} = Q_{SUB} = 1 - Q_{PZT} \tag{3.7}$$

the mixture law can be written as:

$$E_{TOT} = Q_{PZT} \cdot E_{PZT} + Q_{SUB} \cdot E_{SUB} \tag{3.8}$$

or:

$$E_{TOT} = Q_{PZT} \cdot E_{PZT} + (1 - Q_{PZT}) \cdot E_{SUB} \tag{3.9}$$

In this way a Young's modulus useful for the preliminary dimensioning and the finite element modelling can be calculated:

$$E_{TOT} = 0.66 \cdot 5E^{10} + (1 - 0.66) \cdot 19.310^{10} = 106MPa \tag{3.10}$$

A similar approach can be used to evaluate an homogeneous density ρ_{TOT}, given that:

$$\rho_{TOT} = \frac{W_{TOT}}{V_{TOT}} \tag{3.11}$$

where W is the weight and V is the volume. Considering:

$$W_{TOT} = \rho_{PZT} \cdot V_{PZT} + \rho_{SUB} \cdot V_{SUB} \tag{3.12}$$

It's possible to rewrite 3.11 as:

$$\rho_{TOT} = \frac{\rho_{PZT} \cdot V_{PZT} + \rho_{SUB} \cdot V_{SUB}}{V_{TOT}} \tag{3.13}$$

and considering:

$$V_{PZT}/V_{TOT} = Q_{PZT} \tag{3.14}$$

$$V_{SUB}/V_{TOT} = Q_{SUB} = 1 - Q_{PZT} \tag{3.15}$$

it's possible to write:

$$\rho_{TOT} = Q_{PZT} \cdot \rho_{PZT} + Q_{SUB} \cdot \rho_{SUB} \tag{3.16}$$

or:

$$\rho_{TOT} = Q_{PZT} \cdot \rho_{PZT} + (1 - Q_{PZT}) \cdot \rho_{SUB} \tag{3.17}$$

In this way a density useful for the preliminary dimensioning and the finite element modelling can be calculated:

$$\rho_{TOT} = 0.66 \cdot 7800 + (1 - 0.66) \cdot 8000 = 7869 Kg/m^3 \tag{3.18}$$

3.1.3 Buckling analysis

In engineering, when a structural member, subjected to high compressive stresses, experiences a state of elastic instability then it is said to be buckled and in a state of unstable equilibrium. For the case of an ideal (perfectly straight, homogeneous, and free from initial stress), long, slender column the buckling load is defined by Euler formula [5]:

$$P_{cr} = \frac{\pi^2 EI}{(KL)^2} \tag{3.19}$$

where P_{cr} is the axial load that causes the buckling, E is the Young's modulus, I is the area moment of inertia, L is the unsupported length of column and K is the column effective length factor, whose value depends on the conditions of end support of the column, as follows:

1. For one end fixed and the other end free to move laterally, K = 2.

2. For both ends fixed, K = 0.5.

3. For one end fixed and the other end pinned, K = 0.6999.

4. For both ends pinned (hinged, free to rotate), K = 1.

The different shapes of buckled columns, depending on the boundary condition and therefore from K coefficient, are shown in Figure 3.2.

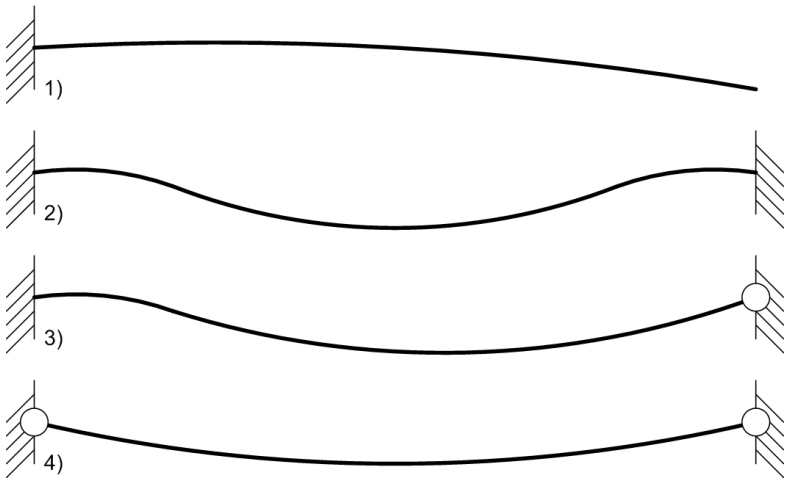

Figure 3.2: Euler buckling shapes depending on the boundary conditions:
1) K = 2
2) K = 0.5
3) K = 0.6999
4) K = 1

From the analysis of the Euler buckling shapes the boundary conditions of the beam have been chosen. The condition that allows a unique curvature of the beam (consequently a state of stress that ensures one face of the beam to be compressed and one face in tension, ensuring a uniform voltage production) is with both the ends pinned as described in Figure 3.3.

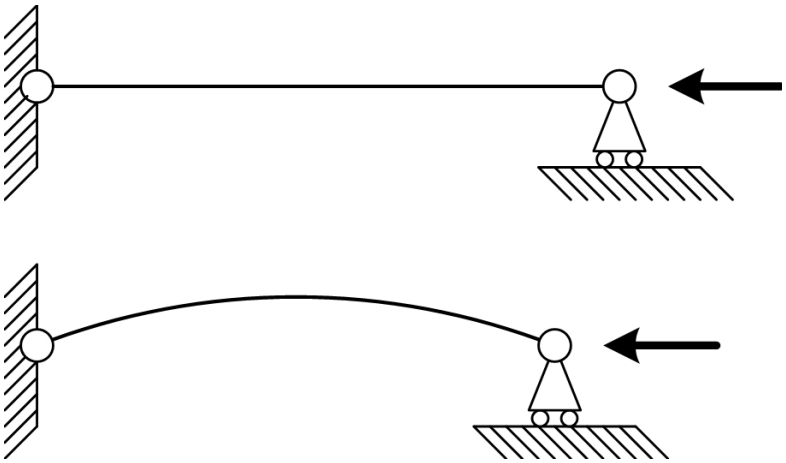

Figure 3.3: Buckling of a simply supported column

Applying the formula 3.19, using the Young's modulus calculated with 3.10 and considering the dimension described in Figure 3.1 a buckling load of 9.17 N is calculated.

3.1.4 Critical buckling stress

From Figure 3.3 it is evident that the stress distribution in the beam is complex and related not only to the compression state but also to the curvature of the beam. The definition of the stresses at this stage can only be done considering the state of compression that the beam is bearing just before buckling [5], as described in equation 3.20.

$$\sigma = \frac{P_{cr}}{A} = \frac{\pi^2 EI}{A(KL)^2} \tag{3.20}$$

Where P_{cr} is the critical buckling load defined in equation 3.19.

That can be rewritten, considering $r = \sqrt{I/A}$, as:

$$\sigma = \frac{\pi^2 E}{L/r} = \frac{\pi^2 E}{(KL/r)^2} \tag{3.21}$$

A compressive stress of 1.13 MPa has been calculated. It is important to underline that this is the compression state induced by the buckling load,

and it's not representative of the stresses after the bucking of the beam.

3.1.5 Modal analysis

The natural frequency of a simply supported beam can be calculated in rad/s as [15]:

$$\omega = (\frac{n\pi}{L})^2 \sqrt{\frac{EI}{A\rho}} \tag{3.22}$$

Where L is the length of the beam, E is the Young's modulus, I is the area moment of inertia, A is the area of the beam, ρ is the density of the beam and n is the order of the resonance frequency.

A first natural frequency of 391.6 rad/s that corresponds to 62.33 Hz has been calculated.

3.2 Finite element modelling

The finite element modelling is organized in two main stages:

1. the development of a set of purely mechanical approaching models with increasing complexity;
2. an electro mechanical model used to:
   (a) model the beam used in the test phase
   (b) investigate the shape optimisation of the beam

The development of the electro-mechanical model coincides with its validation: the theoretical results obtained for the buckling and for the resonance frequency in sections 3.1.3 and 3.1.5 will be the validation parameter. The model will be built step by step increasing the complexity of the used elements. By comparing the results of different analyses, it is possible to understand the mismatch between the results and also to validate the final

model.

The aim of the finite element modelling is to understand the behaviour of the beam and to create a realistic model of the beam that will be produced and tested. To obtain a really thorough model several details (such as the dissipation of the constraints and the dumping effect of the interface between substrate and piezoelectric materials) should be taken into account, but this is beyond the scope of this work.

The electro-mechanical model will also be used to study a lozenge-shaped beam footprint, as proposed by Baker et al. [3], that is believed to be able to increase the power output by 30%.

3.3 Experimental work

The aim of the experimental work is to prove the testing station, the testing jig and the working principles identified in the modelling stage. After the set up of the experimental apparatus, the testing will follow a flexible path depending on the obtained results. The first experiment will be finalised in the recording of the voltage output for the device, under different boundary conditions. After the first analysis of the results it will be possible to address the particular issues encountered during the first experiment stage. A second experiment will be set up aimed to delve into the working principles of the bimorph, simply supported bi-stable beam-based energy harvesting device.

Even if the goal of the finite element modelling is not to obtain a predictive model of the beam used for the device testing, it is believed that a higher closeness from the results of the two phases of the work can be obtained realizing autonomously the beam. This will provide complete knowledge on the used materials and therefore will lead to an exact correspondence between the mechanical properties of the modelled and real beam.

By organising the experimental work in this flexible way, it is possible

to experimentally test the results of the finite element modelling and identify the reasons of possible behaviour mismatches and focus the subsequent experiments on the design improvement.

Chapter 4

Finite Element Modelling

This chapter describes the Finite Element simulation stage of this research work. All the models presented in this chapter are developed with ANSYS. Section 4.1 describes the development of the finite element model, described in section 4.2, through a series of approaching models. Section 4.3 describes the simulation results obtained with the finite element model of the testing beam. Section 4.4 describes the optimisation work done on the footprint of the beam.

4.1 Approaching models

Starting from the analytical results, the final finite element model is developed in steps through a series of approaching models, with increasing complexity as shown in Figure 4.1.

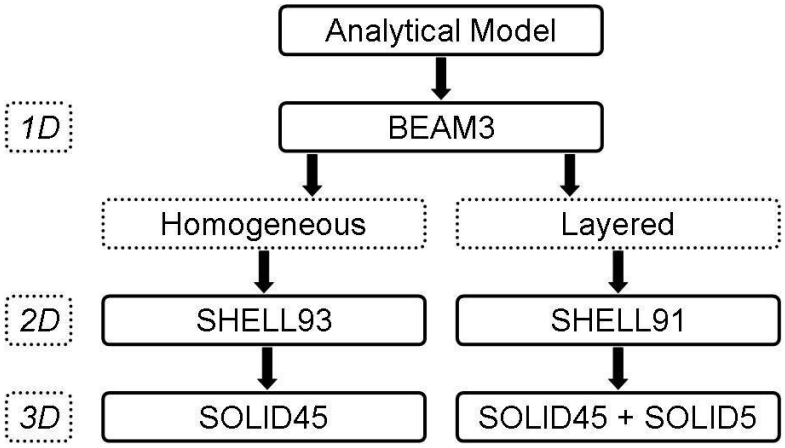

Figure 4.1: Developing of the Finite Element model

This procedure will allow the validation of the final model as last stage of an evolution based on the analytical results.

The complexity of the model is increased from the element's point of view moving from a 1D element (BEAM3) to 2D SHELL elements and finally to 3D SOLID elements.

The modelled structure is a bimorph beam: a three layer laminate, with a substrate in the middle and the piezoelectric materials as top and bottom layers. The models take in account a homogeneous and a layered distribution of the materials.

At this stage only the mechanical response of the beam is taken in account, no electro-mechanical coupling is considered. The electro-mechanical model will be detailed in section 4.2.

The codes used to build the models are listed in Appendix A.

4.1.1 Models descriptions

Some features are common to all the approaching models:

- the plan footprint of the beam is rectangular with 20 mm × 100 mm dimensions;
- all the elements of the various models have the same size, 2 mm.

BEAM3 Model

This model uses 1D elements; thickness, width, area and moment of inertia of the beam section are implicitly defined by the real constant of the BEAM3 element. The material is considered to be homogeneous and the values obtained in section 3.1.2 are used.

SHELL93 Model

This model uses 2D elements; the thickness of the beam is implicitly defined by the real constant of the SHELL93 element. The material is considered to be homogeneous and the values obtained in section 3.1.2 are used.

SHELL91 Model

This model uses 2D elements; the thickness of the beam is implicitly defined by the real constant of the SHELL91 element. The material is considered to be layered in a bimorph configuration as defined by the real constant of the SHELL91 element.

SOLID45 Model

This model uses 3D elements; the material is considered to be homogeneous and the values obtained in section 3.1.2 are used.

SOLID45 & SOLID5 Model

This model uses 3D elements; the substrate material is modelled with SOLID45 elements and the Piezoelectric material is modelled with SOLID5 elements.

4.1.2 Analyses description

The purely structural analyses are done in the following order:

1. Modal analysis to calculate the resonance frequencies and their shapes;
2. Buckling analysis to obtain the buckling load;
3. Static analysis to calculate the response of the structure under the buckling load;
4. Pre-stressed modal analysis to calculate the resonance frequencies of the beam under axial load;
5. Harmonic analysis to calculate the response of the beam under vibrations.

Modal analysis

In the case of the modal analysis the boundary conditions are the following:

- both the extremes of the beam are pinned, the displacement but not the rotation along the three axes is blocked;
- no forces are loading the structure.

The solution method chosen is the Block Lanczos method extracting 5 modes.

Buckling analysis

In the case of the buckling analysis the boundary conditions are the following:

- one extreme of the beam is pinned, the displacement but not the rotation along the three axes is blocked;

- one extreme of the beam has the displacement along Y and Z fixed, the beam tip is free to move along X, all the rotations are free;
- the extreme of the beam free to move along the X direction is loaded with a unitary force along the X direction that compresses the beam.

The buckling analysis is performed using the Block Lanczos solution method, extracting 5 modes.

Static analysis

In the case of the static analysis the boundary conditions are the following:

- one extreme of the beam is pinned, the displacement but not the rotation along the three axes is blocked;
- one extreme of the beam has the displacement along Y and Z fixed, the beam tip is free to move along X, all the rotations are free;
- the extreme of the beam that is free to move along the X direction is loaded with a force equal to the buckling load along the X direction that compresses the beam.
- the centre of the beam is loaded with a force equal to one hundredth of the buckling load along the Z direction to create an interference that causes the beam to buckle at the minimum buckling load.

The static analysis is performed with the option for the large deflections activated.

The outputs of interest are:

1. the displacement along the X axis of the beam tip;
2. the displacement along the Z axis of the beam centre;
3. the Von Mises stress;
4. the stresses along the X, Y, Z axis directions;
5. the XY shear stress.

Pre-stressed modal analysis

In the case of the pre-stressed modal analysis the boundary conditions are the following:

- one extreme of the beam is pinned, the displacement but not the rotation along the three axes is blocked;
- one extreme of the beam has the displacement along Y and Z fixed, the beam tip is free to move along X, all the rotations are free;
- the extreme of the beam that is free to move along the X direction is loaded with a force equal to one quarter, one half, three quarter and the full buckling load along the X direction that compresses the beam.

This analysis is performed in two steps:

1. a static analysis is performed with the option for the large deflections and for the pre-stress calculation activated;
2. the modal analysis is performed with the Block Lanczos solution method, the pre-stress option is activated and the coordinates are updated to the displacements calculated at the previous step.

Harmonic analysis

In the case of the harmonic analysis the boundary conditions are the following:

- both the extremes of the beam have all the rotations free and are allowed a displacement along Z of 4 μm;
- no forces are loading the structure.
- the damping ratio is calculated as $DR = 1/2Q$ where Q is the quality factor and has a value of 32.

Pre-stressed harmonic analysis

The code of a pre-stressed harmonic analysis was prepared along the lines of the pre-stressed modal analysis, but it could not be successfully run. The main problem in developing this code is the update of the coordinates between the static and the harmonic analysis. The boundary conditions of the harmonic analysis are different from the one in the non linear static analysis. and it was not possible to find a way to overcome this problem. An attempt was done trying to perform a simple harmonic analysis with an axial compressive load acting on the beam: this solution did not work because also the axial compressive load was treated as an harmonic load by the solver.

4.1.3 Results

Buckling analysis

The results for the bucking analysis are shown in Figure 4.2 and reported in Table 4.1.

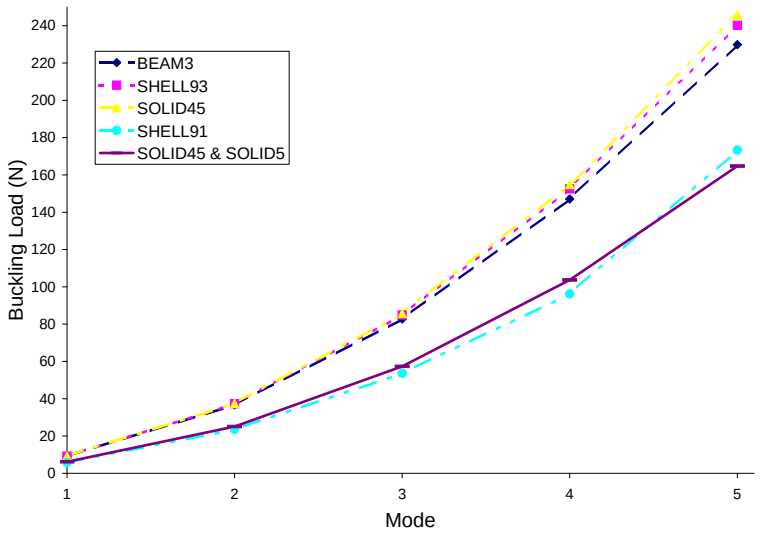

Figure 4.2: Results for the buckling analysis

Table 4.1: Results for the buckling analysis

Model	1^{st} Mode (N)	2^{nd} Mode (N)	3^{rd} Mode (N)	4^{th} Mode (N)	5^{th} Mode (N)
Analytical	9.17				
BEAM3	9.19	36.78	82.75	147.12	229.88
SHELL93	9.23	37.30	84.90	152.48	240.19
SOLID45	9.25	37.49	85.74	154.90	245.78
SHELL91	5.82	23.53	53.56	96.21	173.32
SOLID45 & SOLID5	6.18	25.06	57.35	103.70	164.75

The results are close to each other with a difference of less than 1% between the three homogeneous models. The layered models show a drop of the buckling load of approximately 35% and a difference between each other of about the 6%. The difference can be explained considering a different distribution of the materials and consequentely of the stiffnesses along the thickness of the beam: the softer material is external and this contributes to an earlier instabilty state of the beam.

Modal analysis

The results for the modal analysis are shown in Figure 4.3 and reported in Table 4.2.

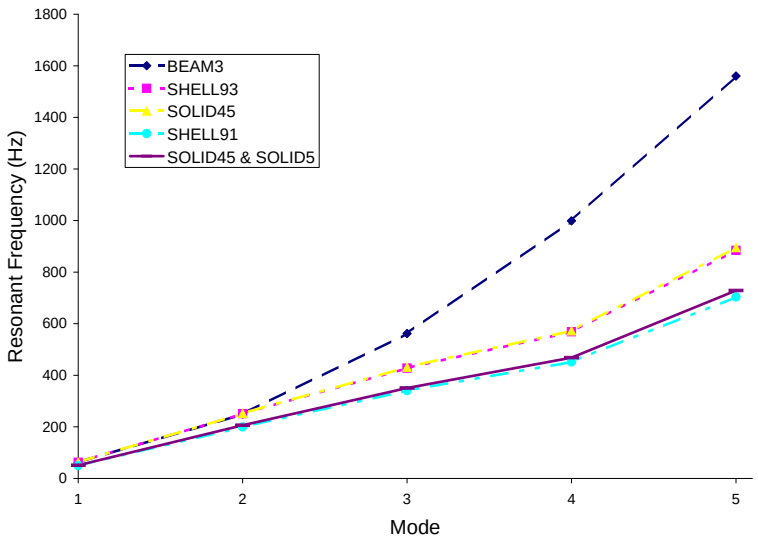

Figure 4.3: Results for the modal analysis

The results are in good accordance with each other and with the analytical calculation. As expected the layered models showed a difference with the homogeneous models, this can be explained considering the different distribution of the stiff areas in the beam.

The results of the simulations are close to each other, the three homoge-

Table 4.2: Results for the modal analysis

Model	1^{st} Mode (Hz)	2^{nd} Mode (Hz)	3^{rd} Mode (Hz)	4^{th} Mode (Hz)	5^{th} Mode (Hz)
Analytical	62.3				
BEAM3	62.4	249.7	561.7	998.6	1560.2
SHELL93	62.6	251.4	428.1	568.9	884.6
SOLID45	62.6	252.2	431.7	572.6	895.1
SHELL91	49.7	199.7	340.6	451.9	703.7
SOLID45 & SOLID5	51.2	206.2	350.6	468.3	728.7

neous models have almost the same first resonance frequency. The BEAM3 model gives results for the higher resonance frequencies that move away from those obtained for the other two homogeneous models. This is because of the difference in the mode shapes.

The layered models show a drop in the first resonance mode of approximately 25% as compared to the homogeneous models and a difference between each other of about 4%. The difference can again be explained by considering the different distribution of the sitffnesses along the thickness of the beam.

The shapes related to each mode are shown in Figure 4.4 for the BEAM3 and the SHELL91 models, the mode shapes for SHELL91 are representative for all the other models.

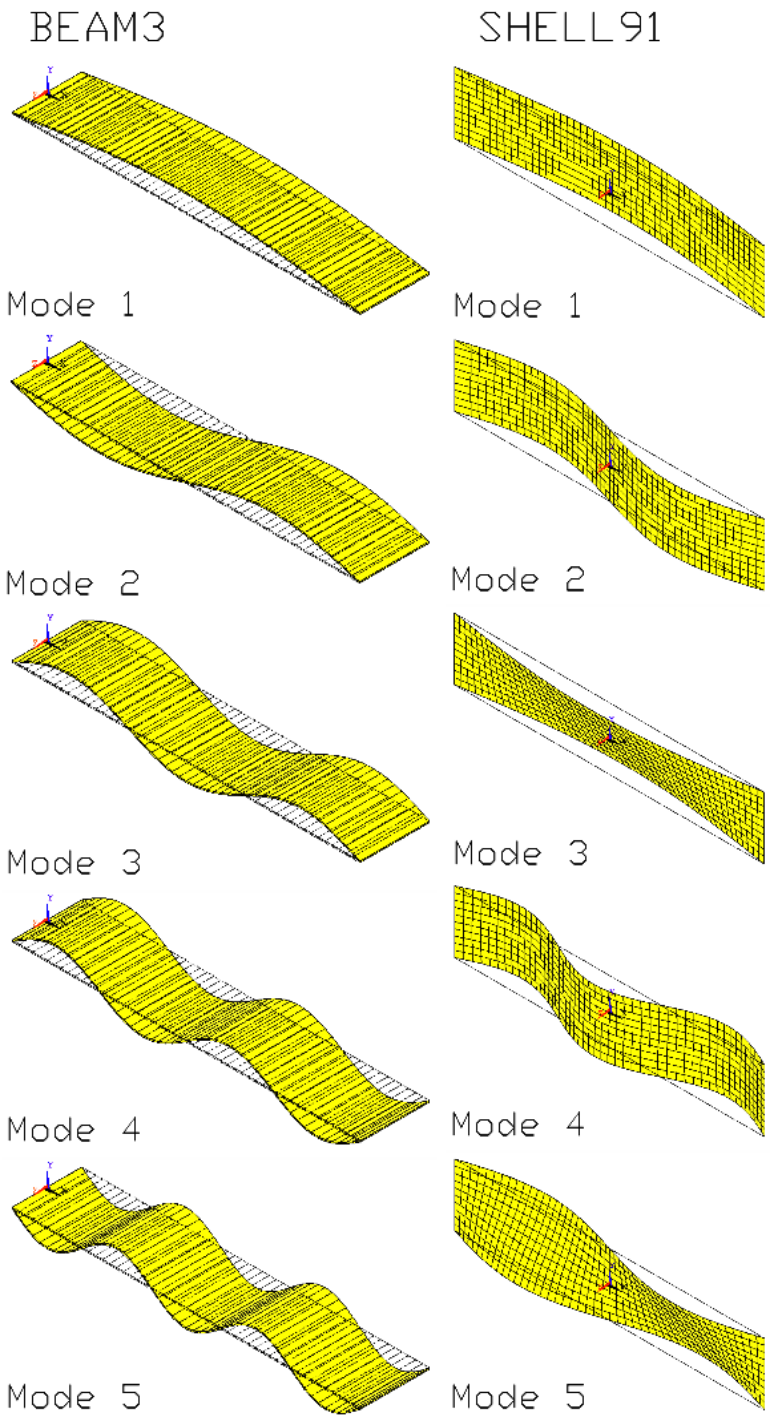

Figure 4.4: Mode shapes for BEAM3 and SHELL91 models

The BEAM3 mode shapes are in accordance with the theoretical flexural

shapes described by the formula $y_x = sin(\frac{\pi n x}{L})$ (where n is a positive integer and L is the length of the beam). This behaviour is obtained because BEAM3 is a mono-dimensional element. In models built with bi or tri-dimensional elements, both flexural shapes and torsional modes can be observed.

Static Analysis

Table 4.3 reports the results of the large displacement static analysis, this table is not completely filled in because some of the data needed cannot be calculated for some specific elements.

The results for the X displacement of the beam end which is free to move along this direction and for the Z displacement of the centre of the beam are shown in Figure 4.5.

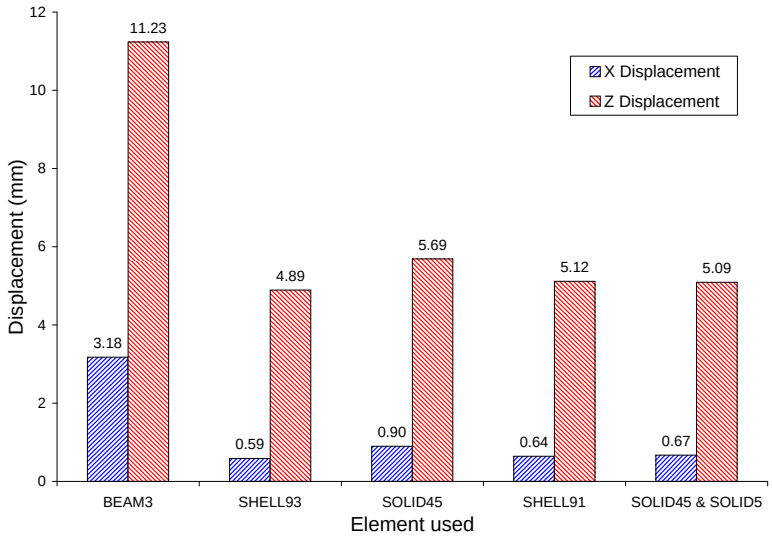

Figure 4.5: X and Z displacements.

In this case the results show a mismatch between them, this is due to a higher complexity of the analysis and by the substantial differences of the models: different densities and distributions of nodes in the various models result in a different outcome. It is believed that the 1D model results are

Table 4.3: Results of the large displacement static analysis

Model	U_X (mm)	U_Y (mm)	$\sigma_{VonMises}$ (MPa)	σ_X (MPa)		σ_Y (MPa)		σ_Z (MPa)		τ_{XY} (MPa)
BEAM3	3.18	11.23								
SHELL93	0.57	4.89	111	-109	111	-15.4	14.8			5.8
SOLID45	0.9	5.69	130	-128	131	-20.8	20.1	-1	1.2	6.81
SHELL91	0.64	5.12	66.9	-66.6	66.8	-12.6	12.8			3.24
SOLID45 & SOLID5	0.67	5.09	85.3	-70.3	86	-12.5	12.2	-0.76	0.88	4.03

unreliable, BEAM3 is too rough an element for a non linear static analysis, and that the results most closely simulating the reality are the ones from the SOLID45 & SOLID5 model, that exploit more refined elements.

Pre-stressed modal analysis

The results for the pre-stressed modal analysis are presented in Tables 4.4, 4.5, 4.6 4.7 and 4.8 and are shown in Figures 4.6, 4.7, 4.8, 4.9 and 4.10.

Table 4.4: Results of the pre-stressed modal analysis for BEAM3 model

Pre-load	1^{st} Mode (Hz)	2^{nd} Mode (Hz)	3^{rd} Mode (Hz)	4^{th} Mode (Hz)	5^{th} Mode (Hz)
1/4 BL	54.0	255.1	554.2	992.4	1558.6
1/2 BL	44.2	241.8	546.2	984.6	1550.8
3/4 BL	31.4	233.6	538.2	976.7	1542.9
BL	9.1	216.1	529.9	969.6	1535.0

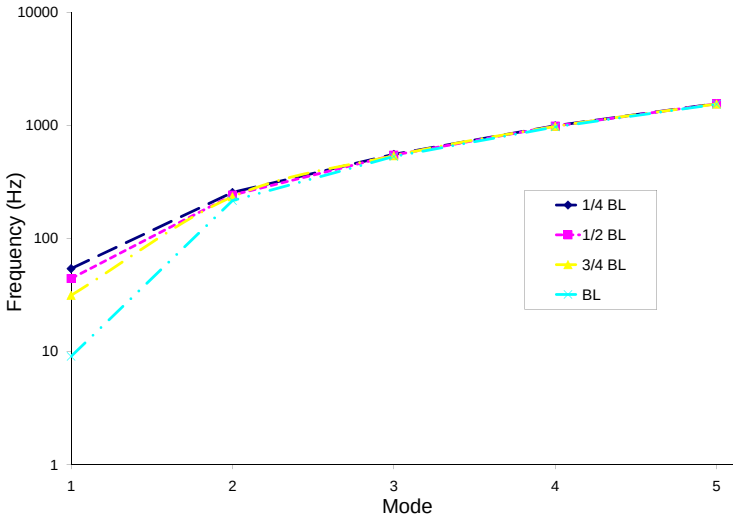

Figure 4.6: Results of the pre-stressed modal analysis for BEAM3 model

Table 4.5: Results of the pre-stressed modal analysis for SHELL93 model

Pre-load	1^{st} Mode (Hz)	2^{nd} Mode (Hz)	3^{rd} Mode (Hz)	4^{th} Mode (Hz)	5^{th} Mode (Hz)
1/4 BL	54.2	243.6	426.9	561.2	882.4
1/2 BL	44.3	235.4	425.8	553.3	880.2
3/4 BL	31.4	227.0	424.7	545.3	878.0
BL	9.2	217.8	423.5	536.9	875.7

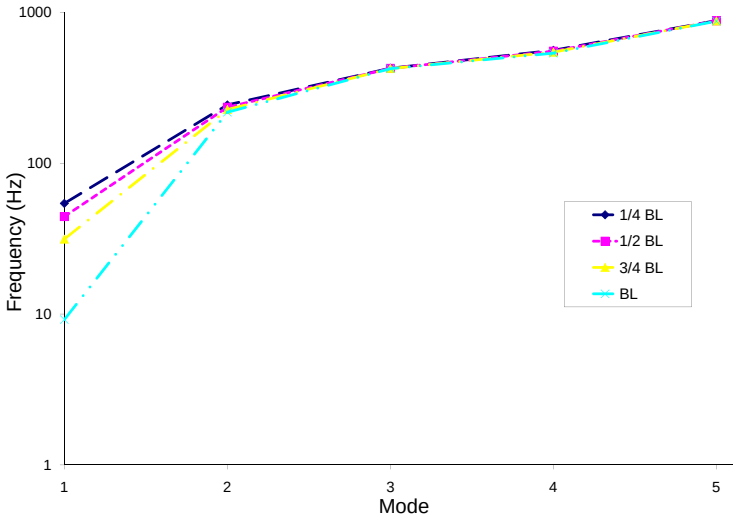

Figure 4.7: Results of the pre-stressed modal analysis for SHELL93 model

Table 4.6: Results of the pre-stressed modal analysis for SOLID45 model

Pre-load	1^{st} Mode (Hz)	2^{nd} Mode (Hz)	3^{rd} Mode (Hz)	4^{th} Mode (Hz)	5^{th} Mode (Hz)
1/4 BL	54.2	244.3	430.5	564.8	892.9
1/2 BL	44.2	236.1	429.4	556.9	890.7
3/4 BL	31.1	227.6	428.2	548.6	888.4
BL	9.1	219.1	427.1	541.0	886.3

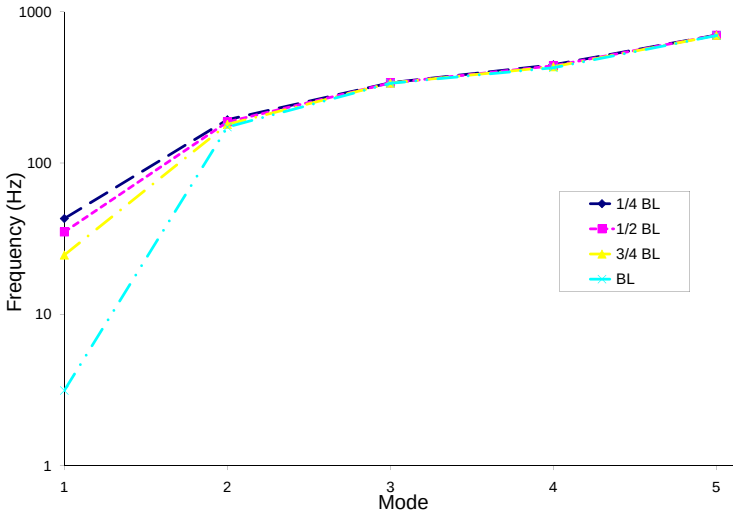

Figure 4.8: Results of the pre-stressed modal analysis for SOLID45 model

Table 4.7: Results of the pre-stressed modal analysis for SHELL91 model

Pre-load	1^{st} Mode (Hz)	2^{nd} Mode (Hz)	3^{rd} Mode (Hz)	4^{th} Mode (Hz)	5^{th} Mode (Hz)
1/4 BL	43.0	193.4	339.7	446.7	701.9
1/2 BL	35.0	186.9	338.7	439.4	700.2
3/4 BL	24.7	180.1	337.8	433.0	698.4
BL	3.1	173.1	336.9	426.5	696.6

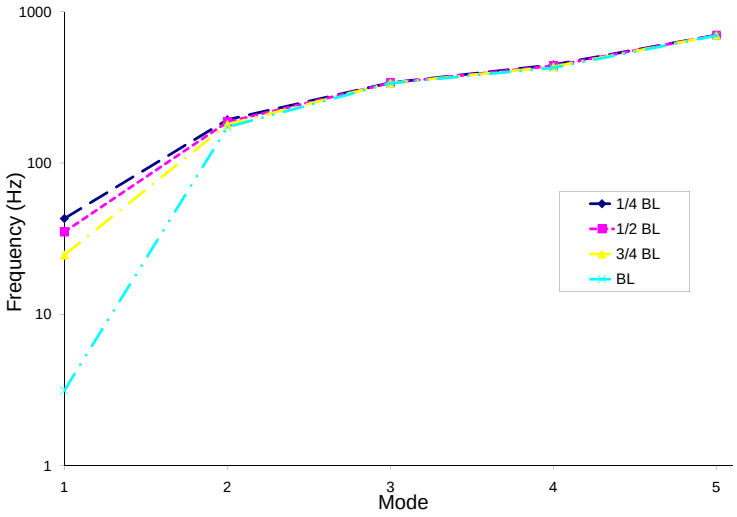

Figure 4.9: Results of the pre-stressed modal analysis for SHELL91 model

Table 4.8: Results of the pre-stressed modal analysis for SOLID45 & SOLID5 model

Pre-load	1^{st} Mode (Hz)	2^{nd} Mode (Hz)	3^{rd} Mode (Hz)	4^{th} Mode (Hz)	5^{th} Mode (Hz)
1/4 BL	44.2	199.2	348.9	459.5	721.3
1/2 BL	36.1	192.5	348.0	460.0	719.5
3/4 BL	25.4	185.5	347.1	446.4	717.6
BL	2.8	178.5	346.1	439.9	715.8

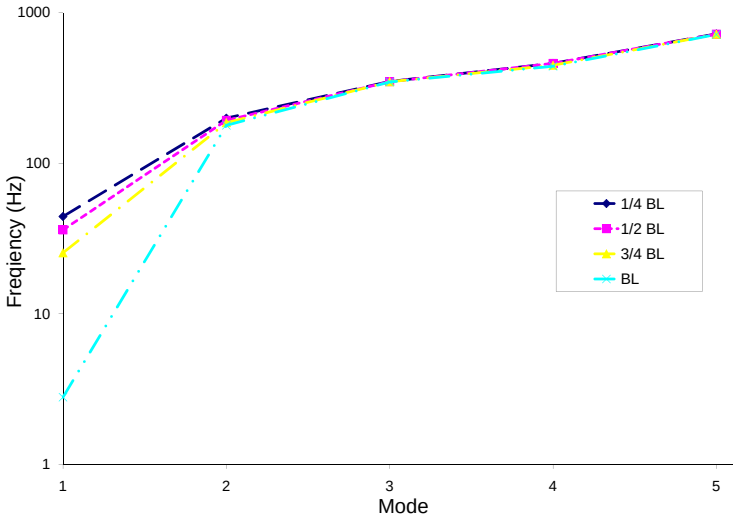

Figure 4.10: Results of the pre-stressed modal analysis for SOLID45 & SOLID5 model

From the analysis of the results it is possible to conclude that the application of an axial pre-load to all the simply supported beams modelled here shifts down the resonance frequencies. This phenomenon can be observed more clearly by plotting the first resonance frequency, of an axially pre-loaded beam, calculated for different fractions of the buckling load. (Figure 4.11).

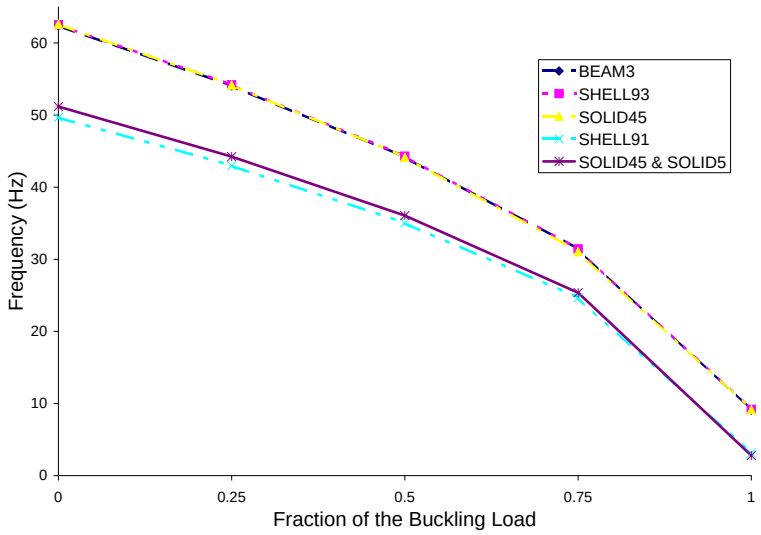

Figure 4.11: First resonance frequency at different pre-stress

Even if the difference in absolute values appears clear between the homogeneous and layered models, the trend with which the resonance frequency decreases is consistent between all the models.

Harmonic analysis

The results for the harmonic analysis are shown in Figure 4.3.

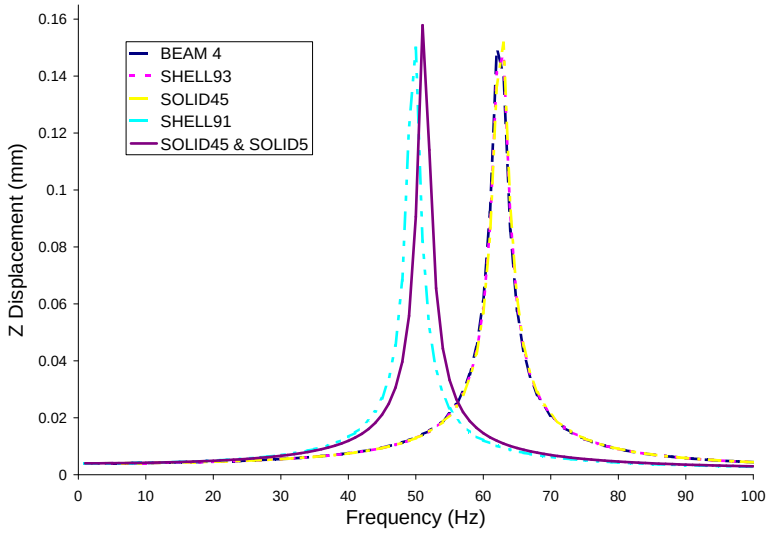

Figure 4.12: Results for the harmonic analysis

The Harmonic analysis confirms the results obtained in the modal analysis. The response for the homogeneous models were condensed around 62 Hz and for the layered models around 50 Hz. Considering the same damping ratio for all the models the displacement of the beam centre is almost the same.

4.2 Final model description

From the approaching models, a final model was developed to simulate the purely mechanical and the electro-mechanical behaviour of the beam. Two different models are used in the research work:

1. A testing beam model to simulate the beam that will be used for the experiments.

2. A beam footprint optimisation model to find if there is a possibility to increase the voltage output acting on the beam footprint.

Useful indications about the modelling of piezoelectric bimorph beams was found in the work of Zhu et al., who studies the electromechanical behaviour of a cantilever beam based energy harvesting device. The meshing and

the electrical connection systems described here are derived from the models used in [28] and [29].

4.2.1 Used elements

The model uses four different kinds of elements:

1. PLANE42: a purely mechanical 2D element used as ancillary element to map the meshing of the structure. This element is not selected during the solution step;

2. SOLID45: a purely mechanical 3D element, used to model the substrate material and the stiffeners;

3. SOLID5: a 3D multi-physic element, used to model the piezoelectric material. In the purely mechanical analyses this element is used with the KEYOPT(1)=2, that allows only the displacements in X, Y and Z as degrees of freedom to save computing time and space. In the electro-mechanical analyses the element is used with the KEYOPT(1)=3, that adds the voltage to the degrees of freedom of the element;

4. MASS21: a point element used to model the mass added to the beam.

4.2.2 Material data

The material data are defined in ANSYS as suggested by Imaoka in [7] who details the method to process the data provided by the manufacturers and feed them to ANSYS. The substrate and the stiffener materials are defined as anisotropic with density, Young's modulus and Poisson's ratio, using the command MP:

```
MP, EX, 2, young modulus
MP, DENS, 2, density
MP, NUXY, 2, poisson ratio
```

The description of the piezoelectric material in ANSYS requires, besides the definition of the mechanical properties, a piezoelectric matrix to correlate

the mechanical and the electrical behaviour of the material and a dielectric matrix.

The mechanical characteristics are defined as a 6×6 compliance matrix using the TB,ANEL command:

```
TB, ANEL,1,1,,1
TBDATA, 1 , s11,s12,s13
TBDATA, 7 , s11,s13
TBDATA, 12, s33
TBDATA, 16, s66
TBDATA, 19, s44
TBDATA, 21, s44
```

The dielectric properties of the piezoelectric are described by the 3×3 diagonal electrical permittivity, defined in ANSYS as an orthotropic material property matrix:

```
eps0=8.854e-12
EMUNIT,EPZRO,eps0
MP, PERX, 1, eps11
MP, PERY, 1, eps11
MP, PERZ, 1, eps33
```

The mechanical-electrical correlation is defined in the manufacturers's data sheets by the piezoelectric matrix $[d]$, that relates the mechanical strain to the electric field. In ANSYS, the user is required to input the piezoelectric matrix $[e]$, that relates the mechanical strain to the electric field. The relation between $[d]$ and $[e]$ is defined as: $[e] = [d]^t[s^E]^{-1}$. The data are entered with the TB,PIEZ command:

```
TB, PIEZ, 1
TBDATA, 3 , e31
TBDATA, 6 , e31
TBDATA, 9 , e33
TBDATA, 14, e15
TBDATA, 16, e15
```

4.2.3 Meshing

The slender geometry of the beam and its 3-layered structure leads to difficulties in creating elements that respect the shape warning limits: the thickness is sensibly smaller than the other dimensions. The number of elements is also limited to 32000 by the license contract terms.

To partially overcome these problems, a mapped division of the mesh is adopted: element PLANE42 is used to mesh the surface and the 3D geometry is created extruding SOLID45 and SOLID5 elements. PLANE42 allows choice of two different shapes of the elements: quadrangular and triangular. Even if the triangular shapes appear the most appropriate to map non rectangular surfaces it is not suitable in this case as it invalidates the results by increasing the stiffness of the modelled beam. The element size was chosen to be equal to the one already used to mesh the approaching models: 2 mm. This size allows creation of elements where the thickness can be comparable with the other dimensions avoiding warnings on the element shapes or making this warnings non relevant. Only a few elements of the beam are reported to have a shapes that violates the warning limits, this is due to the fact that the mesh is automatically created by the program. These elements are believed not to alter the results of the simulation.

4.2.4 Voltage output calculation

For the electro-mechanical analyses the electrical connections are organized to model a bimorph beam with parallel connections as described in Figure 6.1. The surfaces of the piezoelectric that face the substrate are coupled and connected together in a node ($Node_{GR}$ in Figure 4.13). A similar approach is followed for the external surface ($Node_{SI}$ in Figure 4.13. The output of the electro-mechanical simulations will be the electrical potential difference between the two nodes.

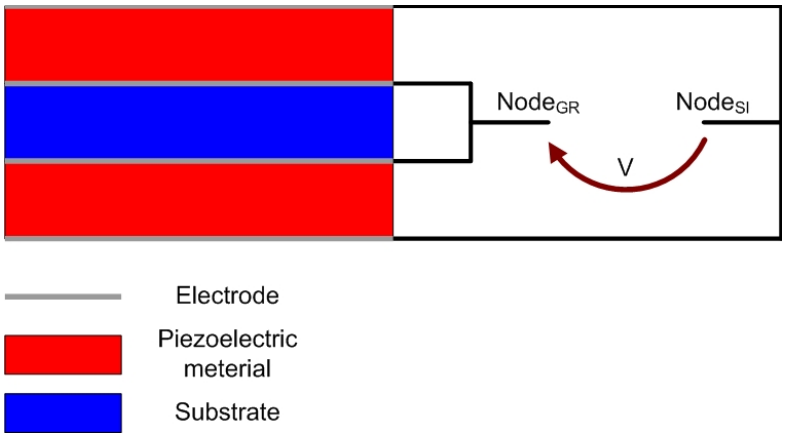

Figure 4.13: Sketch of the electrical connection of the beam

4.2.5 Analyses description

The analyses are performed identically to those described in section 4.1.2. The only difference is that in this case the harmonic analysis is performed with an electromechanical model. This model, besides the mechanical output, also predicts the voltage generated by the bimorph, simply supported bi-stable beam based energy harvesting device.

4.3 Testing beam model

The beam used for the testing is different from the one modelled so far. Figure 4.14 shows the beam that has been modelled and Figure 4.15 shows the finite element model of the beam itself.

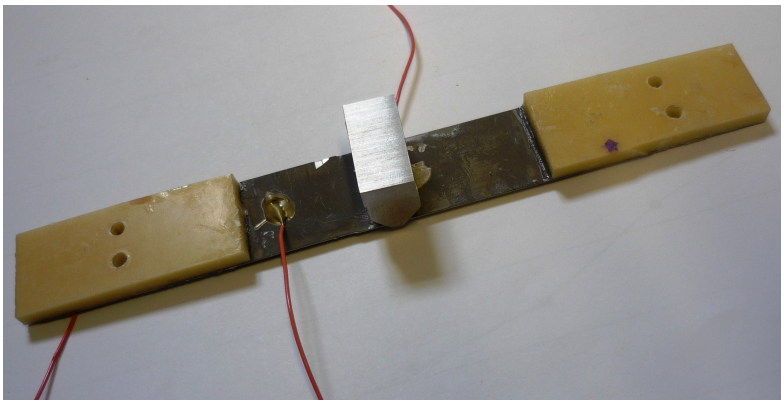

Figure 4.14: Testing Beam

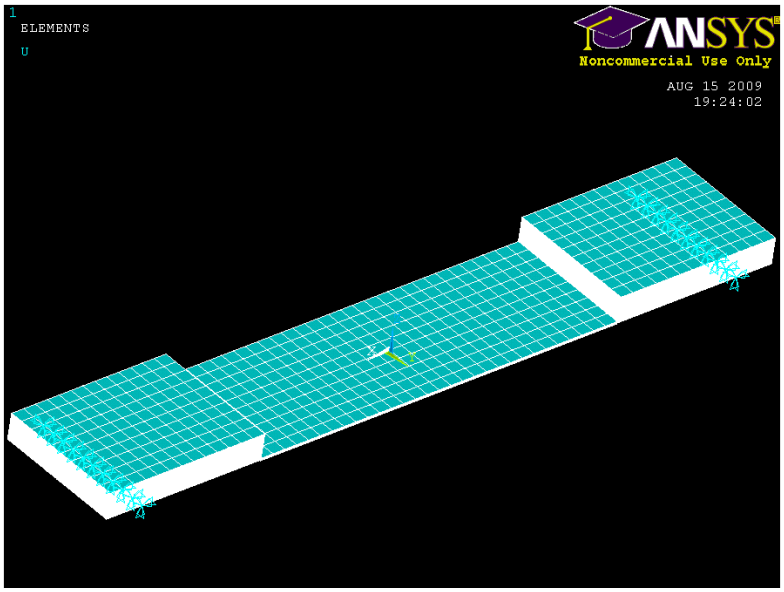

Figure 4.15: Finite element model of the testing beam

The aims of these analyses is to understand the behaviour of the beam that will be used in the experimental stage and have a rough forecast of its properties such as buckling load and resonance frequencies. It has to be taken in account that this model is not a full model of the beam: there are no contact elements to model the glue layer between the piezoelectric material and the substrate, therefore the damping effect of the glue layer could not be taken in to account. Also, the modelled hinges have an ideal behaviour, and do not dissipate any energy.

4.3.1 Analysis results

The analyses were performed as described in section 4.2.5.

Buckling analysis

The results for the bucking analysis are shown in Figure 4.16 and reported in Table 4.9.

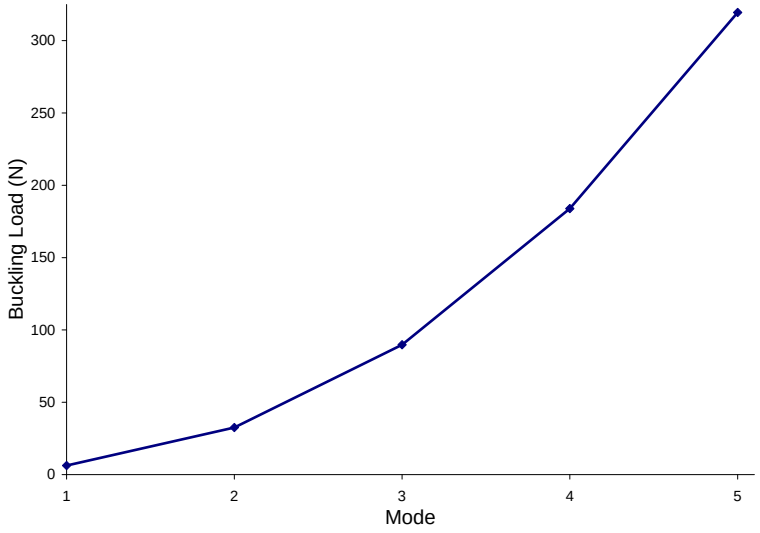

Figure 4.16: Results for the buckling analysis

Table 4.9: Results for the buckling analysis

1^{st}Mode (N)	2^{nd}Mode (N)	3^{rd}Mode (N)	4^{th}Mode (N)	5^{th}Mode (N)
6.27	32.57	89.754	188.89	319.46

Modal analysis

The results for the modal analysis are shown in Figure 4.17 and reported in Table 4.10.

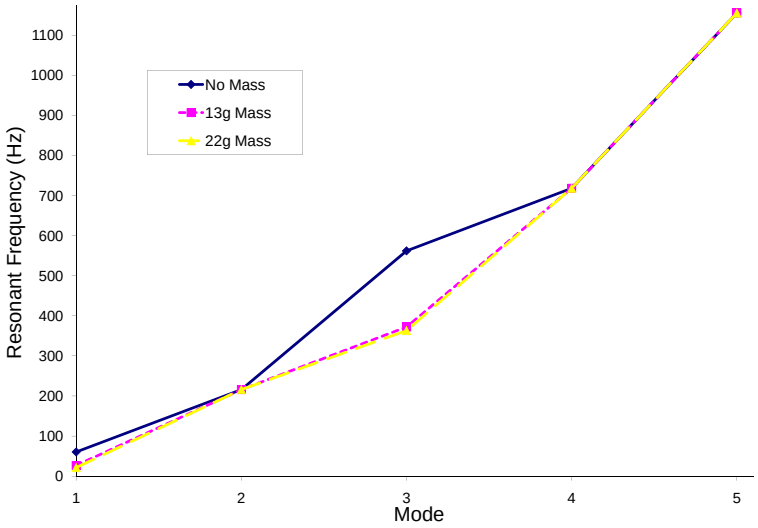

Figure 4.17: Results for the modal analysis

Table 4.10: Results for the modal analysis

Added Mass (g)	1^{st}Mode (Hz)	2^{nd}Mode (Hz)	3^{rd}Mode (Hz)	4^{th}Mode (Hz)	5^{th}Mode (Hz)
0	60.15	216.05	561.94	718.22	1155.27
13	26.57	216.05	372.18	718.22	1155.27
22	21.28	216.05	363.22	718.22	1155.27

The shapes related to each mode are shown in Figure 4.18.

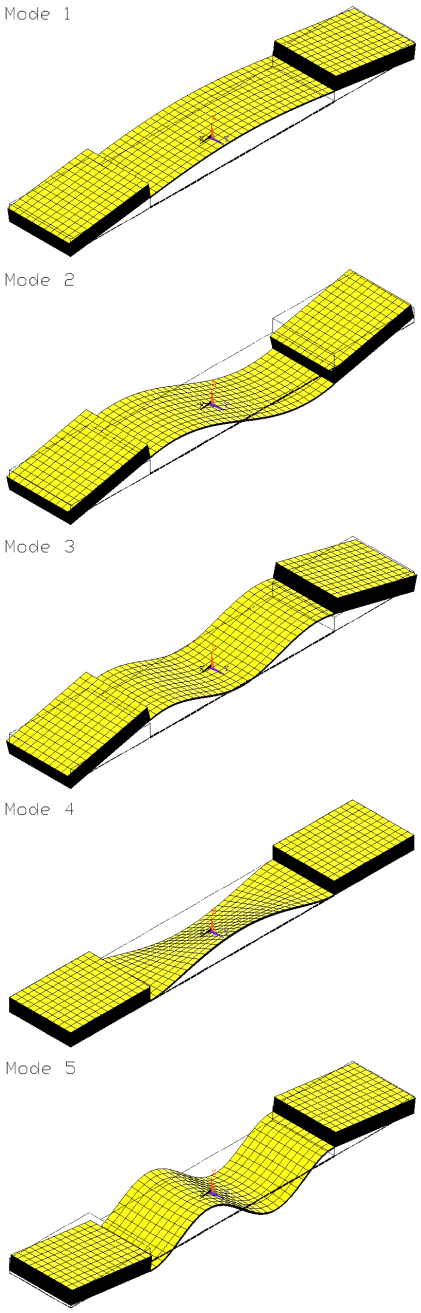

Figure 4.18: Mode shapes for the testing beam model

Static analysis

Table 4.11 reports the results of the large displacement static analysis.

Table 4.11: Results of the large displacement static analysis

U_X (mm)	U_Y (mm)	$\sigma_{VonMises}$ (MPa)	σ_X (MPa)		σ_Y (MPa)		σ_Z (MPa)		τ_{XY} (MPa)
0.67	4.476	81.4	-67.1	82.1	-27.2	13.1	-19.1	9.66	7.14

From these results it is evident that the beam will not be subjected to a stress failure even at the buckled shape.

Figures 4.32 and 4.20 show the displacements and the von Mises stress distribution of the testing beam subjected to the buckling load.

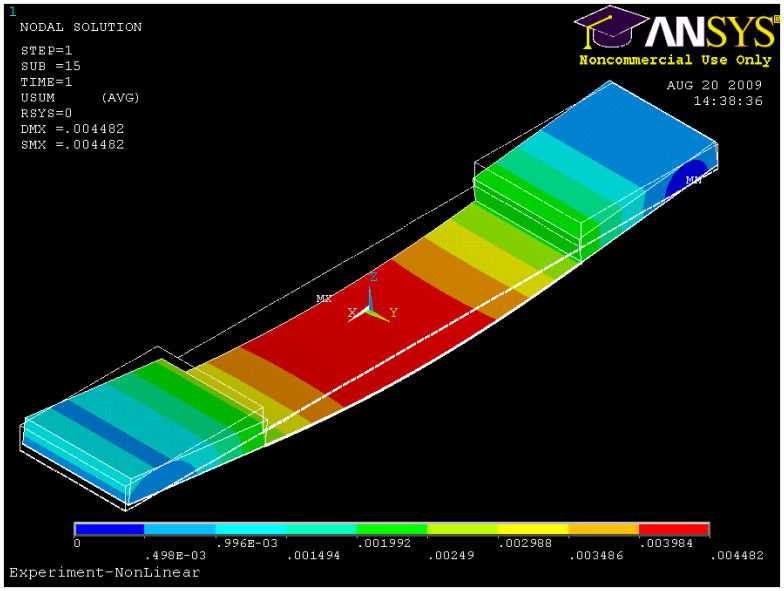

Figure 4.19: Static displacement

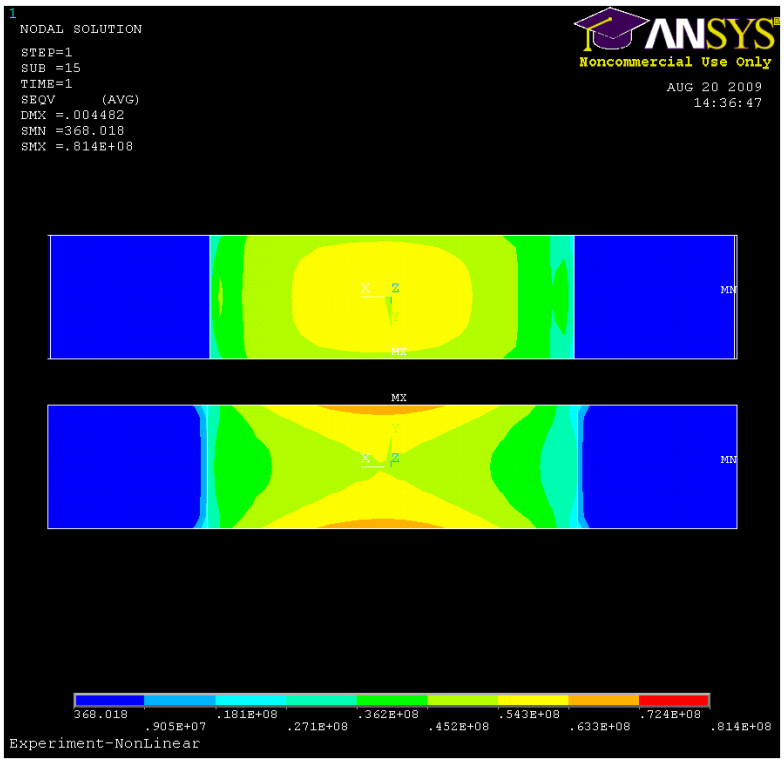

Figure 4.20: Von Mises stress distribution

Pre-stressed modal analysis

The results for the pre-stressed modal analysis are presented in Tables 4.12, 4.13 and 4.14 and shown in Figures 4.21, 4.22 and 4.23.

Table 4.12: Results of the pre-stressed modal analysis without extra mass

Pre-load	1^{st} Mode (Hz)	2^{nd} Mode (Hz)	3^{rd} Mode (Hz)
1/4 BL	39.1	193.2	522.5
1/2 BL	31.5	188.2	517.8
3/4 BL	21.3	183	513.2
BL	12.2	181.3	511.5

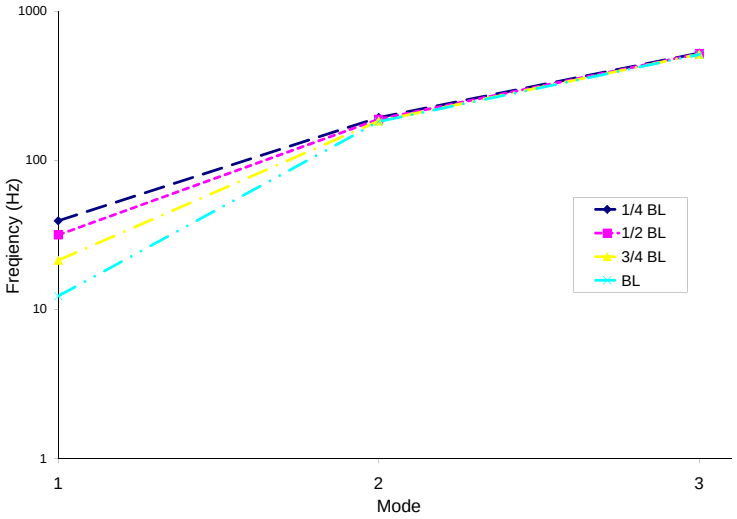

Figure 4.21: Results of the pre-stressed modal analysis without extra mass

Table 4.13: Results of the pre-stressed modal analysis with 13 g extra mass

Pre-load	1^{st} Mode (Hz)	2^{nd} Mode (Hz)	3^{rd} Mode (Hz)
1/4 BL	17.9	193.2	338.3
1/2 BL	14.4	188.1	335.1
3/4 BL	9.7	183	331.9
BL	5.7	178.9	328.4

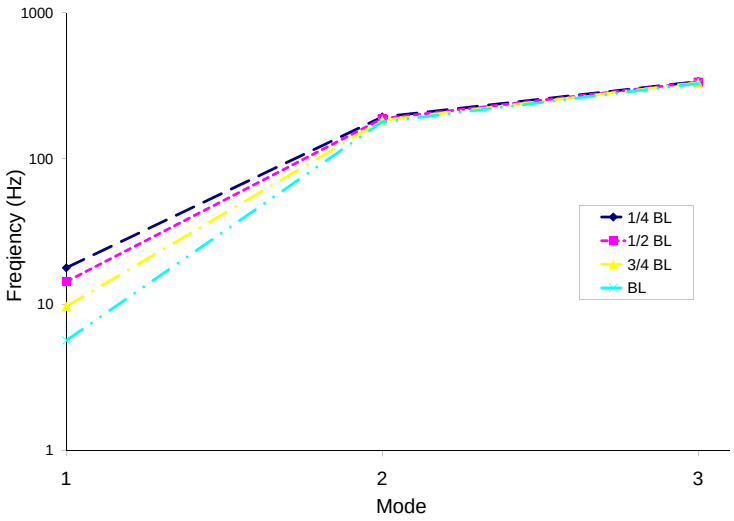

Figure 4.22: Results of the pre-stressed modal analysis with 13 g extra mass

Table 4.14: Results of the pre-stressed modal analysis with 22 g extra mass

Pre-load	1^{st} Mode (Hz)	2^{nd} Mode (Hz)	3^{rd} Mode (Hz)
1/4 BL	14.4	193.2	329.2
1/2 BL	11.5	188.2	326.1
3/4 BL	7.1	183.0	322.9
BL	4.5	178.5	317.6

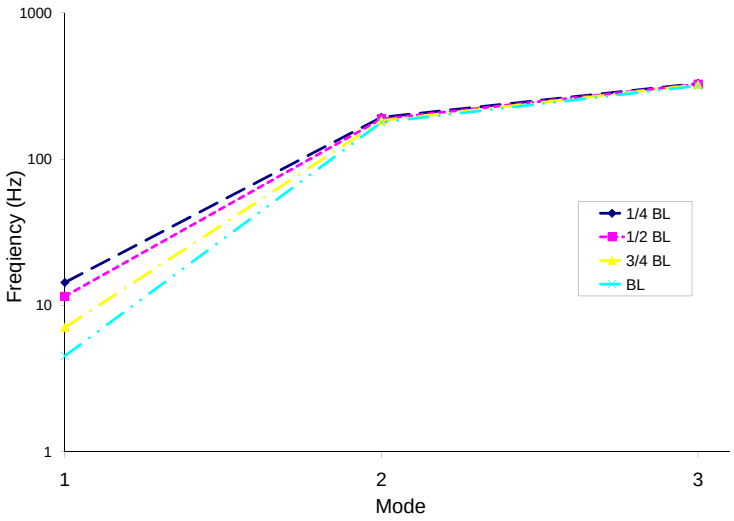

Figure 4.23: Results of the pre-stressed modal analysis with 22 g extra mass

From the analysis of the results it is possible to conclude that the application of an axial pre-load to all the simply supported beams modelled here shifts down the resonance frequencies. This phenomenon can be observed more clearly by plotting the first resonance frequency, of an axially pre-loaded beam, calculated for different fractions of the buckling load.(Figure 4.24).

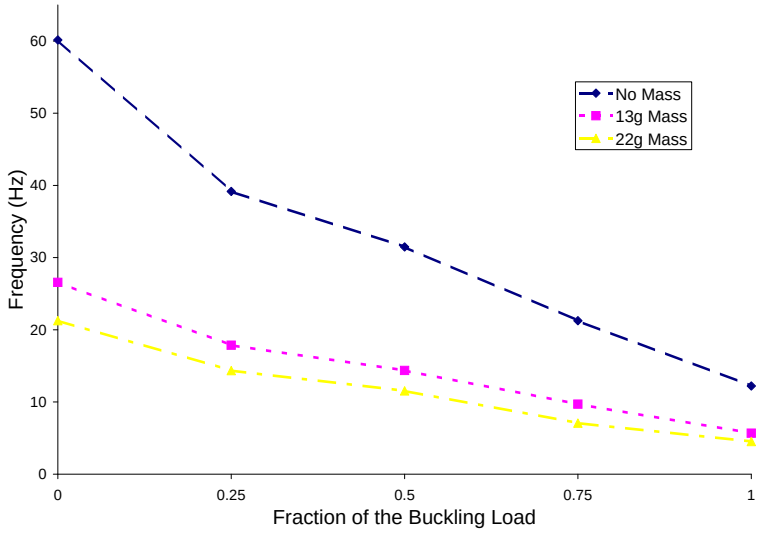

Figure 4.24: First resonance frequency at different pre-stress

Harmonic analysis

The results for the harmonic analysis are shown in Figures 4.25 and 4.26.

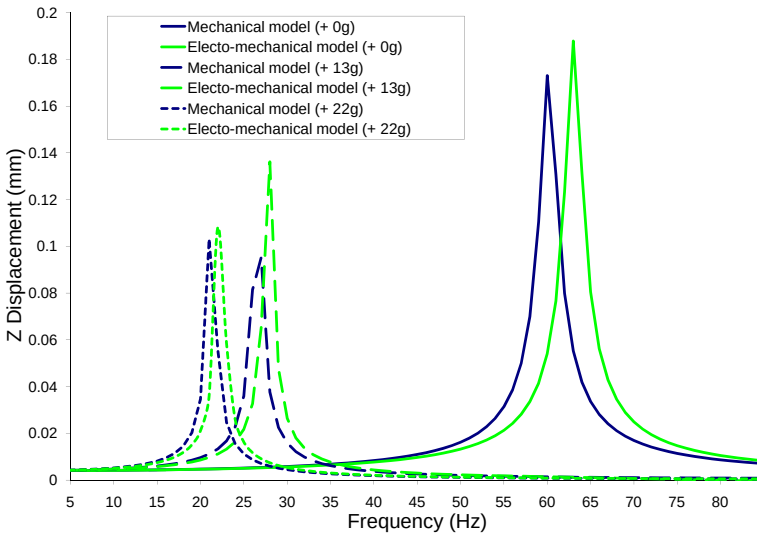

Figure 4.25: Results for the harmonic analysis

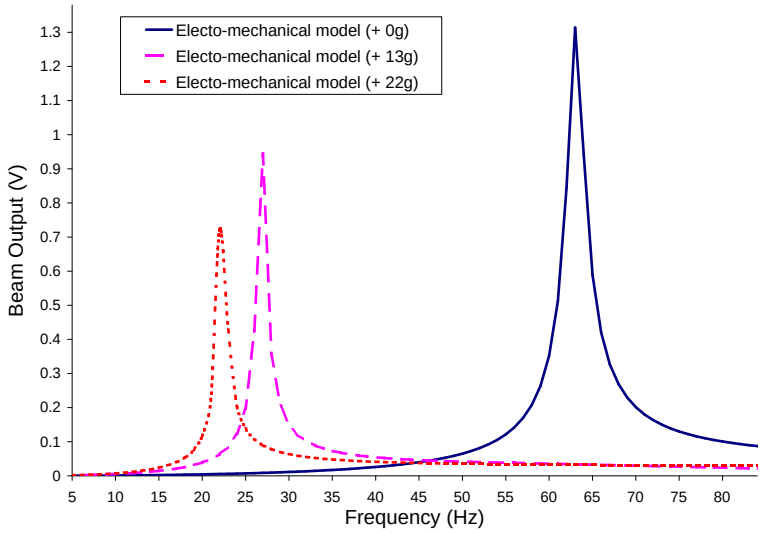

Figure 4.26: Results for the harmonic analysis

The Harmonic analysis confirms the results obtained in the modal analysis with the response at around 60 Hz for the beam with no added mass, at 26 Hz for the beam with 13 g of added mass and at 21 for the beam with 22 g of added mass. It is possible to observe that the purely mechanical model presents the resonance peak at a slightly lower frequency and with a smaller peak value than the electro-mechanical model as shown in Table 4.15.

Table 4.15: Results of the harmonic analysis

Added Mass (g)	Mechanical ω_{res} (Hz)	Mechanical Displ. (μm)	Electro-Mechanical ω_{res} (Hz)	Electro-Mechanical Displ. (μm)
+ 0	60	173	63	188
+ 13	27	95	28	136
+ 22	21	103	22	108

An evident trend appears: adding mass to the beam reduces both the resonance frequency and the displacement of the centre of the beam. The same effect is observed for the voltage output as shown in Figure 4.26 and summarized in Table 4.16.

Table 4.16: Results of the harmonic analysis

Added Mass (g)	Resonance Frequency (Hz)	Voltage output (V)
+ 0	63	1.31
+ 13	28	0.94
+ 22	22	0.72

4.3.2 Considerations about the testing beam modelling

These analyses gave the opportunity to better understand the behaviour of the beam before performing the real test. From a combination of the results obtained in the pre-stressed modal analysis and the theoretical analyses reported in section 2.2.3 and in particular from the work of Lesieture and Davis [10] it is possible to forecast that, if the snap through mechanism could be obtained, the device will be able to be tuned with the application of a pre-load that will also have the effect of increase the voltage output of the device itself.

4.4 Beam footprint optimisation

The beam footprint optimisation analyses puts its roots on the observations made by Baker et al. [3] that proposes a lozenge-shaped footprint of the bistable beam as optimised design which is able to increase the power output by the 30%.

The aim of this part of the work is to understand if the design proposed has a possibility of further developments.

4.4.1 Geometry

For the shape optimisation analyses the geometry is described with parameters that allow modification of the thickness of each layer and the footprint of the beam ranging from a simple rectangular shape to an lozenge, hexagonal shape. The surface area and consequently the volume of active material is kept constant for different footprints. The two extremes of the footprints used for the analyses are shown in Figure 4.27 and the measures of the end and centre width for all the beam footprints are reported in Table 4.17.

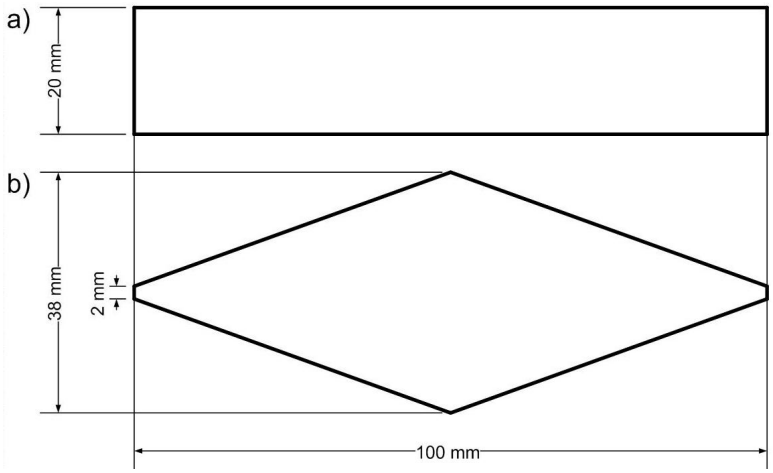

Figure 4.27: Beam footprints plane views:
a) rectangular footprint
b) lozenge-shaped, hexagonal, footprint

Table 4.17: Measures of tip and centre width.

End Width (mm)	Centre Width
2	38
4	36
6	34
8	32
10	30
12	28
14	26
16	24
18	22
20	20

4.4.2 Analysis results

The analysis are run as described in section 4.2.5.

Buckling analysis

Table 4.18 reports the results of the buckling analysis.

Table 4.18: Results of the buckling analysis

Beam Dimensions (mm)	Buckling load (N)				
	1	2	3	4	5
2-38	7.64	21.62	48.35	82.72	133.60
4-36	7.75	22.74	51.77	90.22	144.16
6-34	7.67	23.41	54.42	95.85	155.33
8-32	7.96	25.18	58.79	100.97	166.03
10-30	7.50	24.67	58.90	102.69	164.23
12-28	7.41	25.30	59.32	103.80	166.91
14-26	7.25	25.64	59.51	102.94	169.10
16-24	6.68	25.46	59.01	105.07	165.43
18-22	6.42	25.00	57.42	103.34	164.36
20-20	6.18	25.06	57.35	103.70	164.75

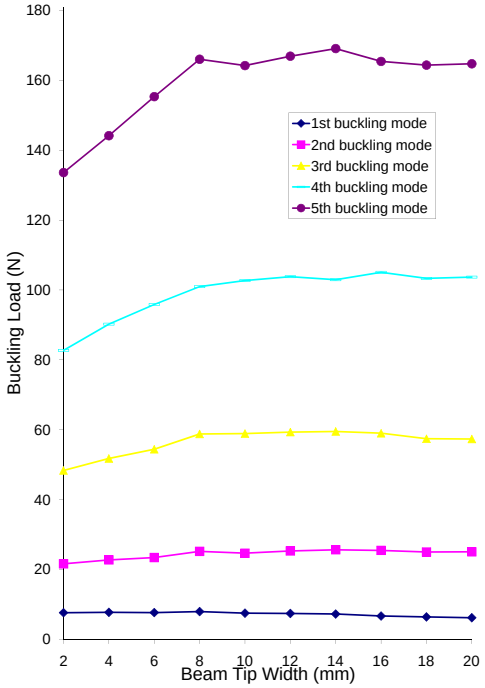

Figure 4.28: Results of the buckling analysis

Modal analysis

Table 4.19 reports the results of the modal analysis.

Table 4.19: Results of the modal analysis

Beam Dimensions	1^{st} Mode (Hz)	2^{nd} Mode (Hz)	3^{rd} Mode (Hz)	4^{th} Mode (Hz)	5^{th} Mode (Hz)
2-38	49.6	154.5	200.9	472.0	650.0
4-36	50.6	175.4	203.7	475.1	680.0
6-34	50.9	194.0	204.4	477.3	699.5
8-32	52.6	210.4	217.8	491.6	724.7
10-30	51.8	206.8	234.5	483.6	729.9
12-28	52.2	208.7	256.5	482.1	752.9
14-26	52.5	209.5	287.0	481.4	743.9
16-24	51.2	208.1	302.7	474.8	728.7
18-22	51.1	206.1	323.3	468.1	728.5
20-20	51.2	206.2	350.6	468.3	728.7

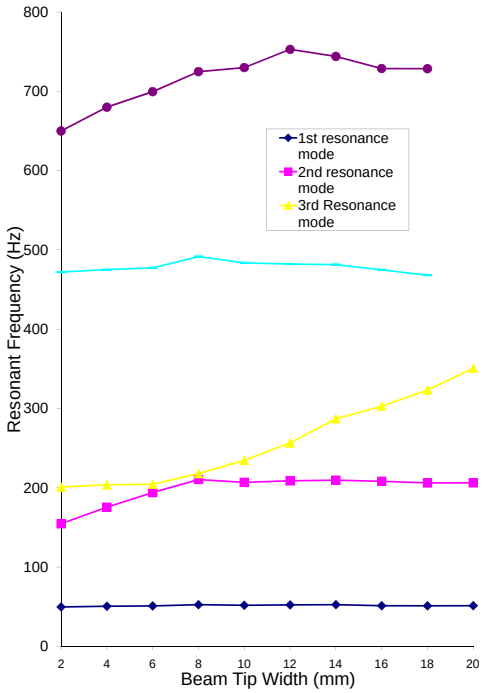

Figure 4.29: Results of the modal analysis

The shapes related to each mode are shown in Figure 4.30 for the 20-20 *mm* and the 2-38 *mm* footprint.

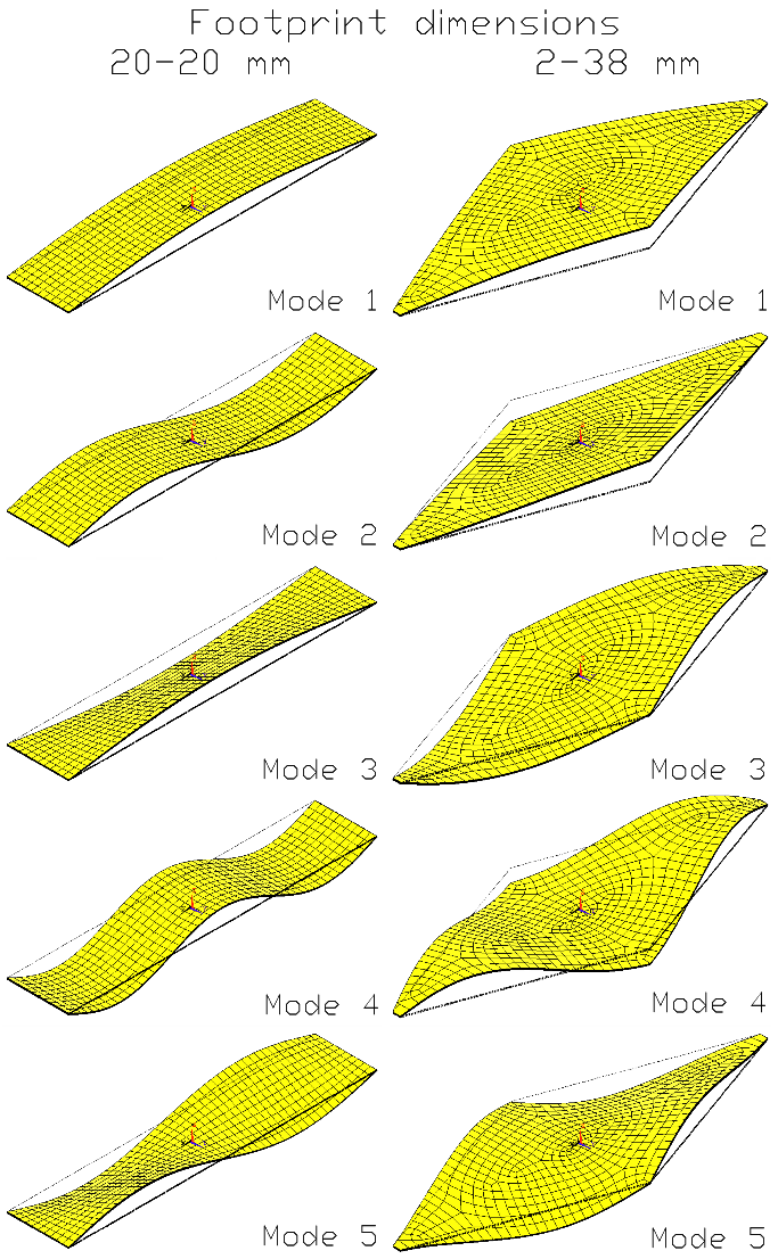

Figure 4.30: Mode shapes for for the 20-20 *mm* and the 2-38 *mm* footprint

Figure 4.29 shows that the second and the third resonance frequency get closer and are almost coinciding for the 8-32 model. It is possible to identify two different trends for this particular modes: one almost horizontal and parallel to the first resonance frequency and the other with a clear slope. The

resonance frequency modes that belong to the first line are purely flexural with a mode shape described by the formula $y_x = sin(\frac{\pi 2x}{L})$ and the modes that belong to the second line are a purely torsional mode around the X axis, as can be also observed comparing the second and the third mode for the two model shown in Figure 4.30. Also the fifth mode is a torsional mode.

Static analysis

Table 4.20 reports the results of the large displacement static analysis.

Figure 4.32 and 4.31 show the displacements for the two extremes of the footprint shapes.

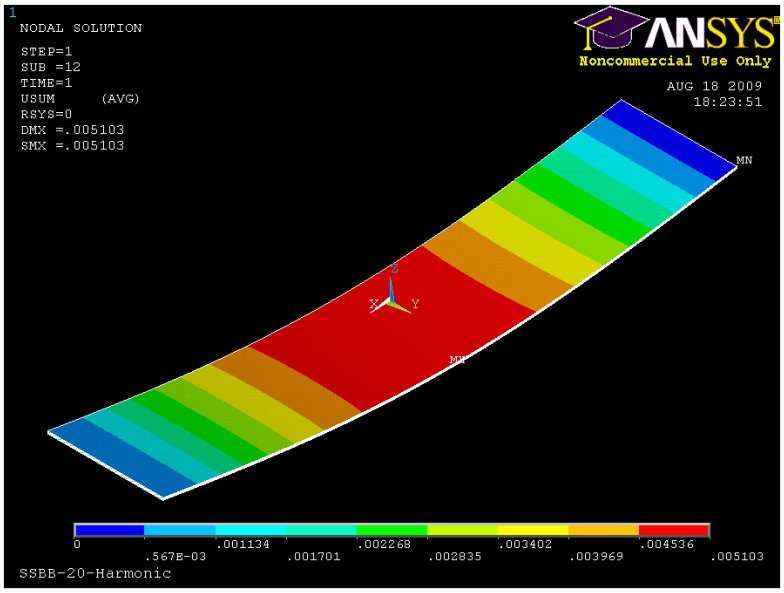

Figure 4.31: Static displacement for the 20 - 20 *mm* footprint shape

Table 4.20: Results of the large displacement static analysis

Beam Dimensions	U_X (mm)	U_Y (mm)	$\sigma_{VonMises}$ (MPa)	σ_X (MPa)		σ_Y (MPa)		σ_Z (MPa)		τ_{XY} (MPa)
2-38	0.43	3.80	58.6	-53.5	57.1	-14.8	14.8	-8.7	8.8	9.1
4-36	0.48	4.00	62.0	-56.9	60.8	-17.7	17.4	-8.9	9.8	9.1
6-34	0.66	4.83	72.6	-63.9	72.1	-17.4	17.6	-8.0	6.3	9.9
8-32	0.56	4.45	66.7	-60.9	66.3	-19.5	19.5	-7.2	6.8	10.6
10-30	0.55	5.44	68.0	-59.4	67.8	-15.7	15.7	-7.5	7.4	8.1
12-28	0.51	4.33	63.4	-57.4	63.3	-15.5	15.2	-6.3	6.3	5.6
14-26	0.53	4.41	67.8	-58.9	68.6	-14.0	14.2	-6.1	6.0	6.6
16-24	0.41	3.91	59.0	-49.4	59.3	-8.8	8.5	-3.3	3.2	3.9
18-22	0.51	4.43	69.2	-58.1	69.7	-10.1	9.9	-0.9	1.0	4.2
20-20	0.67	5.09	85.3	-70.3	86.0	-12.5	12.2	-0.8	0.9	4.0

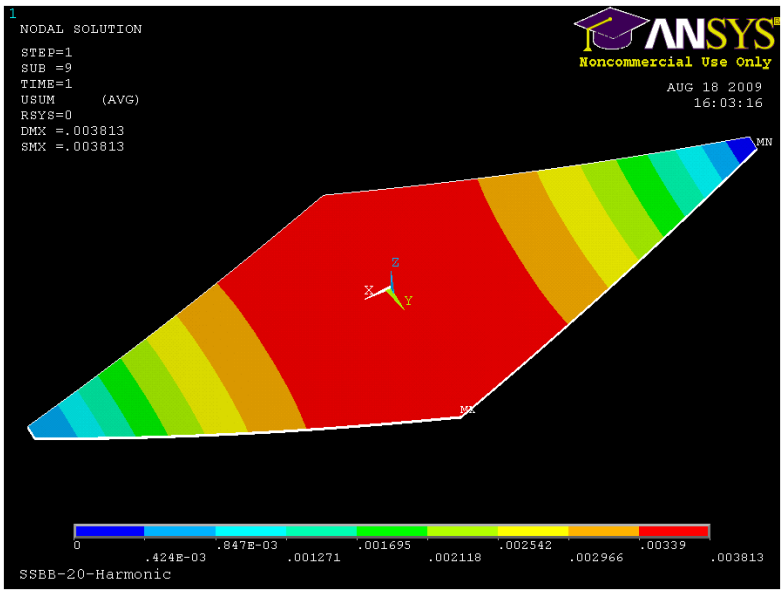

Figure 4.32: Static displacement for the 2 - 38 *mm* footprint shape

Figure 4.34 and 4.33 show the von Mises stress distribution for the two extremes of the footprint shapes.

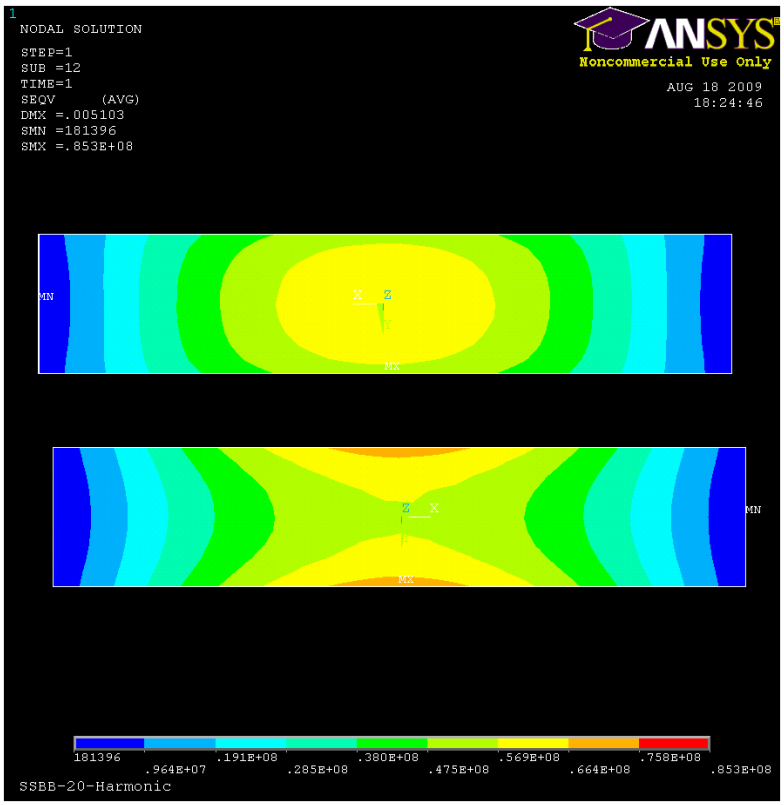

Figure 4.33: Von Mises stress distribution for the 20 - 20 *mm* footprint shape

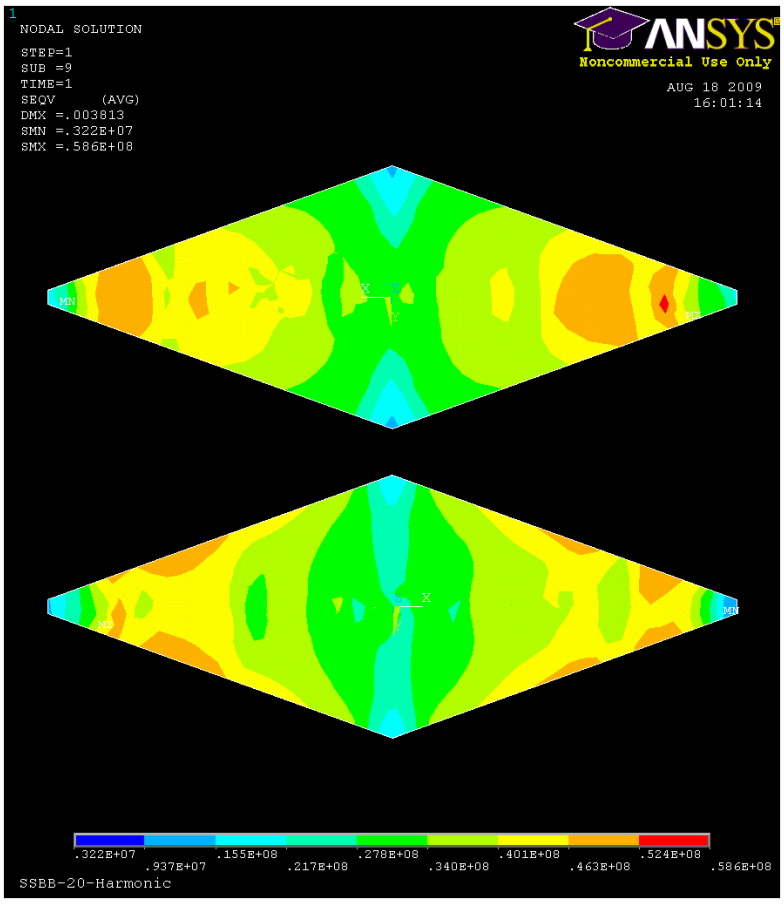

Figure 4.34: Von Mises stress distribution for the 2 - 38 *mm* footprint shape

Harmonic analysis

The results for the harmonic analysis are shown in Figures 4.35 and 4.36.

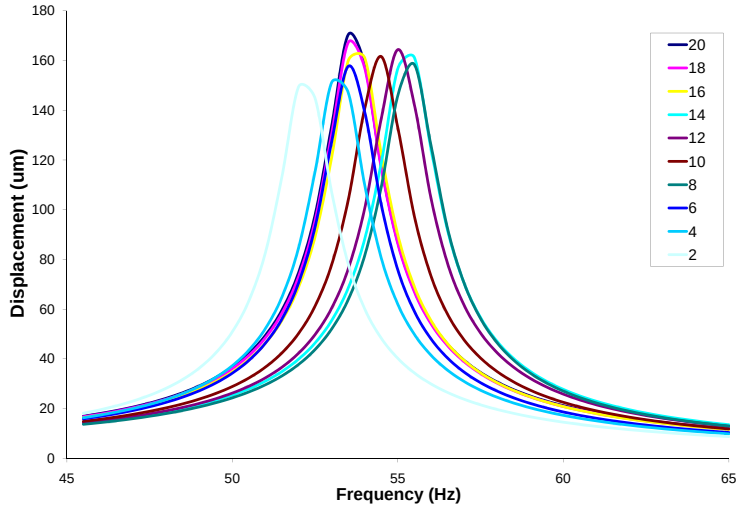

Figure 4.35: Results for the harmonic analysis

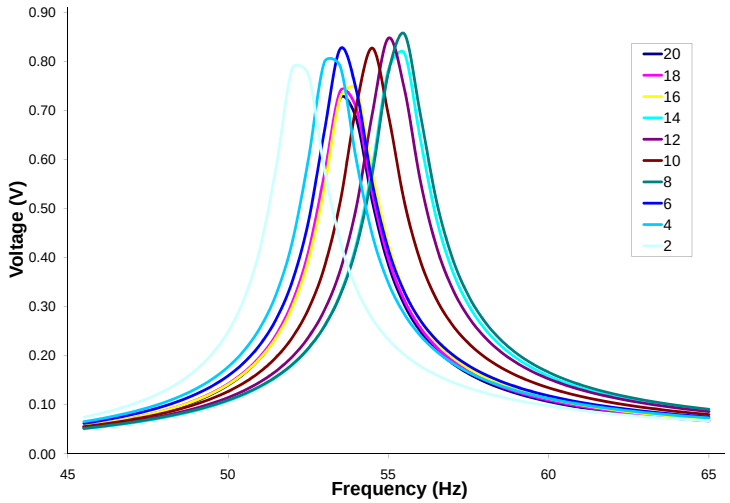

Figure 4.36: Results for the harmonic analysis

The Harmonic analysis confirms the results obtained in the modal analysis, it has to be taken in account that when performing the harmonic analysis the results obtained with the electromechanical model are slightly shifted to higher frequency than the results obtained with the purely mechanical analysis. The different nature of the two analyses performed to obtain these

results must be considered: the modal analysis gives the exact value of the resonance frequency of a structure while the harmonic analysis calculates the response of a structure to an harmonic stimulus. The resonance frequency is identified with a peak in the displacement. The results from the modal and the harmonic analysis are compared and summarized in Table 4.21:

Table 4.21: Results of the harmonic analysis

Beam Dimensions (mm)	Resonance Frequency from Modal Analysis (Hz)	Resonance Frequency from Harmonic Analysis (Hz)	Voltage output (V)
2-38	49.6	53.5	0.72
4-36	50.6	53.5	0.74
6-34	50.9	54.0	0.74
8-32	52.6	55.5	0.82
10-30	51.8	55.0	0.85
12-28	52.2	54.5	0.83
14-26	52.5	55.5	0.86
16-24	51.2	53.5	0.83
18-22	51.1	53.0	0.80
20-20	51.2	52.0	0.78

Observing Figure 4.36 and reading the value of Table 4.21 it is possible to note that by modifying the beam footprint an increase of 20% of the voltage output can be achieved.

The consequence on the power output of the device will be discussed in section 6.1.3.

Chapter 5

Experimental Work

This chapter describes the experimental phase of this research work. The production of the beam is detailed in section 5.1. Section 5.2 describes the experimental set up for the beam electromechanical response test, the procedure followed to run the test and reports the obtained results. Section 5.3 describes the snap through experiments performed to understand the causes of the unsatisfactory results of the beam electromechanical response test.

5.1 Beam manufacture process

The beam has been produced by gluing two Piezo Systems Inc. PSI-5H4E piezoelectric sheets to both sides of an AISI 316 sheet with Circuit Works conductive epoxy. The Piezo Systems Inc. PSI-5H4E piezoelectric sheets come in square plates of 72.4 mm of side and have been cut to match the dimensions of 20 mm $\times$ 72.4 mm.

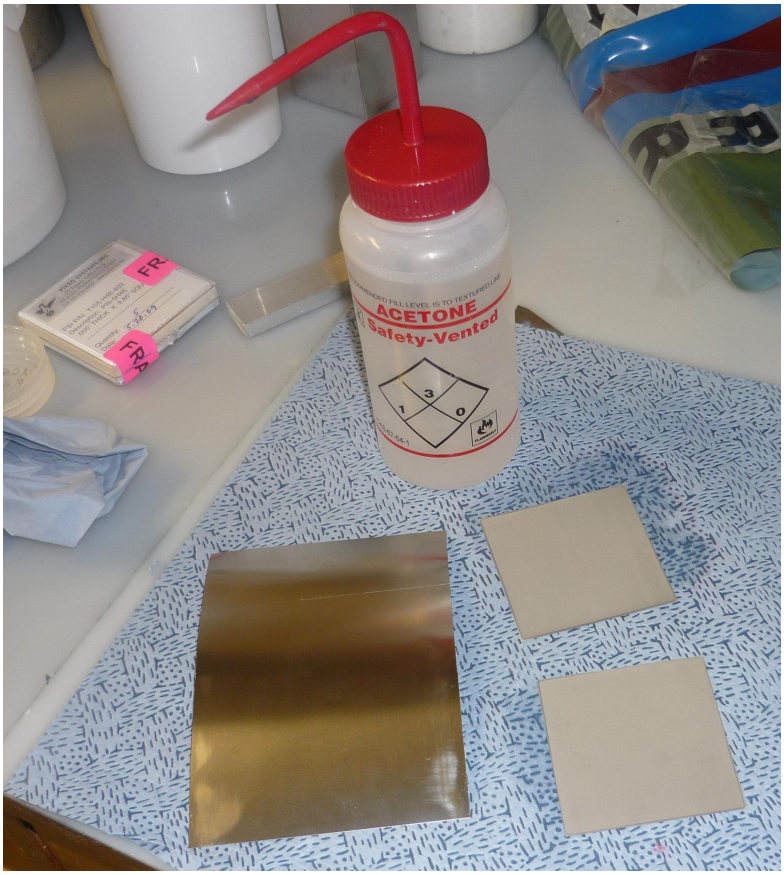

Figure 5.1: Materials used to realize the bimorph beam

A first attempt was done by cutting the piezoelectric sheets with a meter saw and then gluing them to the substrate: the extreme brittleness of the piezoelectric made this option infeasible. During cutting, the vibration induced by the meter saw caused the PZT material to crack and break. After

the cutting, and without a substrate to support it, the piezoelectric material could not be handled and cleaned properly without breaking it.

A second attempt was made fixing the PZT material to a glass plate with wax: even if the PZT material did not break during the cutting, some cracks had propagated through it, and when the PZT specimens were cleaned before gluing them to the substrate, the acetone penetrated the cracks and opened them.

The last attempt was made gluing the piezoelectric to the substrate and then cutting it to the desired dimensions. Both the surfaces was cleaned with acetone to eliminate every trace of grease or impurity. The conductive epoxy was mixed and applied to the substrate surface, the piezoelectric material was then applied.

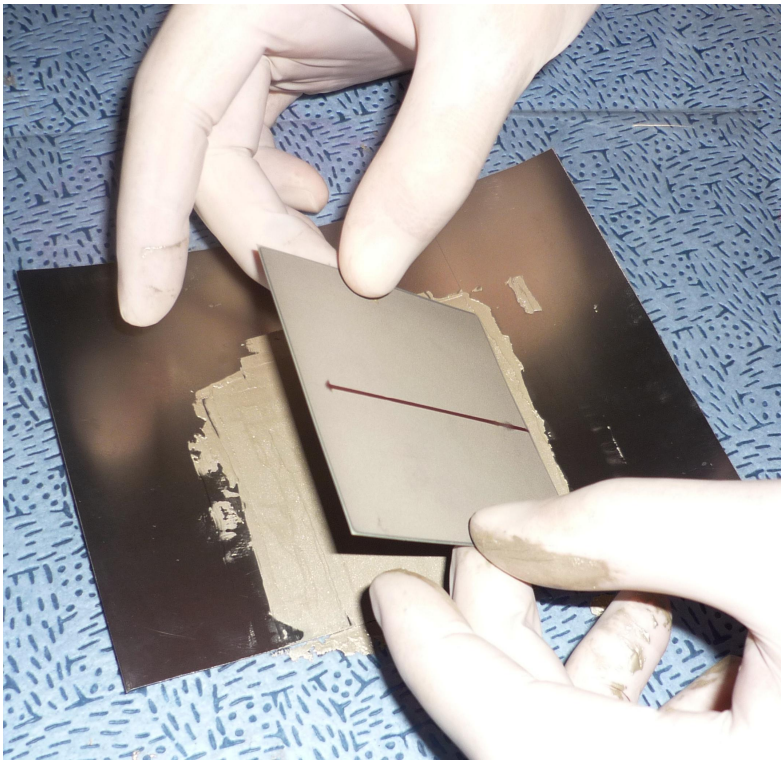

Figure 5.2: Gluing of the piezoelectric material to the substrate with silver epoxy

The glue was cured at a temperature of $60°C$ for 10 minutes and at room temperature for 24 hours between two glass plate and under moderate pressure ($\tilde{5}00\ Pa$). This curing cycle ensures higher mechanical strength and conductivity, at the same time the high temperature of the early stage of the curing reduces the viscosity of the epoxy resin allowing it to spread better and ensuring a better electro-mechanical connection between substrate and PZT material.


GRM
300
GRM
GRM
GRM

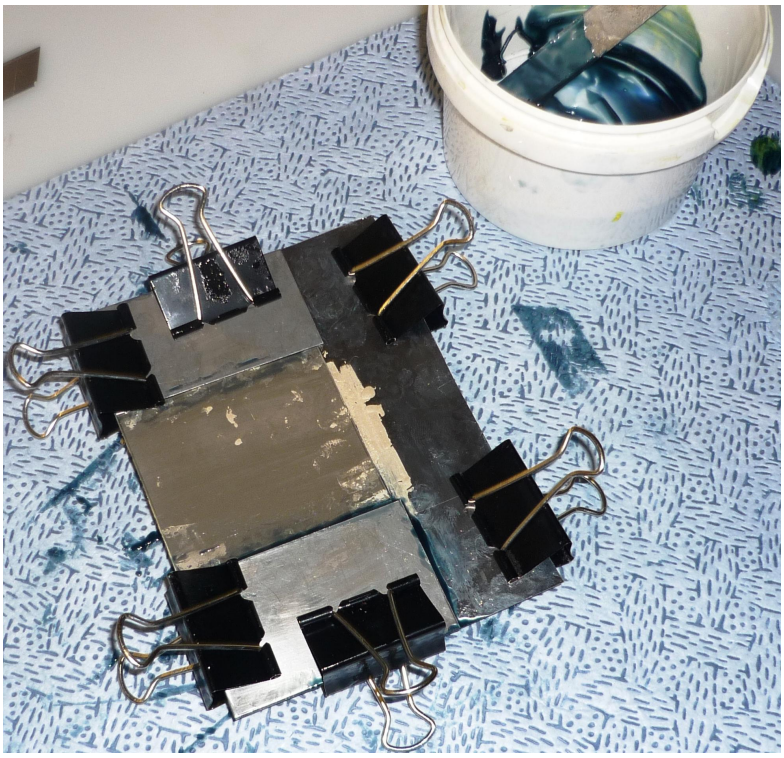

Figure 5.4: Gluing of the stiffeners with Araldite

The plate obtained in this way has then been cut to the desired shape, ground on the side to refine the dimensions, and holes for the fitting on the testing jig have been drilled.

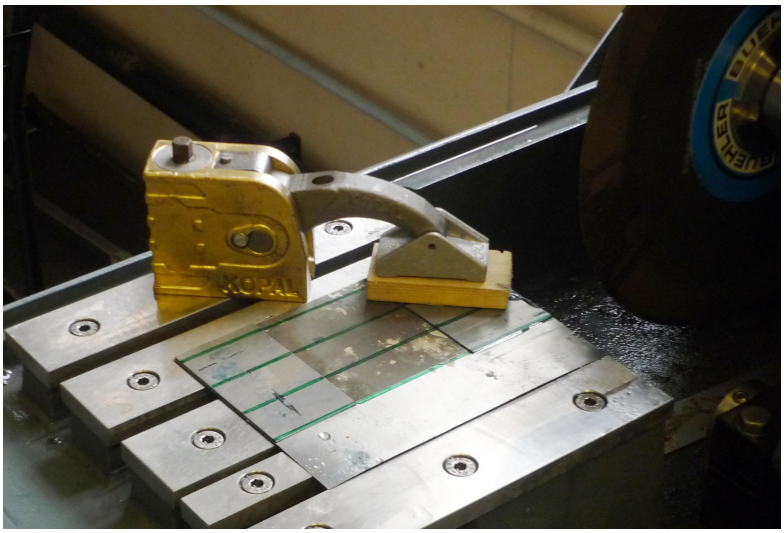

Figure 5.5: Cutting of the laminate with a meter saw, the clamping absorbs the vibrations

Between the various steps of the beam production the beams have been checked with a multimeter to avoid short circuits. Wires have been connected to the beam, using conductive epoxy, accordingly to the bimorph parallel configuration.

5.2 Beam electromechanical response test

5.2.1 General test bed layout

The general test set up is described by the diagram presented in Figure 5.6 and shown in Figure 5.7.

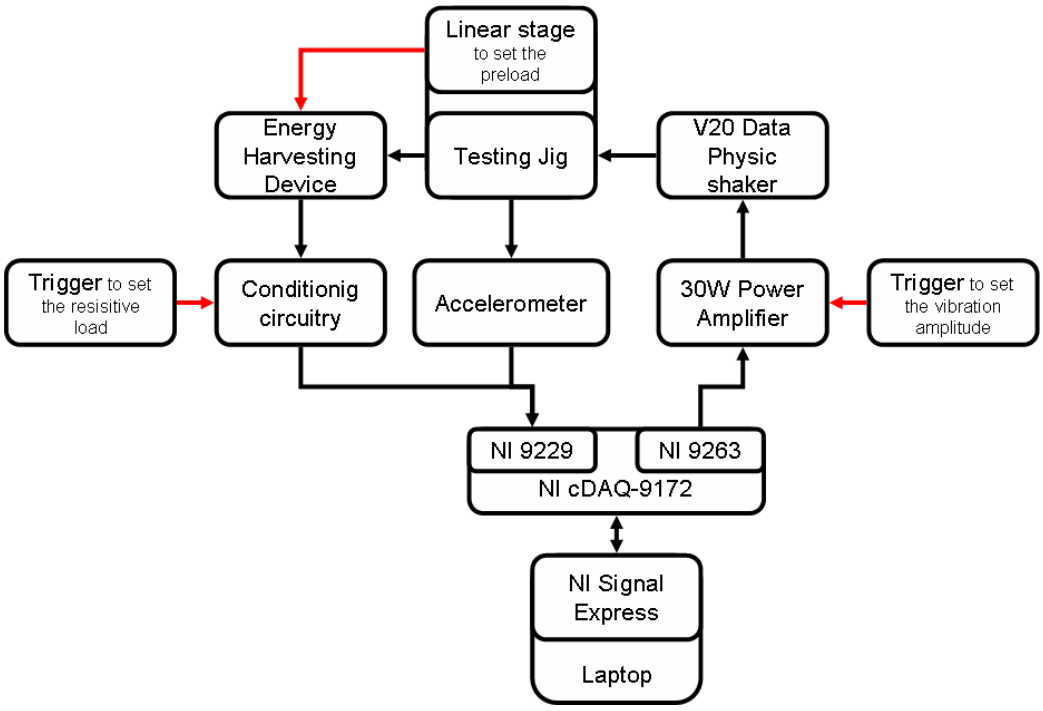

Figure 5.6: Diagram of the experimental set-up

The whole testing apparatus is controlled by a Signal Express program, described in 5.2.1, run by a laptop. The laptop is connected with a USB cable to a NI cDAQ-9172 data acquisition System. A NI 9263 analog output module is fitted on the cDAQ. The driving signal is generated by the Signal Express program and sent to the cDAQ and to the NI 9263, from here the signal is sent to a GW 30W amplifier. A trigger is fitted on the amplifier, this is used to set the amplitude of the vibration. The amplifier drives a V20 Data Physic shaker on which the testing jig is fixed. Further details about the testing jig will be discussed in section 5.2.1. The voltage output of the beam, processed by a conditioning circuit, and the output from the accelerometer fixed on the testing jig are collected by a NI 9229 analog input module and transmitted, through the cDAQ, to the laptop where the data will be recorded by the Signal Express program.

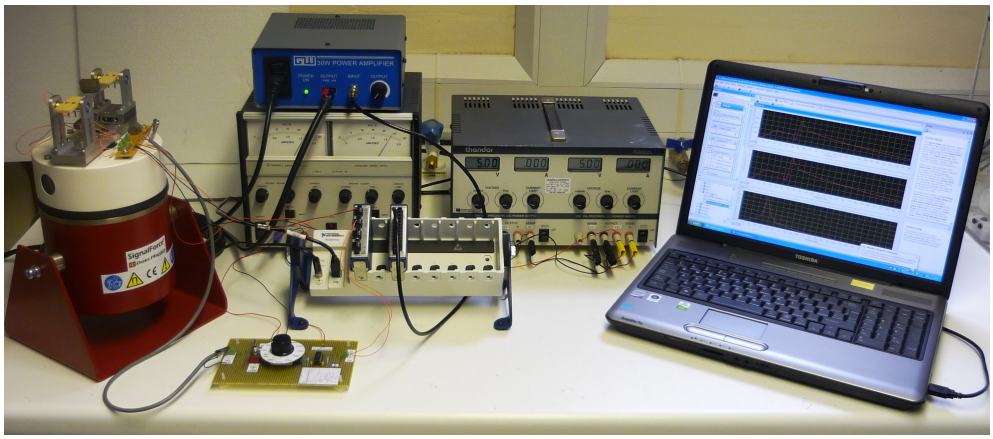

Figure 5.7: Experimental set-up

This experimental set up was developed along the lines of the one used by Worthington and Zhu to run tests on energy harvesting device based on cantilever beams, [25] and [27].

Testing Jig design

The Testing jig has been conceived with the following points in mind:

- it has to be able to control the compression load of the beam;
- it has to solve the problem of the constraint of the beam, as raised by Leland and Wright in [9];
- it has to be as flexible as possible, considering a future optimisation of the device that will involve different shapes and length of the beam.

The general layout of the jig entails a plate that acts as connection between the shaker, giving the vibrational impulse, and four vertical columns that hold the beam. The plate holds several threaded holes that allow the columns and the linear stage to be fixed in different positions making the device suitable to test different kinds of beams. A sealed miniature ball bearing is fitted in every column and holds one end of a rod where the the beam is fixed with screws. The bearings are believed to be able to create a hinged constraint better than the one proposed by Leland and Wright in [9]. The

pre-load is applied to the beam with a SDS precision low-profile ball bearing linear stage equipped with a micrometer, two of the columns are fixed to the stage and can be moved along the main dimension of the beam.

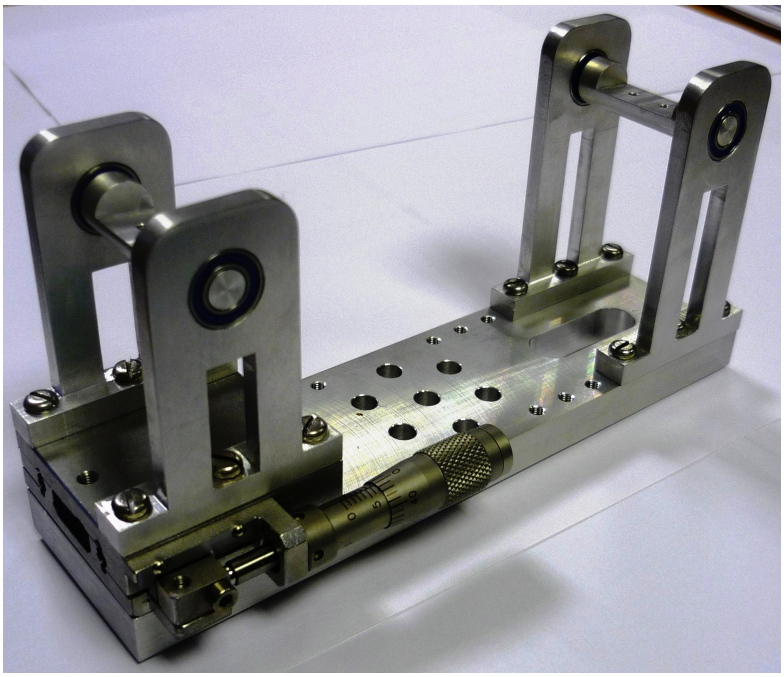

Figure 5.8: Testing Jig

During the experiment different masses will be added to the beam. It is important to minimise the effect of the addition of the mass to the stiffness of the beam. The contact area between the mass and the beam has to be as narrow as possible. A mass with a profile like the one presented in Figure 5.9 is used. Brick-shaped masses will be added to it.

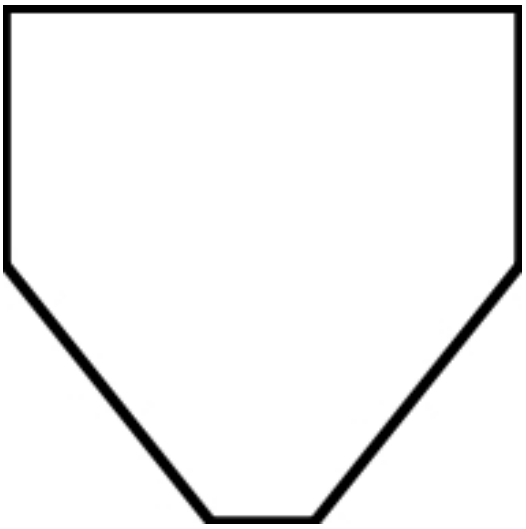

Figure 5.9: Mass profile: designed to reduce the contasct area between beam and mass

The technical drawings of the jig and of the mass are reported in Appendix B.

Testing Software description

The program used to drive the testing apparatus was developed using LabVIEW SignalExpress. This software allows to create a signal that can be transmitted to the NI cDAQ-9172 data acquisition System to control the experiment and simultaneously to record the results of the experiment itself.

Calibration program The program generates an analog sine wave signal at an assigned frequency, and transmits it to a 'DAQmx Generate' block that creates an analog output that it is transmitted, through the cDAQ-9172, to the NI 9263. At the same time the NI 9229 is recording the voltage output from the accelerometer and sending it, through the cDAQ-9172, to a 'DAQmx Acquire' block, that receives the analog input and transmits it to a 'Amplitude and Level' block. Here the peak to peak value of the accelerometer voltage output, i.e. the acceleration of the testing jig, is calculated and

displayed.

Beam testing program The program is composed by a routine that is repeated as a frequency sweep over a defined frequency interval (from Fr_0 to Fr_N) and with a defined number of sub-steps. At a certain frequency Fr_n the routine generates an analog sine wave signal for 3 seconds and transmits it to a 'DAQmx Generate' block that creates an analog output that it is transmitted, through the cDAQ-9172, to the NI 9263. At the same time the NI 9229 is recording the voltage output from the beam and from the accelerometer and sending them, through the cDAQ-9172, to a 'DAQmx Acquire' block. The 'DAQmx Acquire' block waits for two seconds and then starts to measure the analog voltage input. The signal is then processed by a 'Tone Extraction' block that returns the frequency, amplitude, and absolute phase of the signals. The signal from the accelerometer is elaborated by a 'Formula' block that calculates the acceleration in m/s^2. The information about the maximum amplitude of the voltage output from the beam and from the accelerometer and the maximum acceleration in m/s^2 at the assigned frequency are shown on a 'Data View' interface. When the routine is completed the frequency sweep loop increases the frequency of the generated analog signal of an assigned Δ_{freq} and updates the data that is shown on the interface creating a frequency sweep graph of acceleration and beam voltage output.

5.2.2 Testing procedures

The test procedure is organized into three different stages:

1. calibration;
2. testing of the beam;
3. post-processing of the data.

Calibration

The aim of the calibration procedure is to set the amplitude of vibration to ensure a certain acceleration at a defined vibration frequency. For obvious reasons the acceleration is not constant for all the frequencies.

In the case of the experiments presented in this work, the amplitude is set using the program described in section 5.2.1, to ensure an acceleration of 5 m/s^2 at a frequency of 113 Hz. The acceleration is chosen according to the existing literature. The frequency is chosen to match the resonance frequency of the beam found from the previous frequency sweep test.

Testing of the beam

The variables considered in the testing of the beam are:

1. beam pre-load, introduced with the displacement of 0, 0.1 mm, 0.2 mm, 0.3 mm, 0.4 mm at one end of the beam.

2. extra mass of the beam introduced with masses of 13g and 9g.

Even if different resistive loads were available in the conditioning circuit, it was chosen to perform all the tests with an open circuit configuration.

Post-processing of the data

The data was post-processed to rescale the voltage output of the beam to a constant acceleration by using the following procedure:

1. calculation of a ratio between the acceleration at the calibration frequency and at the recorded frequency;

2. multiplication of the ratio with the voltage output of the beam.

5.2.3 Test results

The results of the tests are presented as recorded in Figures 5.10, 5.12 and 5.14 and after the post-process in Figures 5.11, 5.13 and 5.15.

Results without extra mass

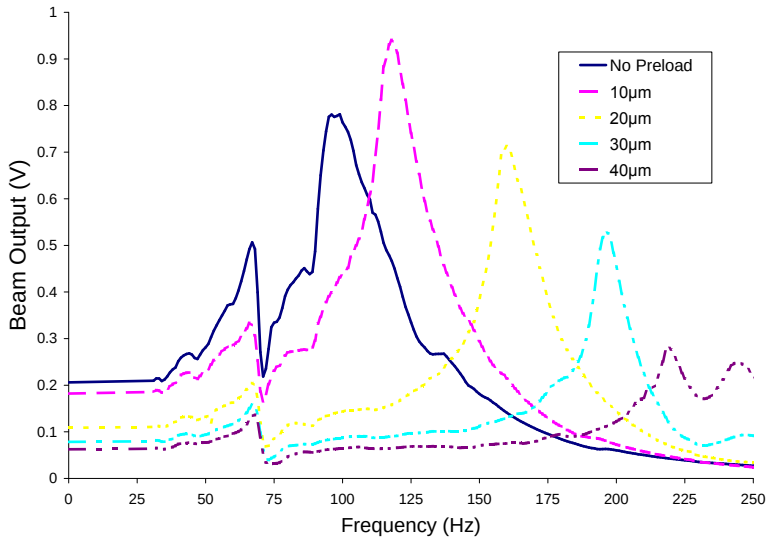

Figure 5.10: Recorded Results without extra mass

The beam presents a peak in the voltage output corresponding with the resonance frequency, Table 5.1 shows the resonance frequency and the voltage output of the beams. Before the beam response peak there is a another peak at 67 Hz, this is believed to be a response of all the testing system: the shaker plus the testing jig and the beam itself.

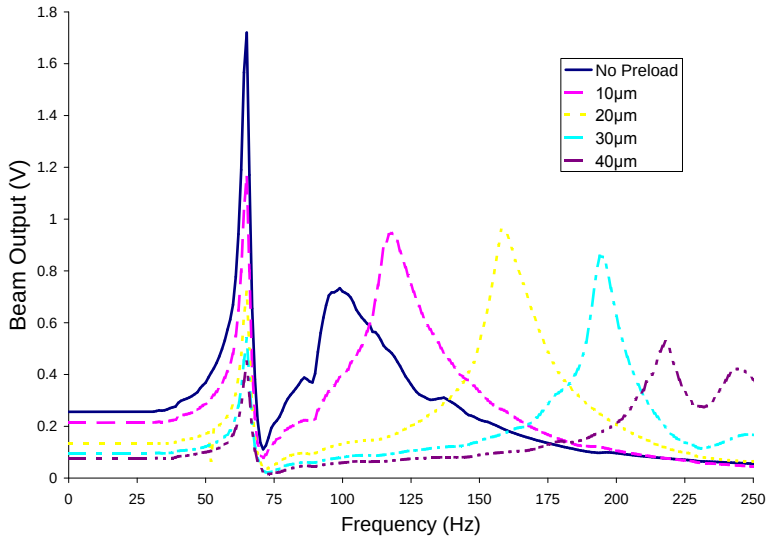

Figure 5.11: Post-processed results without extra mass

After the post-process of the data the beam responses present the same resonance frequency but the peak value is modified, as can be seen in table 5.1. The system response is accentuated by the data post-process, this value is not of interest for the purposes of this research work.

Table 5.1: Results of the test without extra mass

Beam Tip Displacement (mm)	Resonance Frequency (Hz)	Beam output (V)	
		Recorded	Post-processed
0	97	0.78	0.73
0.1	118	0.94	0.95
0.2	160	0.71	0.94
0.3	196	0.53	0.84
0.4	219	0.28	0.51

It is possible to observe that the pre-load, applied with a displacement of one of the beam end, increases the resonance frequency and, except for the 0.1 and 0.2 mm displacement, decreases the voltage output peak.

Results with 13g of extra mass

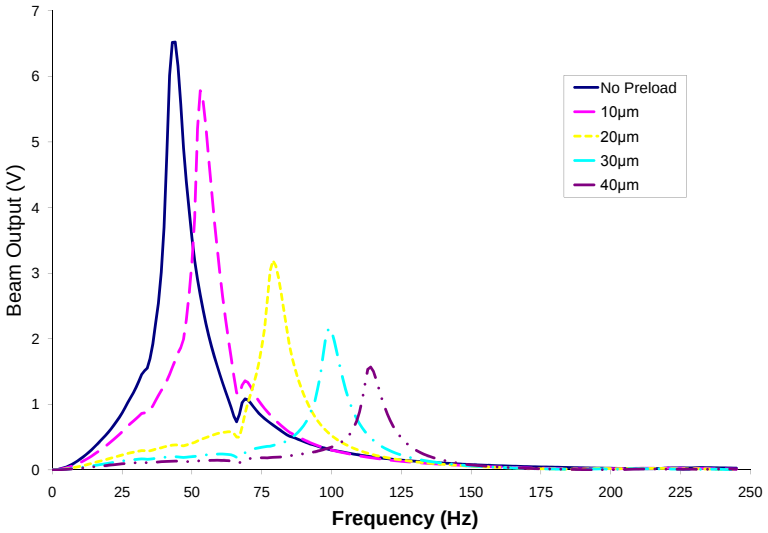

Figure 5.12: Recorded Results with 13g of extra mass

The beam present a peak in the voltage output corresponding with the resonance frequency, Table 5.2 shows the resonance frequency and the voltage output of the beam. As in the above results the system response peak is at a frequency of 67 Hz.

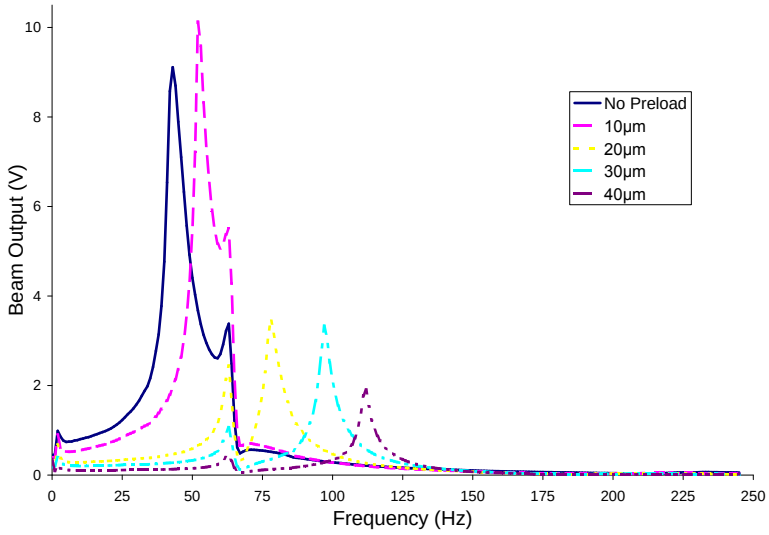

Figure 5.13: Post-processed results with 13g of extra mass

After the post-process of the data the beam responses present the same resonance frequency but the peak value is modified, as can be seen in Table 5.2.

Table 5.2: Results of the test with 13g of extra mass

Beam Tip Displacement (mm)	Resonance Frequency (Hz)	Beam output	
		Recorded	Post-processed (V)
0	44	6.52	9.11
0.1	53	5.78	10.12
0.2	73	3.19	3.47
0.3	99	2.16	3.33
0.4	114	1.57	1.91

Results with 22g of extra mass

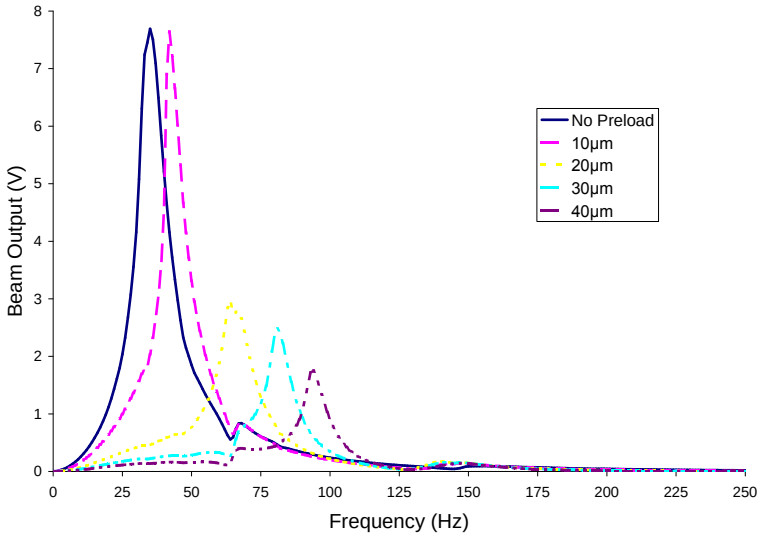

Figure 5.14: Recorded Results with 22g of extra mass

The beam present a peak in the voltage output corresponding with the resonance frequency, Table 5.3 shows the resonance frequency and the voltage output of the beam. As in the above results the system response peak is at a frequency of 67 Hz.

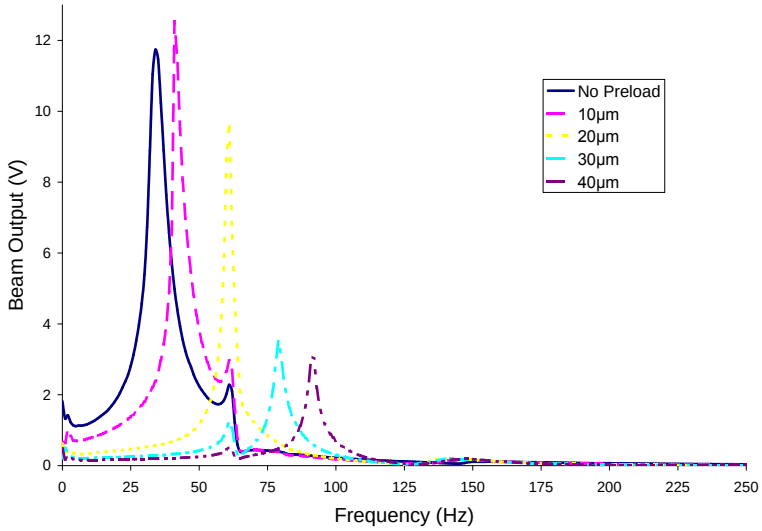

Figure 5.15: Post-processed results with 22g of extra mass

After the post-process of the data the beam responses present the same resonance frequency but the peak value is modified, as can be seen in table 5.3.

Table 5.3: Results of the test with 22g of extra mass

Beam Tip Displacement (mm)	Resonance Frequency (Hz)	Beam output	
		Recorded	Post-processed (V)
0	34	7.69	11.55
0.10	41	7.64	12.53
0.20	64	2.97	9.68
0.30	81	2.48	3.54
0.40	94	1.75	3.08

System response

Figure 5.16 shows the acceleration recorded by the accelerometer fitted on the testing jig during the beam response test.

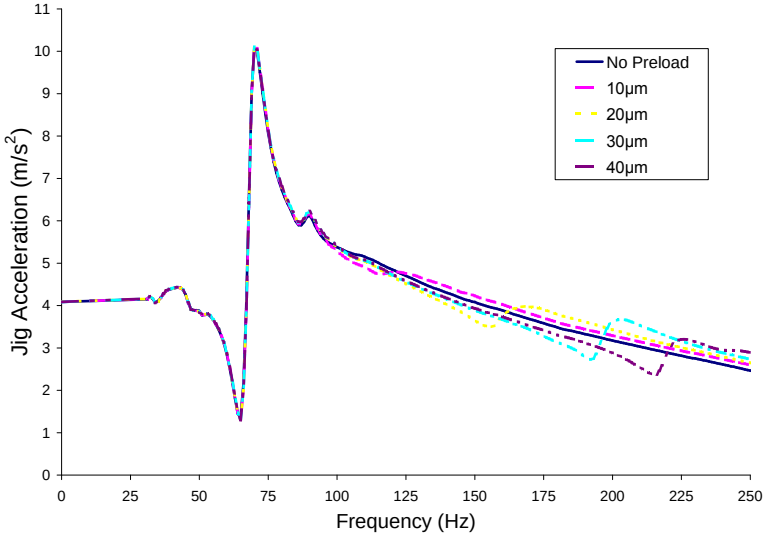

Figure 5.16: System acceleration response

It is possible to observe that the system presents a peak in its acceleration at around 67 Hz. This is believed to be a non linear response of the system constituted by the shaker and the testing jig. This effect marginally influences the results, however it is always possible to distinguish the beam response from the whole system response.

The results of the test will be discussed in section 6.2.2, the differences between the test results and the finite element modelling will be discussed in section 6.3.1.

5.3 Snap through experiments

As in the previous set of tests the snap through was not observed, and after the modification proposed in section 6.2.4, a series of tests to observe the phenomenon of the snap through have been performed with metallic uniform beams.

5.3.1 Beam dimensions

The test will be performed on three different beams dimensioned to have the same buckling load.

The Euler Buckling load is defined by formula 3.19:

$$P_{cr} = \frac{\pi^2 EI}{(KL)^2} \tag{5.1}$$

To have comparable results the buckling load BL has to be kept constant among the three beams. The material and the length is the same for the three beams, which means that the moment of inertia must be the same for the three different beams.

The formula of the momentum of inertia I is:

$$I = \frac{w \cdot t^3}{12} \tag{5.2}$$

where w and t are the width and the thickness of the beam.

Inverting equation 5.2 it has been possible to calculate the beam dimensions summarized in Table 5.4.

Table 5.4: Dimensions of the beam for the snap through test

Beam	Width (mm)	Thickness (μm)	Moment of inertia (mm^3)
1	20	203	0.0139
2	10	254	0.0137
3	6	305	0.0142

The extra mass of 30 g, shown in figure 5.17, is added to the centre of the beam. The mass is shaped to reduce the area of the beam that is stiffened.

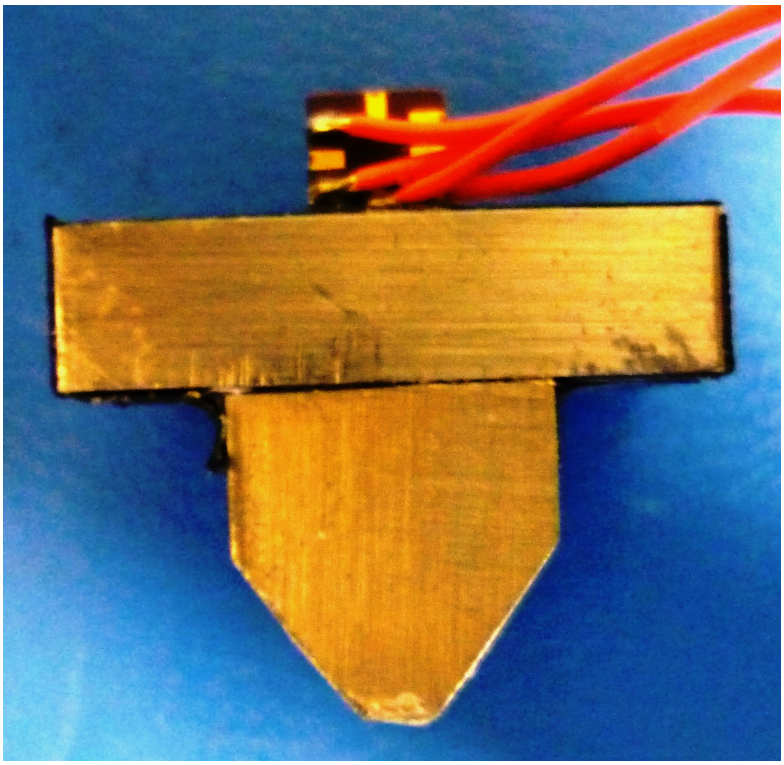

Figure 5.17: Extra 30 g mass added to the centre of the beam. The contact area is minimised to reduced the stiffened area.

The technical drawing of the mass is reported in Appendix B.

5.3.2 General test-bed layout

The testing station and the software used for the snap through tests are directly derived from the one described in section 5.2. The general test set up is describe by the diagram presented in Figure 5.18.

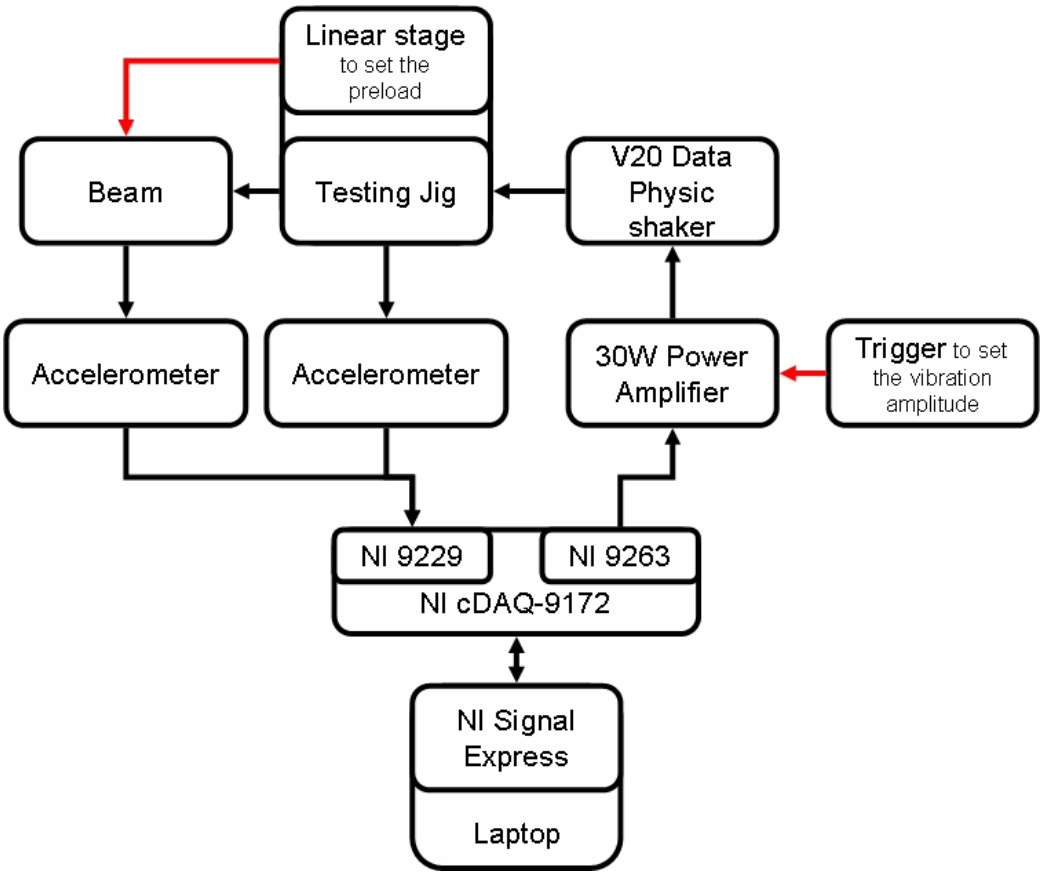

Figure 5.18: Diagram of the experimental set-up

An extra accelerometer is fixed in the centre of the beam on top of the inertial mass in order to record the response of the beam as shown in figure 5.19.

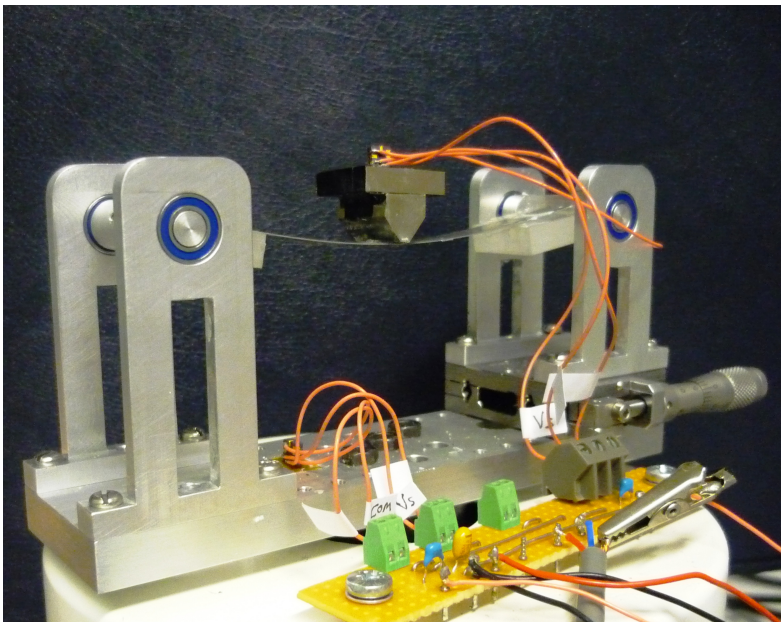

Figure 5.19: Test set up for the snap trough experiment. One accelerometer is fitted on the testing jig and one on the inertial mass glued to the centre of the beam.

Testing Jig modifications

The jig was slightly modified to be able to experiment with two different boundary conditions:

1. simply supported, as shown in figure 5.20. A PMMA block is glued on the rod that is held by two bearings, and the beam tip is glued on the PMMA block.

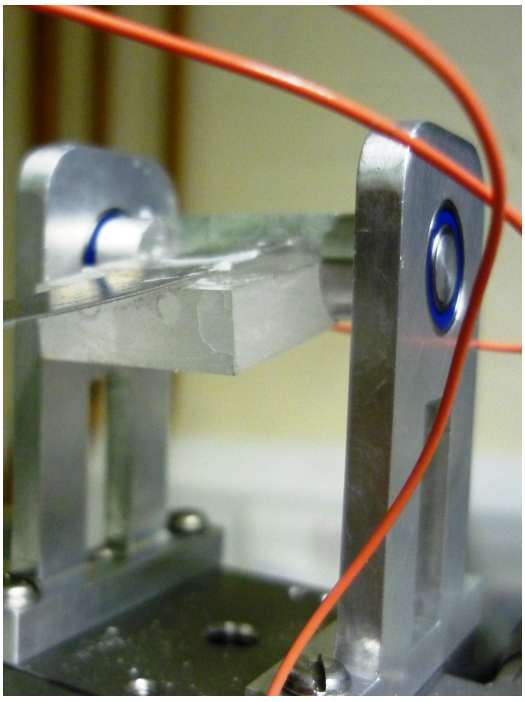

Figure 5.20: Hinged constrain

2. fixed-fixed as shown in figure 5.21. A PMMA rod is glued to the columns that support the hinged constraints, the beam tip is glued to the PMMA rod.

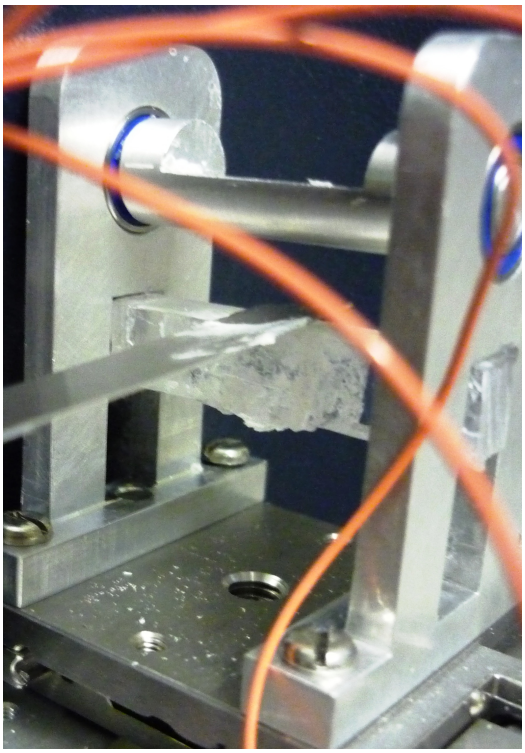

Figure 5.21: Fixed constrain

A first problem is observed when trying to fix the beams to the testing jig. A beam has six degrees of freedom, a hinge suppresses three degrees of freedom blocking the displacements but not the rotations: a simply supported beam is then statically determinate. When introducing a relative position between the two hinges, as in this case, a further constraint is added and the structure becomes statically indeterminate. Therefore, to force the beam to respect all the boundary conditions, pre-stresses are introduced in it while fixing it to the testing jig. This problem was solved with a higher accuracy in the beam cutting and alignment of the parts on the testing jig.

Testing Software modifications

The program is similar to the one described in paragraph 5.2.1. It has been modified to be able to record and process the signals from both the accelerometer at the same time and display them on the same graph. When the

acceleration of the beam presents a peak and moves away from the testing jig acceleration this means that the beam is at its resonance frequency. The snap through can be visually identified while performing the experiment.

5.3.3 Testing procedure

The experiment is performed by introducing a displacement in one of the tips of the beam from an elongation of 0.3 mm to a compression of 0.9 mm.

The experiment is a frequency sweep to visually identify the frequency of an eventual snap through and record it as an acceleration response of the beam. Performing the experiment in this way also allows the identification of the resonance frequency of the beam.

5.3.4 Test results

Figures 5.22 and 5.23 report the results of the tests as resonance frequency against the beam tip displacement. The displacement is assumed to be positive when it compresses the beam and negative when it stretches the beam.

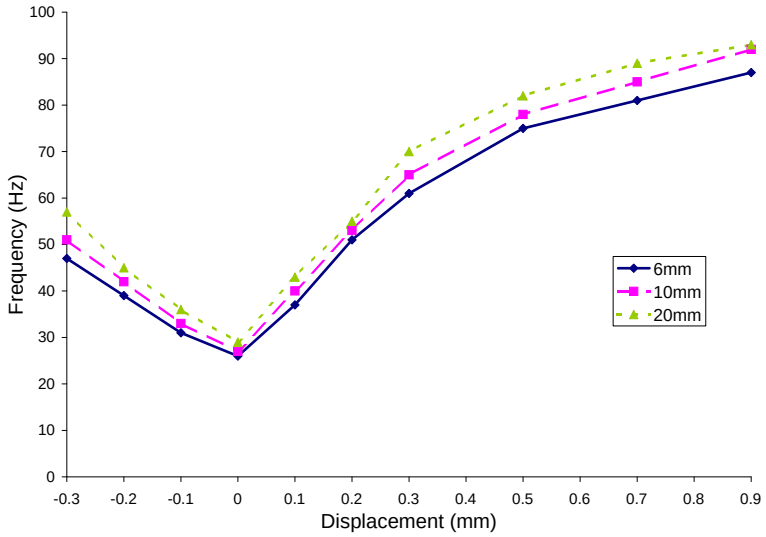

Figure 5.22: Resonance frequency of the simply supported beam versus the beam tip displacement for the different beam size

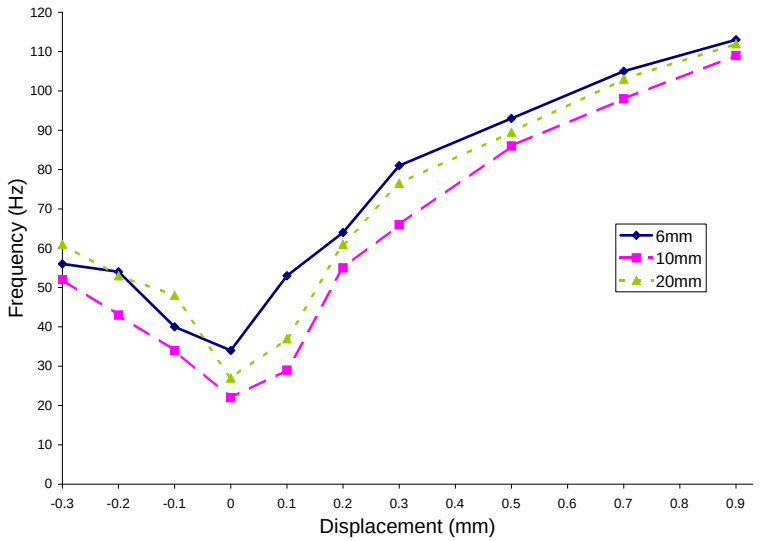

Figure 5.23: Resonance frequency of the fixed-fixed beam versus the beam tip displacement for the different beam size

The obtained results are in accordance with the results obtained from the beam electromechanical response test, but not with what was found in literature and in the calculation of the finite element modelling. The results

will be discussed in section 6.2.3, the differences between the test results and the finite element modelling will be discussed, along with the results of section 6.2.2 in section 6.3.1.

Chapter 6

Discussion

This chapter reports the discussion of the results obtained during the research work. The results of the finite element modelling phase and of the experimental phase are treated separately in section 6.1 and 6.2. An explanation about the differences in the results obtained in the two phases is given in section 6.3.

6.1 Finite element modelling results

In this section the main results from the finite element modelling stage described in Chapter 4 will be discussed and analysed.

6.1.1 Approaching models

The aim of validating the final model while building it through a series of models with increasing complexity is completely achieved. Overall, the different models show a good consistency between them in the results from the different analyses and also with the analytical results. All the discrepancies between the results have been explained. The SOLID45 & SOLID5 model is believed to be very suitable to qualitatively simulate the behaviour of the energy harvesting device. By modifying the properties of the SOLID5 elements it has been possible to create the electro-mechanical model of the beam, which was the goal at this stage of the work.

Another important result obtained at this stage is represented by the understanding of the effect of the pre-load on the resonance frequency of the beam. It is possible to conclude that the pre-load represents, at least theoretically, a tool to tune the resonance frequency of a bimorph, simply supported bi-stable beam based energy harvesting device.

6.1.2 Testing beam model

The results from the testing beam model have to be carefully considered: the model does not take into account certain aspects of the real beam, such as the damping effect of the glue layer and the energy absorption of the hinged constraints, that are fundamental in order to create an exact model of the beam. Besides this, another difference between the modelled and the real beam is in the tolerances. The modelled beam is perfectly straight and the hinges at the two extremes of the beam are perfectly aligned. In the real beam, difficulties have been found in aligning the beam with the testing Jig

and applying the pre-load as a perfectly compressive load.

From the testing beam model, information about the tunability of the energy harvesting device was gathered.

- As expected the device can be tuned by adding a mass to the centre of the beam. The generic formula for the natural frequency of a structure is $\omega_{res} = \sqrt{K/M}$ (where K is the stiffness and M the mass), it is clear that adding mass to the structure will result in a reduction of the resonance frequency.

- The second mechanism that appears evident to be usable for a frequency tuning of the device is the pre-load. The finite element analyses show that to an increase of the axial pre-load corresponds a reduction of the resonance frequency of the beam.

The two mechanisms could be used to tune the resonance frequency of the bimorph, simply supported bi-stable beam based energy harvesting device to the environmental vibrations.

The missing results from this simulations are from the pre-stressed harmonic analysis: this analysis could have given an indication of the real benefit of the axial pre-load on the voltage output of the device.

As the output of the electro-mechanical analyses is the electric potential difference between the $Node_{GR}$ and $Node_{SI}$ in Figure 4.13, it is necessary to estimate the power output of the device. To do this, the method used by Who et al. in [28] was followed. The power output was calculated across a resistor installed between $Node_{GR}$ and $Node_{SI}$ as shown in figure 6.1.

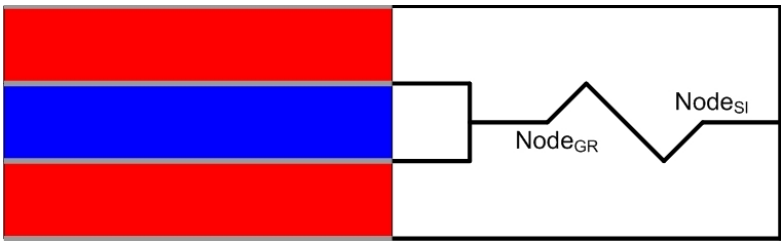

Figure 6.1: electrical connections of the beam

The electrical outputs of a piezoelectric energy harvesting device directly connected to a load resistor can be expressed by Joule's law:

$$P = V \cdot I \tag{6.1}$$

where P is the electric power, V is the voltage and I is the electric current, and by Ohm's law:

$$V = R \cdot I \tag{6.2}$$

where R is the resistance. The power output can be then written as:

$$P = \frac{V^2}{R} \tag{6.3}$$

To define the resistance of the resistor between $Node_{GR}$ and $Node_{SI}$ the formula used by Zhu in [28] for the optimised resistance was used:

$$R_{opt} = \frac{1}{2\pi f_{res} C_P} \tag{6.4}$$

where f_{res} is the resonance frequency of the beam and C_P is the the capacitance of the piezoelectric calculated as:

$$C_P = \epsilon_0 \epsilon_{33} \frac{A_{PZT}}{t_{PZT}} \tag{6.5}$$

where A_{PZT} and t_{PZT} are the area and the thickness of the piezoelectric material, ϵ_{33} is its dielectric constant and ϵ_0 is the permittivity of free space.

A constant resistance of 5 $k\Omega$ is also considered for the calculation of the

beam outputs.

The power output for the testing beam model is summarised in Table 6.1.

Table 6.1: Testing beam model outputs calculated from the harmonic analysis results

Added Mass (g)	Resonance Frequency (Hz)	Voltage output (V)	R ($k\Omega$)	Current output (μA)	Power output (μW)
	R = R_{opt}				
+ 0	63	1.31	7.7	170	222
+ 13	28	0.94	17.4	54	51
+ 22	22	0.72	22.1	33	23
	R = constant				
+ 0	63	1.31	5.0	262	343
+ 13	28	0.94	5.0	188	177
+ 22	22	0.72	5.0	144	104

It has to be remarked that the response of the beam to the added mass is in contrast with the available literature. In their work, Roundy and Wright state that the power output is proportional to the added mass [20]. It is believed that the obtained results are incorrect: the mass has the right effect in shifting down the resonance frequency but it also decreases the displacements in the beam and consequently the stresses and the voltage output. After working on the property of the MASS21 element, a solution could not be found. The results of the voltage output for the models with 13 and 22 g of added mass are expected to be confuted by the experimental results. It is believed that by using a realistic model of the added mass, it could bring the correct result.

6.1.3 Shape optimisation analysis

The same path explained in section 6.1.2 was followed to calculate and compare the power output of various shapes considered for the beam footprint

optimisation.

The power output of the energy harvesting device is dependent on both the shape of the beam and the resistance of the resistor. Initially, in this work an optimised resistance, which is different for various beams, was used for the calculation of the beam power output. With this method, the real benefit of the shape optimisation study could have been hidden. In order to rectify this problem, a constant resistance of 5 $k\Omega$ was considered for all the various beams for the calculation of the beam power output.

The peak values of current and power output are reported in Table 6.2. Figures 6.2 and 6.3 show the power values on the interval of the frequency sweep.

Table 6.2: Shape optimisation models outputs calculated from the harmonic analysis results

Beam Dimensions (mm)	Resonance Frequency (Hz)	Voltage output (V)	R ($k\Omega$)	Current output (μA)	Power output (μW)
	R = R_{opt}				
2-38	53.5	0.72	5.45	133	96
4-36	53.5	0.74	5.45	136	100
6-34	54.0	0.74	5.40	137	102
8-32	55.5	0.82	5.26	155	127
10-30	55.0	0.85	5.31	160	135
12-28	54.5	0.83	5.35	154	128
14-26	55.5	0.86	5.26	163	139
16-24	53.5	0.83	5.45	151	125
18-22	53.0	0.80	5.51	145	116
20-20	52.0	0.78	5.61	140	110
	R = constant				
2-38	53.5	0.72	5.0	145	105
4-36	53.5	0.74	5.0	148	109
6-34	54.0	0.74	5.0	149	110
8-32	55.5	0.82	5.0	163	133
10-30	55.0	0.85	5.0	169	143
12-28	54.5	0.83	5.0	165	137
14-26	55.5	0.86	5.0	171	146
16-24	53.5	0.83	5.0	165	136
18-22	53.0	0.80	5.0	160	127
20-20	52.0	0.78	5.0	157	123

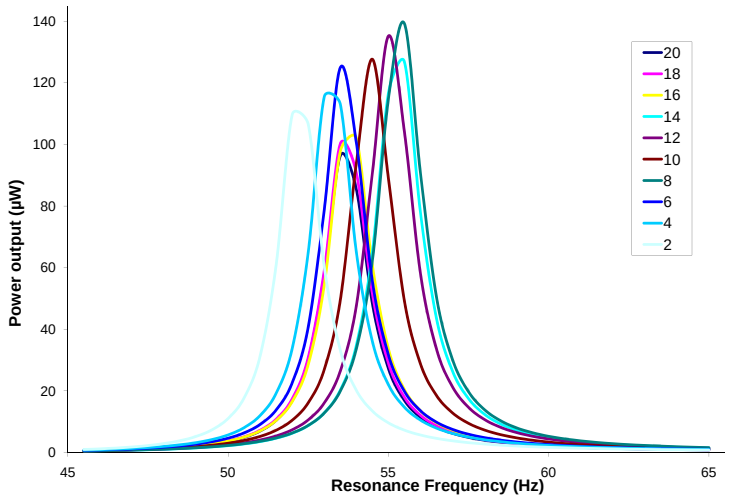

Figure 6.2: Power output calculated from the harmonic analysis results for the different beam shapes with R = R_{opt}

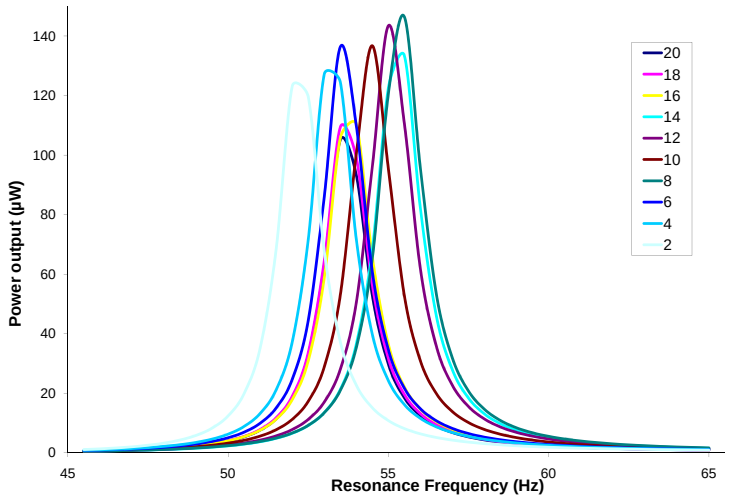

Figure 6.3: Power output calculated from the harmonic analysis results for the different beam shapes with R = 5 $k\Omega$

By plotting the peak value of the power generated by the device and calculating the trend, it is possible to identify the shape that ensures maximum power output, as shown in Figure 6.4.

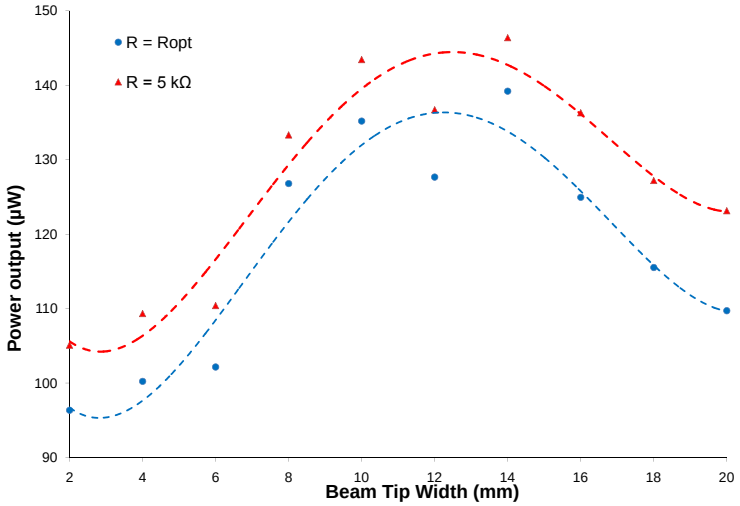

Figure 6.4: Power output peaks and trend line for optimised and constant resistance

The two curves present the same trend, the maximum power output can be obtained in the region of the curve where the ratio of beam centre and beam tip width is between 3 (10-30 *mm* footprint) and 1.86 (14-26 *mm* footprint). The hypothesis that was made by Baker et al. [3] is confirmed: a shape optimisation study can lead to a power increase of 40%.

6.2 Experimental work

6.2.1 Beam manufacture process

The benefits expected from the autonomous production of the beam, i.e. the knowledge of the used materials as explained in section 3.3 did not compensate the experienced difficulties.

The PZT material was almost impossible to handle in its off-the-shelf form: its extreme brittleness made it difficult to cut, clean and process in general. Even when glued on the substrate, it appeared brittle and was difficult to cut and handle.

By starting with a number of PZT sheets enough to produce 12 specimens, it has been possible to produce only one specimen. A lot of material was lost during the efforts to understand the best cutting procedure. Some specimens broke after the cutting and the grinding because of crack propagation. In some specimens a short circuit between the electrodes was found.

Autonomously producing the test specimens has been an extremely time consuming and onerous activity. It is recommended, for further studies on this subject, to buy an off-the-shelf bimorph beam and focus the efforts on the hinge design.

6.2.2 Beam electromechanical response test

Figures 6.5 and 6.6 are a summary of the obtained results.

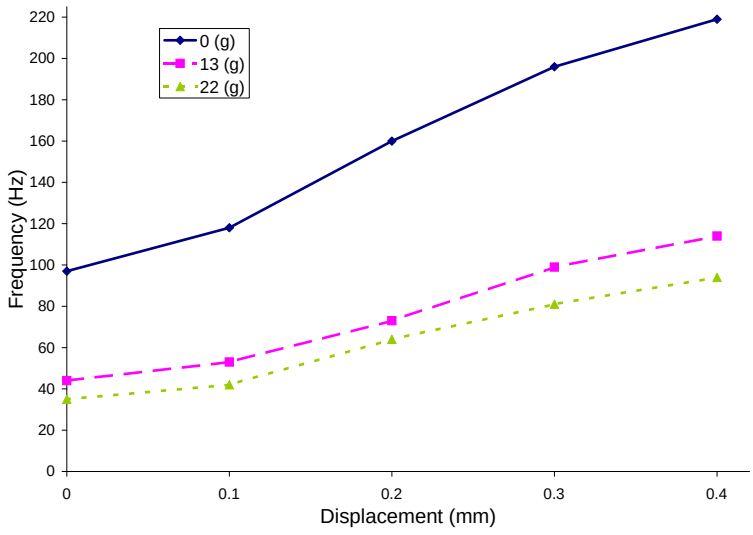

Figure 6.5: Natural Frequency of the beam versus the beam tip displacement with different extra masses

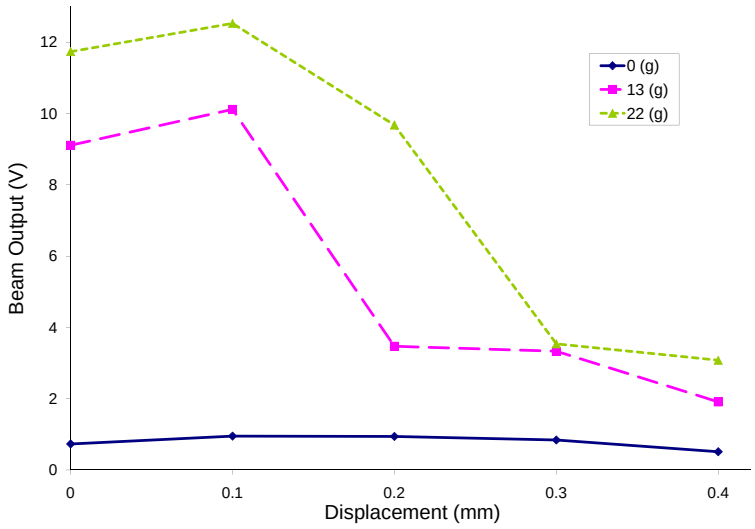

Figure 6.6: Beam output versus the beam tip displacement with different extra masses

From the graphs above, observations about the effect of the added mass and the pre-load can be made.

The extra mass modifies the response and the voltage output of the beam as expected: an increase of the mass causes a reduction of the resonance frequency and an increase of the voltage output.

When the pre-load is increased the resonance frequency of the beam increases, as shown in Figure 6.5, and the voltage output decreases, as shown in Figure 6.6. This result is in contrast to the finite element results presented in section 4.3 and the available literature [9], [3] and [19]. This is believed to be caused by the fact that the beam, when axially loaded assumes a curved deformed shape and does not perform the snap through, but vibrates around that curved shape. This leads to an increase of the resonance frequency of the beam and a reduction in the voltage output. The only voltage increase is recorded when a displacement of 0.1 mm is applied to the beam end, this is believed to be due to the fact that the benefit of the axial pre-load is not completely covered by the increase in the stiffness of the beam caused by its

deformation.

Leland and Wright [9] at University of California, Berkeley obtained a reduction in the resonance frequency between 19% and 24% with the introduction of an axial pre-load. The difference between the experiment performed in this work and the one performed at University of California, Berkeley is in the constraint method of the beam. In the experiment performed for this work, at each end, the beam is fixed to a rod fitted with two bearings supported by two columns. The columns at one end of the beam are moved by a linear stage to apply the preload. Whereas, in the experiment performed by Leland and Wright, a self centring vise holds two sliding L-shaped brakets that hold the beam. This design is believed to be able to apply a purely compressive load to the beam without deformations and therefore perform the snap through.

The differences between the finite element model and the experimental results will be discussed in section 6.3.1.

The voltage output from the beam's electromechanical response test was post-processed to calculate the power output (in the same way the voltage output from the harmonic analysis in section 6.1.2 was calculated). The post-process was done considering R_{opt} based on the resonance frequency of the beam at its state and a constant resistance of 5 $k\Omega$. The results are reported in Tables 6.3, 6.4 and 6.5

Table 6.3: Beam without extra mass outputs calculated from the electromechanical response test results

Beam Tip Displacement (mm)	Resonance Frequency (Hz)	Voltage output (V)	R ($k\Omega$)	Current output (μA)	Power output (μW)
	R = R_{opt}				
0	97	0.73	5.0	146	106
0.1	118	0.95	4.1	230	219
0.2	160	0.94	3.0	309	291
0.3	196	0.84	2.5	339	284
0.4	219	0.51	2.2	230	117
	R = constant				
0	97	0.73	5.0	146	106
0.1	118	0.95	5.0	190	181
0.2	160	0.94	5.0	188	177
0.3	196	0.84	5.0	168	141
0.4	219	0.51	5.0	102	320

Table 6.4: Beam with 13 g of extra mass outputs calculated from the electromechanical response test results

Beam Tip Displacement (mm)	Resonance Frequency (Hz)	Voltage output (V)	R ($k\Omega$)	Current output (μA)	Power output (μW)
	R = R_{opt}				
0	44	9.11	11	824	7510
0.1	53	10.12	9.2	1100	11200
0.2	73	3.47	6.7	521	18100
0.3	99	3.33	4.9	687	2260
0.4	114	1.91	4.3	448	855
	R = constant				
0	44	9.11	5.0	1820	16600
0.1	53	10.12	5.0	2020	20500
0.2	73	3.47	5.0	694	2410
0.3	99	3.33	5.0	666	2220
0.4	114	1.91	5.0	382	730

Table 6.5: Beam with 22 g of outputs calculated from the electromechanical response test results

Beam Tip Displacement (mm)	Resonance Frequency (Hz)	Voltage output (V)	R ($k\Omega$)	Current output (μA)	Power output (μW)
	R = R_{opt}				
0	34	11.74	14.3	821	9640
0.1	41	12.53	11.9	1060	13200
0.2	64	9.68	7.6	1270	12300
0.3	81	3.54	6.0	590	2090
0.4	94	3.08	5.1	595	1830
	R = constant				
0	34	11.74	5.0	2350	27600
0.1	41	12.53	5.0	2510	31400
0.2	64	9.68	5.0	1940	18700
0.3	81	3.54	5.0	708	2510
0.4	94	3.08	5.0	616	1900

6.2.3 Snap through experiments

The snap through phenomenon has not been observed for any of the three beams. Even if the beams show a resonance response it never snapped through moving from one of the deformed positions to the symmetric one. The resonance frequencies increase with the application of the pre-load.

The modification of the hinge fitting design did not give the expected results.

The only recorded experience of a snap through has been found in the papers written by the Berkeley research group: it is reported that an acceleration of 39.24 m/s^2 was needed to have the snap through phenomenon [3]. It is believed, after the observation of the behaviour of the beam in several frequency sweep tests with increasing amplitude, pushing to the limits of the available equipment, that a higher acceleration of the shaker could give the right impulse to the snap through phenomenon. It has to be reported that

there are no records available for this set of experiments: the accelerometer allows the recording of accelerations with a maximum value of 19.62 m/s^2 and therefore no sensible data could be recorded.

At the same time, it is observed that the mass fitted in the centre of the beam, even if it has a negligible effect on the stiffness of the beam, has its own response to the vibrational stimulus that alters the response of the whole beam.

It appears clear that the resonance frequency is dependent upon the pre-load introduced in the beam. The application of a tensile pre-load increases the resonance frequency. It is proven that the introduction of a pre-load modifies the resonance frequency of the beam allowing the designers to tune the resonance frequency of the energy harvesting device to the environment.

6.2.4 Testing jig design

The main reason for the unsatisfactory results of the beam electromechanical response test and for the mismatch between the finite element modelling results and the behaviour of the testing beam, is due an incorrect hinge design in the testing Jig. In the only found reference that presents the experimental set up used to perform a snap through test [9], the bimorph beam is described to be 'held between two sliding L-shaped brackets' fitted on a self centring vise. No further information could be found to help the design of the hinges. A first solution was the one presented in section 5.2.1. After performing the beam response test, it was observed that this kind of design does not permit the snap through phenomenon. It is believed that the main reason is the method with which the pre-load is applied: in this configuration the load, generated by the displacement of the columns that hold the beam, is transmitted to the beam in a way that promotes the rotation of the hinged constraint and results in the deformation of the beam. The hinges were then redesigned to be more close to the constraints proposed by Leland and Wright

and the pre-load was tried to be applied in a way that prevents bending in the beam. A schematic comparison between the two design is presented in Figure

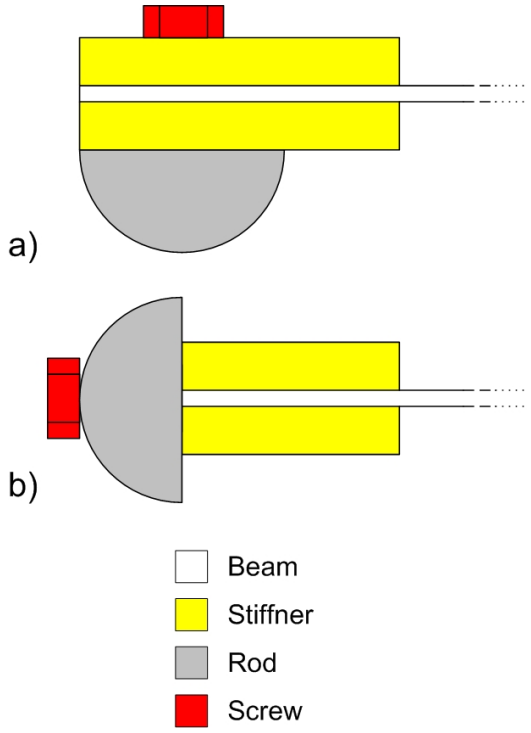

Figure 6.7: Schematic comparison of the hinge design:
a) first attempt
b) modified design

After performing the snap through experiment with negative results, it is believed that a re-design of the constrain configuration is not sufficient, a system able to self align the two ends of the beam is needed.

6.3 Finite elements vs experimental results

Before starting any discussion, it has to be remembered that the aim of the finite element modelling was not to create a model able to accurately predict the mechanical properties and the voltage output of the experimental beam, but to have a tool to understand the general behaviour and the working

principles of the beam.

6.3.1 Beam response

By comparing the results obtained from the finite element model described in section 4.3 and the ones collected during the experiment described in section 5.2.3, it is evident that there is a discrepancy between the two sets of results as shown in Table 6.6.

Table 6.6: First resonance frequency

Added Mass (g)	Resonance Frequency (Hz)		Voltage output (V)	
	FE model	Tested beam	FE model	Tested beam
0	60	97	1.31	0.73
13	27	44	0.94	9.11
22	21	35	0.72	11.55

The difference in the resonance frequency is due to the relative simplicity of the finite element model that does not take into account the damping effect of the glue layers and the energy dissipation of the hinged constraints. This difference was expected from the start of the modelling phase.

A common trend between the finite element model and the real beam can be observed in the behaviour of the resonance frequencies with the increasing of the mass attached to the beam: when adding a mass at the centre of the beam the first resonance frequency is shifted down by an common value, as summarized in table 6.6. The resonance frequency for the beam with 13 grams of extra mass is the 44.2% of the unloaded beam for the finite element model and the 45.4% for the experimental results. For 22 grams of extra mass the percentage are respectively 35.4% and 36.1%.

As expected, there is a difference in the response of the voltage output to the added mass. It has to be remarked the the boundary conditions are different between the finite element model and the experiment. In the harmonic

analysis, the beam tip is allowed a displacement of 4 μm and in the frequency sweep test the vertical displacement of the jig is dependent on the frequency. There is a mismatch in the results obtained from the finite element model and experiments for the behaviour of the power output depending on the added mass. The experimental results are in accordance with expectation of the literature review [20]. The output of the finite element model has already been explained in section 6.1.2. It is believed that a modification in the finite element model that properly simulates the mass with its shape will produce more accurate results.

A substantial difference emerges when analysing the behaviour of the pre-loaded beams, even if a direct comparison can not be done. The axial pre-load lowers the resonance frequency of the finite element model (Figure 4.24)while the application of an axial pre-load increases the resonance frequency of the tested beam (Figures 5.22 and 5.23). An explanation can be found looking at the animation of the modal shapes of the finite element model, and comparing them with the vibration shape of the tested beam. In the finite element model the beam is perfectly compressed and vibrates around the deformed shape given by the compression. When the testing beam is loaded, moving one end towards the other, the beam acquires a bent shape and afterwards, it vibrates around this deformed shape but not snapping to the symmetric deformed shape as observed by the finite element model. The different deformation of the two beams when loaded with a compressive force explains their different modal behaviour. Initially, a different kind of constrain was believed to allow the beam to perform the snap through. After modifying the hinged constraints, as presented in section 6.2.4 and also testing a fixed-fixed constrain configuration the experimental behaviour is still discordant from what is expected from the finite element simulations.

Chapter 7

Conclusions and Suggestions for Further Work

7.1 Conclusions

This section will present the main concepts involved in the design and manufacturing of the bimorph, simply supported bi-stable beam based energy harvesting device and will be concluded with a consideration of the feasibility of the device.

7.1.1 Axial pre-load effect

The application of a compressive axial pre-load to the active material is the main novelty of the present work. The simply supported beam geometry was chosen in order to allow the application of the pre-load. The following conclusions were drawn from the work.

Tunability

The tunability of the bimorph, simply supported bi-stable beam based energy harvesting device was proved with the finite element models. The pre-stressed modal analyses showed that an increase of the axial pre-load reduces the resonance frequency. Furthermore, it is possible to tune the energy harvesting device to different environmental vibrations by applying different pre-loads. The results obtained from the finite element simulations could not be validated by the experimental work, this was due to the difficulty encountered while applying a purely axial pre-load to the beam. Whereas, the results obtained by Leland and Wright [9] are in good agreement with the finite element modeling results.

Power output

The increasing of the power output could not be proven with the finite element model because it was not possible to develop the code for the pre-stressed harmonic analysis that updates the coordinates between the static and the harmonic analysis. Also, the differences in the boundary conditions between the harmonic analysis and non linear static analysis further amplified the problem. On the other hand, the experimental results only showed a

marginal increase in the device power output. This is due to the deformation of the beam owing to the inadequate hinge design and therefore to the fact that the pre-load could not be axially applied.

7.1.2 Shape optimisation

The finite element analysis of various shapes of the beam footprint showed that a shape optimisation can increase the power output by 40%. The ideal shape has a ratio of beam centre to beam tip width between 3 (10-30 mm footprint) and 1.86 (14-26 mm footprint).

7.1.3 Testing jig

The testing jig, and consequently the device itself, has been proven to be complex to be made. An inadequate hinge design gave rise to issues with the application of the pre-load. When pre-loaded, the beam assumes a bent shape and therefore, it is not perfectly axially loaded. This changed the harmonic behaviour of the beam and made the snap through phenomenon, base concept of the bimorph of the simply supported bi-stable beam based energy harvesting device, impossible to be obtained. This has to be taken into account in any future industrialisation of this concept.

7.1.4 Feasibility

Considering the obtained results the possibility to develop a bimorph, simply supported bi-stable beam based energy harvesting device looks promising. From the finite element results the possibility to tune the device to different resonance frequencies has been proved. The pre-stress used to tune the device also has a benefit on the energy output, as observed in the experiments and found in literature. A problem has been identified, during this work, as the main weakness of the concept presented here and that made its realisation delicate and complex: the application of the pre-load. If a proper method to apply a purely axial pre-load to the beam is identified, then the bimorph, simply supported bi-stable beam based energy harvesting device

will represent a profitable way to harvest energy from the environment and transform it into usable electric power.

7.2 Suggestions for further work

7.2.1 Finite element modelling

To perform an in-depth study of the bimorph, simply supported bi-stable beam based energy harvesting device, a code which is able to perform a pre-stressed harmonic analysis is needed. This will give the designers the possibility to really understand the benefit of the pre-load on the voltage output of the device and at the same time to understand if a shape optimisation of the beam can make this kind of devices a profitable energy source.

The finite element model can be also used to evaluate a law that correlates the pre-load intensity and the resonance frequency drop.

7.2.2 Experimental work

The main problem is to create a system able to apply the axial pre-load without bending the beam; this will allow testing the real benefits of the action of the pre-load on the beam voltage output. A self aligning system is needed to precisely align the two ends of the beam and keep them aligned during the application of the pre-load preventing the beam from bending.

At the same time, to address the problem of the pre-load application, different kinds of beams can be designed and tested: a bimorph beam with a thick soft substrate might also be able bear the pre-load without bending and to perform the snap through.

Regarding the hinge design a new configuration should be studied. The problem while addressing this issue, if the two ends of the beam are perfectly

aligned and the pre-load applied without bending the beam, is the energy dissipation. The energy absorbed by the hinges should be minimized in order to keep the acceleration needed to preform the snap through as low as possible.

Bibliography

[1] J. Ajitsaria, S. Y. Choe, D. Shen, and D. J. Kim. Modeling and analysis of a bimorph piezoelectric cantilever beam for voltage generation. *Smart Materials and Structures*, 16(2):447–454, 2007.

[2] S. R. Anton and H. A. Sodano. A review of power harvesting using piezoelectric materials (20032006). *Smart Materials and Structures*, (16):R1 – R21, 2007.

[3] J. Baker, S. Roundy, and P. K. Wright. Alternative geometries for increasing power density in vibration energy scavenging for wireless sensor networks. In *The Third International Energy Conversion Engineering Conference, American Institute of Aeronautics and Astronautics*, pages Paper Number AIAA 2005–5617, 15 18 August 2005.

[4] S. P. Beeby, M. J. Tudor, and N. M. White. Energy harvesting vibration sources for microsystems applications. *Measurement Science and Technology*, 17:R175, December 2006.

[5] en.wikipedia.org. Buckling - from wikipedia, the free encyclopedia, 2009.

[6] M. Ericka, D. Vasic, F. Costa, and G. Poulain. Predictive energy harvesting from mechanical vibration using a circular piezoelectric membrane, 2005. ID: 1.

[7] S. Imaoka. Ansys tip of the week: Conversion of piezoelectric material data, 1999.

[8] H. Kim, S. Priya, and K. Uchino. Modeling of piezoelectric energy harvesting using cymbal transducers. *Japanese Journal of Applied Physics*, 45(7):5836, 2006.

[9] E. S. Leland and P. K. Wright. Resonance tuning of piezoelectric vibration energy scavenging generators using compressive axial preload. *Smart Materials and Structures*, 15(5):1413–1420(8), October 2006.

[10] G. A. Lesieutre and C. L. Davis. Can a cuoppling coefficient of a piezoelectric device be higher than those of its active material? *Journal of Intelligent Material Systems and Structures*, 8:859–867, 1997.

[11] L. Mateu. Optimum piezoelectric bending beam structures for energy harvesting using shoe inserts. *Journal of Intelligent Material Systems and Structures*, 16(10):835 – 845, 2005.

[12] L. Mateu and F. Moll Echeto. Review of energy harvesting techniques and applications for microelectronics, 2005.

[13] E. Minazara, D. Vasic, F. Costa, and G. Poulin. Piezoelectric diaphragm for vibration energy harvesting. *Ultrasonics,*, 44(Supplement 1):e699–e703, 12/22 2006.

[14] K. Mossi, C. Green, Z. Ounaies, and E. Hughes. Harvesting energy using a thin unimorph prestressed bender: Geometrical effects. *Journal of Intelligent Material Systems and Structures*, 16(3):249 – 261, 2005.

[15] P. Museros and M. D. Martinez-Rodrigo. Vibration control of simply supported beams under moving loads using fluid viscous dampers. *Journal of Sound and Vibration*, 300(1-2):292–315, 2/20 2007.

[16] T. H. Ng and W. H. Liao. Feasibility study of a self-powered piezoelectric sensor. volume 5389, pages 377 – 388, July 29, 2004 2004.

[17] T. H. Ng and W. H. Liao. Sensitivity analysis and energy harvesting for a self-powered piezoelectric sensor. *Journal of Intelligent Material Systems and Structures*, 16(10):785 – 797, 2005.

[18] M. Pereyma. Overview of the modern state of the vibration energy harvesting devices. pages 107 – 112, 23-26 May 2007.

[19] S. Roundy, E. S. Leland, J. Baker, E. Carleton, E. Reilly, E. Lai, B. Otis, J. M. Rabaey, P. K. Wright, and V. Sundararajan. Improving power output for vibration-based energy scavengers, 2005. ID: 1.

[20] S. Roundy and P. K. Wright. A piezoelectric vibration based generator for wireless electronics. *Smart Materials and Structures,*, 13(5):1131–1142(12), October 2004.

[21] S. Roundy, P. K. Wright, and J. Rabaey. A study of low level vibrations as a power source for wireless sensor nodes. *Computer Communications,*, 26(11):1131–1144, 7/1 2003.

[22] H. A. Sodano and D. J. Inman. Comparison of piezoelectric energy harvesting devices for recharging batteries. *Journal of Intelligent Material Systems and Structures,*, 16(10):799 – 807, 2005.

[23] H. A. Sodano, D. J. Inman, and G. Park. A review of power harvesting from vibration using piezoelectric materials. *The Shock and Vibration Digest*, 36(3):197 – 205, 2004.

[24] S. Wing. Overview of smart materials technology.

[25] E. Worthington and M. Zhu. An experimental study on the electric output performance of a piezoelectric energy harvesting device directly connected to a resistive load. *IEEE Transactions on Ultrasonics Ferroelectrics and Frequency Control*, Awating for publication.

[26] M. Zhu and G. Leighton. Dimensional reduction study of piezoelectric ceramics constitutive equations from 3d to 2d and 1d. *IEEE Transactions on Ultrasonics Ferroelectrics and Frequency Control*, 47:2377–2383, 2008.

[27] M. Zhu and E. Worthington. design and testing of piezoelectric energy harvesting devices for generation of higher electric power for wireless sensor networks. 25-28 Oct., 2009 Awaiting for publication.

[28] M. Zhu, E. Worthington, and J. Njuguna. Analyses of power output of piezoelectric energy harvesting devices directly connected to a resistive load using a coupled piezoelectric-circuit finite element method. *IEEE Transactions on Ultrasonics Ferroelectrics and Frequency Control*, 56(7):1309–1318, 2009.

[29] M. Zhu, E. Worthington, and J. Njuguna. Coupled piezoelectric-circuit fea to study influence of a resistive load on power output of piezoelectric energy devices. volume 7362, pages 736202:1–12, 4-6 May 2009.

Appendices

Appendix A

ANSYS models

A.1 BEAM3 model

```
FINISH
/CLEAR
/CWD,C:\1-Model\Beam
/FILNAME,Beam-Buckling
/TITLE,Beam-Buckling
/PREP7
/OUTPUT, TERM
/UNITS, SI
/SHOW

! ***********
! Basic Unit
! ***********

mm=1e-3
PI2=2*3.14159

! ****************************************
! Define geometrical  structural parameters
! ****************************************

length = 100*mm ! beam length
width = 20*mm ! beam width
thickness = 0.375*mm ! beam thickness
```

```
meshsize = 2*mm

! ***************************
! Define material parameters
! ***************************

dens = 7867 ! Density in kg/m^3
young = 1.06e11 ! Young's modulus in Pa
poiss = 0.3 ! Poisson ratio

! **********************
! Material declaration
! **********************

MP, EX, 1, young
MP, DENS, 1, dens
MP, NUXY, 1, poiss

! ******************
! Element type used
! ******************

ET,1,BEAM3  ! Set element type
R,1,Width*thickness,Width*(thickness**3)/12,thickness  !** = exponent

! *********
! Modeling
! *********

! GEOMETRY
K,1,0,0,0,   ! Keypoint, 1, x, y, z
K,2,length,0,0,! Keypoint, 2, x, y, z
L,1,2   ! Line from keypoint 1 to 2

! MASHING
LESIZE,ALL,meshsize ! Size of line elements
LMESH,1  ! Mesh line 1
```

A.2 SHELL93 model

```
FINISH
/CLEAR
/CWD,C:\1-Model\Shell
/FILNAME,Shell
/TITLE,Shell
/PREP7
/OUTPUT, TERM
/UNITS, SI
/SHOW

! ***********
! Basic Unit
! ***********

mm = 1e-3
um = 1e-6
eps_0 = 8.854e-12
PI2 = 2*3.14159
res_fre = 51 !Hz

! ****************************************
! Define geometrical  structural parameters
! ****************************************

! Beam Geometry

base_w = 20*mm ! beam base width
center_w = 20*mm ! beam center width
length = 100*mm ! beam length
thick = 0.375*mm ! pzt thickness

! Mesh parameters

meshsize = 2*mm

! Loads

BuckLoad = XX
DestLoad = BuckLoad/100
```

```
! Numbers...

Nnodes = (base_w/meshsize)+(base_w/meshsize)+1

! ***************************
! Define material parameters
! ***************************

dens = 7867 ! Density in kg/m^3
young = 1.06e11 ! Young's modulus in Pa
poiss = 0.3 ! Poisson ratio

! ******************
! Element type used
! ******************

ET, 1, SHELL93
R,thick,thick,thick,thick

! **********************
! Material declaration
! **********************

MP, EX,   1, young
MP, DENS, 1, dens
MP, NUXY, 1, poiss

! *********
! Modeling
! *********

! * Draw 2D

k,1,-length/2,-base_w/2,0
k,2,-length/2,base_w/2,0
k,3,0,center_w/2,0
k,4,length/2,base_w/2,0
k,5,length/2,-base_w/2,0
k,6,0,-center_w/2,0
```

```
A,1,2,3,4,5,6

! * Mesh 2D

TYPE,1
ESIZE, meshsize
AMESH, all

NSEL,S,LOC, x, -meshsize/4, meshsize/4
NSEL,R,LOC, Y, -meshsize/4, meshsize/4
*GET,node_cr,node,,num,min
```

A.3 SHELL91 model

```
FINISH
/CLEAR
/CWD,C:\1-Model\Shell91
/FILNAME,Shell91-Harmonic
/TITLE,Shell91-Harmonic
/PREP7
/OUTPUT, TERM
/UNITS, SI
/SHOW

! ***********
! Basic Unit
! ***********

mm = 1e-3
um = 1e-6
eps_0 = 8.854e-12
PI2 = 2*3.14159
res_fre = 51 !Hz

! ****************************************
! Define geometrical  structural parameters
! ****************************************
```

```
! Beam Geometry

base_w = 20*mm ! beam base width
center_w = 20*mm ! beam center width
length = 100*mm ! beam length
thick = 0.125*mm ! pzt thickness

! Mesh parameters

meshsize = 2*mm

! Loads

BuckLoad = XX
DestLoad = BuckLoad/100
Q=32
KECI=1/(2*Q)

! Numbers...

Nnodes = ((base_w/meshsize)*2)+1

! ***************************
! Define material parameters
! ***************************

dens_ss = 8000 ! Density in kg/m^3
young_ss = 19.3e10 ! Young's modulus in Pa
poiss_ss = 0.3 ! Poisson ratio

dens_pzt = 7800 ! Density in kg/m^3
young_pzt = 6.2e10 ! Young's modulus in Pa
poiss_pzt = 0.3 ! Poisson ratio

! *********************
! Material declaration
! *********************

MP, EX,   1, young_ss
MP, DENS, 1, dens_ss
MP, NUXY, 1, poiss_ss
```

```
MP, EX,   2, young_pzt
MP, DENS, 2, dens_pzt
MP, NUXY, 2, poiss_pzt

! ******************
! Element type used
! ******************

ET, 1, SHELL91,3
R,1,3
RMORE
RMORE,2,0,thick,thick,thick,thick
RMORE,1,0,thick,thick,thick,thick
RMORE,2,0,thick,thick,thick,thick

! *********
! Modeling
! *********

! * Draw 2D

k,1,-length/2,-base_w/2,0
k,2,-length/2,base_w/2,0
k,3,0,center_w/2,0
k,4,length/2,base_w/2,0
k,5,length/2,-base_w/2,0
k,6,0,-center_w/2,0

A,1,2,3,4,5,6

! * Mesh 2D

TYPE,1
ESIZE, meshsize
AMESH, all

NSEL,S,LOC, x, -meshsize/4, meshsize/4
NSEL,R,LOC, Y, -meshsize/4, meshsize/4
*GET,node_cr,node,,num,min
```

A.4 SOLID45 model

```
FINISH
/CLEAR
/CWD,C:\1-Model\solid
/FILNAME,Solid
/TITLE, SSBB-Solid
/PREP7
/OUTPUT, TERM
/UNITS, SI
/SHOW

! ***********
! Basic Unit
! ***********

mm = 1e-3
um = 1e-6
eps_0 = 8.854e-12
PI2 = 2*3.14159
res_fre = 51 !Hz

! ****************************************
! Define geometrical  structural parameters
! ****************************************

! Beam Geometry

base_w = 20*mm ! beam base width
center_w = 20*mm ! beam center width
length = 100*mm ! beam length
thick = 0.375*mm ! pzt thickness

! Mesh parameters

meshsize = 2*mm

! Loads

BuckLoad = XX
DestLoad = BuckLoad/100
```

```
! Numbers...

Nnodes = (base_w/meshsize)+1

! ***************************
! Define material parameters
! ***************************

dens = 7867 ! Density in kg/m^3
young = 1.06e11 ! Young's modulus in Pa
poiss = 0.3 ! Poisson ratio

! ******************
! Element type used
! ******************

ET, 1, PLANE42
ET, 2, SOLID45

! **********************
! Material declaration
! **********************

MP, EX,   1, young
MP, DENS, 1, dens
MP, NUXY, 1, poiss

! *********
! Modeling
! *********

! * Draw 2D

k,1,-length/2,-base_w/2,0
k,2,-length/2,base_w/2,0
k,3,0,center_w/2,0
k,4,length/2,base_w/2,0
k,5,length/2,-base_w/2,0
k,6,0,-center_w/2,0
```

```
A,1,2,3,4,5,6

! * Mesh 2D

TYPE,1
ESIZE, meshsize
MSHAPE, 0, 2D ! 0 for square elements
! 1 for triangular elements
AMESH, all

! * Extrude 3D

! Substrate layer

TYPE,2
MAT,1
ESIZE, , 2
ASEL, , LOC, Z, 0
VEXT, ALL, , , , ,thick

ESEL, U,TYPE, ,1 ! Unselect PLANE42 elements

NSEL, ,LOC, x, -meshsize/2, meshsize/2
NSEL,R,LOC, Y, -meshsize/2, meshsize/2
NSEL,R,LOC, Z, 0
*GET,node_cr,node,,num,min
```

A.5 Layered SOLID45 and SOLID5 model

```
FINISH
/CLEAR
/CWD,C:\1-Model\ss\20
/FILNAME,20-Harmonic
/TITLE, SSBB-20-Harmonic
/PREP7
/OUTPUT, TERM
/UNITS, SI
/SHOW
```

```
! ***********
! Basic Unit
! ***********

mm = 1e-3
um = 1e-6

! ****************************************
! Define geometrical  structural parameters
! ****************************************

! Beam Geometry

base_w = 20*mm ! beam base width
center_w = 20*mm ! beam center width
length = 100*mm ! beam length
pzt_t = 0.125*mm ! pzt thickness
sub_t = 0.125*mm ! substrate thickness

! Mesh parameters

meshsize= 2*mm
sub_m = 2 ! substrate thickness mesh division number
pzt_m = 2 ! piezo thickness mesh division number

! Loads

BuckLoad = XX
DestLoad = BuckLoad/100

! Numbers...

Nnodes = (base_w/meshsize)+1

! **************************
! Define material parameters
! **************************

! * PZT  (p=PZT)
```

```
dens_p=7800 ! Density in kg/m^3

s11_p = 15.1e-12 ! s11_p in m^2/N
s12_p = -4.5e-12 ! s12_p in m^2/N
s13_p = -9.4e-12  ! s13_p in m^2/N
s33_p = 24.8e-12 ! s33_p in m^2/N
s66_p = 39.2e-12 ! s44_p in m^2/N
s44_p = 37.1e-12 ! s44_p in m^2/N

c11_p = 16.9e10 ! c11_p in N/m^2
c12_p = 11.8e10 ! c12_p in N/m^2
c13_p = 10.9e10 ! c13_p in N/m^2
c33_p = 12.3e10 ! c33_p in N/m^2
c44_p = 2.7e10 ! c44_p in N/m^2
c66_p = 2.5e10 ! c66_p in N/m^2

! * AISI 316 (ss=AISI 316)

dens_ss = 8000 ! Density in kg/m^3
young_ss = 193e9 ! Young's modulus in Pa
poiss_ss = 0.3 ! Poisson ratio

! ******************
! Element type used
! ******************

ET, 1, PLANE42
ET, 2, SOLID45 ! for mechanical ONLY
ET, 3, SOLID5,2 ! for piezoelectric ONLY, 2 => purely mechanical

! *************************
! material reference number
! *************************

! material 1 = Substrate
! material 2 = Piezoelectric

! *********************
! Material declaration
! *********************
```

```
! *** Substrate material ***

MP, EX,   1, young_ss
MP, DENS, 1, dens_ss
MP, NUXY, 1, poiss_ss

! *** PZT Material ***

! Density

MP, DENS, 2, dens_p

! Stiffness Matrix

!TB, ANEL,2,1,,1
!TBDATA, 1 , s11_p,s12_p,s13_p
!TBDATA, 7 , s11_p,s13_p
!TBDATA, 12, s33_p
!TBDATA, 16, s66_p
!TBDATA, 19, s44_p
!TBDATA, 21, s44_p

TB, ANEL,2,1,,0
TBDATA, 1,  c11_p
TBDATA, 2,  c12_p
TBDATA, 3,  c13_p
TBDATA, 7,  c11_p ! c22=c11
TBDATA, 8,  c13_p ! c23=c13
TBDATA, 12, c33_p
TBDATA, 16, c66_p ! C66 goes in 44 position
TBDATA, 19, c44_p
TBDATA, 21, c44_p ! c55=c44

! *********
! Modeling
! *********

! * Draw 2D

k,1,-length/2,-base_w/2,0
k,2,-length/2,base_w/2,0
```

```
k,3,0,center_w/2,0
k,4,length/2,base_w/2,0
k,5,length/2,-base_w/2,0
k,6,0,-center_w/2,0

A,1,2,3,4,5,6

! * Mesh 2D

TYPE,1
ESIZE, meshsize
MSHAPE, 0, 2D
AMESH, all

! * Extrude 3D below

! Substrate layer

TYPE,2
MAT,1
ESIZE, , sub_m/2
ASEL, , LOC, Z, 0
VEXT, ALL, , , , ,sub_t/2
ASEL, , LOC, Z, 0
VEXT, ALL, , , , ,-sub_t/2
/VIEW, 1, 1, 1, 1
/VUP, 1, Z
/ANG
/REP

! PZT layer

TYPE,3
MAT,2
ESIZE, , pzt_m
ASEL, , LOC, Z, sub_t/2
VEXT, ALL, , , , , pzt_t

ASEL, , LOC, Z, -sub_t/2
VEXT, ALL, , , , , -pzt_t
```

```
NUMMRG, NODE, 1.0E-10

NSEL, ,LOC, x, -meshsize/2, meshsize/2
NSEL,R,LOC, Y, -meshsize/2, meshsize/2
NSEL,R,LOC, Z, 0
*GET,node_cr,node,,num,min

*GET,ENUM,ELEM,,NUM,MAX
```

A.6 Testing beam model

```
! ****************************
! Simply Supported Bimorph Beam
! ****************************

FINISH
/CLEAR
/CWD,C:\1-Model\Experiment
/FILNAME,Experiment-Harmonic
/TITLE,Experiment-Harmonic
/PREP7
/OUTPUT, TERM
/UNITS, SI
/SHOW

! ***********
! Basic Unit
! ***********

mm = 1e-3
um = 1e-6
eps_0 = 8.854e-12
PI2 = 2*3.14159

! ****************************************
! Define geometrical  structural parameters
! ****************************************
```

```
! Beam Geometry

base_w = 20*mm ! beam base width
length = 112*mm ! beam length
pzt_t = 0.125*mm ! pzt thickness
sub_t = 0.125*mm ! substrate thickness
stif_t = 4*mm
stif_l = 26*mm

! Mesh parameters

meshsize = 2*mm
sub_m = 2 ! substrate thickness mesh division number
pzt_m = 2 ! piezo thickness mesh division number
stif_m = 64 ! stiffner thickness mesh division number

! Loads

BuckLoad = XX
DestLoad = BuckLoad/100
Mass = XX

! Numbers...

Nnodes = (base_w/meshsize)+1

! ***************************
! Define material parameters
! ***************************

! * PZT  (p=PZT)

dens_p=7800 ! Density in kg/m^3

s11_p = 15.1e-12 ! s11_p in m^2/N
s12_p = -4.5e-12 ! s12_p in m^2/N
s13_p = -9.4e-12  ! s13_p in m^2/N
s33_p = 24.8e-12 ! s33_p in m^2/N
s66_p = 39.2e-12 ! s44_p in m^2/N
s44_p = 37.1e-12 ! s44_p in m^2/N
```

```
c11_p = 16.9e10 ! c11_p in N/m^2
c12_p = 11.8e10 ! c12_p in N/m^2
c13_p = 10.9e10 ! c13_p in N/m^2
c33_p = 12.3e10 ! c33_p in N/m^2
c44_p = 2.7e10 ! c44_p in N/m^2
c66_p = 2.5e10 ! c66_p in N/m^2

e31_p = -12 !
e33_p = 18.2 !
e15_p = 21.9 !

eps11_p = 3550 ! In F/m^2
eps33_p = 3850 ! In F/m^2

! * AISI 316 (ss=AISI 316)

dens_ss = 8000 ! Density in kg/m^3
young_ss = 193e9 ! Young's modulus in Pa
poiss_ss = 0.3 ! Poisson ratio

! * TUFNOL (tf=TUFNOL)

dens_tf = 1500 ! Density in kg/m^3
young_tf = 100e9 ! Young's modulus in Pa
poiss_tf = 0.3 ! Poisson ratio

! ******************
! Element type used
! ******************

ET, 1, PLANE42
ET, 2, SOLID45 ! for mechanical ONLY
ET, 3, SOLID5,3 ! for piezoelectric ONLY
! 2 => only U
! 3 => U and VOLT
ET, 4, MASS21,,,2
R,1,Mass

! *************************
! material reference number
! *************************
```

```
! material 1 = Substrate  ! (Change ss or pi to change the substrate)
! material 2 = Piezoelectric

! *********************
! Material declaration
! *********************

! *** Substrate material ***

MP, EX,   1, young_ss
MP, DENS, 1, dens_ss
MP, NUXY, 1, poiss_ss

! *** Stiffner material ***

MP, EX,   3, young_tf
MP, DENS, 3, dens_tf
MP, NUXY, 3, poiss_tf

! *** PZT Material ***

! Density

MP, DENS, 2, dens_p

! Stiffness Matrix

!TB, ANEL,2,1,,1
!TBDATA, 1 , s11_p,s12_p,s13_p
!TBDATA, 7 , s11_p,s13_p
!TBDATA, 12, s33_p
!TBDATA, 16, s66_p
!TBDATA, 19, s44_p
!TBDATA, 21, s44_p

TB, ANEL,2,1,,0
TBDATA, 1,  c11_p
TBDATA, 2,  c12_p
TBDATA, 3,  c13_p
TBDATA, 7,  c11_p ! c22=c11
```

```
TBDATA, 8,  c13_p ! c23=c13
TBDATA, 12, c33_p
TBDATA, 16, c66_p ! C66 goes in 44 position
TBDATA, 19, c44_p
TBDATA, 21, c44_p ! c55=c44

! Piezoelectric Constant Matrix

TB, PIEZ, 2,
TBDATA, 3 , e31_p
TBDATA, 6 , e31_p
TBDATA, 9 , e33_p
TBDATA, 14, e15_p
TBDATA, 16, e15_p

! Permittivity Matrix

EMUNIT,EPZRO,eps_0
MP, PERX, 2, eps11_p
MP, PERY, 2, eps11_p
MP, PERZ, 2, eps33_p

! *********
! Modeling
! *********

! * Draw 2D

k,1,-length/2,base_w/2,0
k,2,-length/2+stif_l,base_w/2,0
k,3,length/2-stif_l,base_w/2,0
k,4,length/2,base_w/2,0
k,5,-length/2,-base_w/2,0
k,6,-length/2+stif_l,-base_w/2,0
k,7,length/2-stif_l,-base_w/2,0
k,8,length/2,-base_w/2,0
k,9,0,0,0

A,1,2,6,5
A,2,3,7,6
A,3,4,8,7
```

```
NUMMRG,KP,1.0E-10

! * Mesh 2D

TYPE,1
ESIZE, meshsize
MSHAPE, 0, 2D ! 0 for square elements
! 1 for triangular elements
AMESH, all

! * Extrude 3D below

! Substrate layer

TYPE,2
MAT,1
ESIZE, , sub_m/2
ASEL, , LOC, Z, 0
VEXT, ALL, , , , ,sub_t/2
ASEL, , LOC, Z, 0
VEXT, ALL, , , , ,-sub_t/2
/VIEW, 1, 1, 1, 1
/VUP, 1, Z
/ANG
/REP

NUMMRG,KP,1.0E-10
NUMMRG,NODE,1.0E-10

ESEL, U,TYPE, ,1 ! Unselect PLANE42 elements

! PZT layer

TYPE,3
MAT,2
ESIZE, , pzt_m

ASEL,S, LOC, Z, sub_t/2
ASEL,R, LOC, X, 0
VEXT, ALL, , , , , pzt_t
```

```
ASEL, , LOC, Z, -sub_t/2
ASEL,R, LOC, X, 0
VEXT, ALL, , , , , -pzt_t

NUMMRG,KP,1.0E-10
NUMMRG,NODE,1.0E-10

! Stiffner

TYPE,2
MAT,3
ESIZE, , stif_m

ASEL,S, LOC, Z, sub_t/2
ASEL,R, LOC, X, -length/2,-length/2+stif_l
VEXT, ALL, , , , , stif_t

ASEL,S, LOC, Z, sub_t/2
ASEL,R, LOC, X, length/2,length/2-stif_l
VEXT, ALL, , , , , stif_t

! Mass

TYPE,4
KMESH,9

NUMMRG,KP,1.0E-10
NUMMRG,NODE,1.0E-10

NSEL, ,LOC,x,-meshsize/2,meshsize/2
NSEL,R,LOC,Y,-meshsize/2,meshsize/2
NSEL,R,LOC,Z,0
*GET,node_cr,node,,num,min

*GET,ENUM,ELEM,,NUM,MAX

! *********************************************************
!     Define the coupling sets of the electrode
! The PZT are connected in parallel & with same polaities
! *********************************************************
```

```
! Define the first couple set of the central electrodes

NSEL,S,LOC,Z,sub_t/2 ,,0.1*um
NSEL,A,LOC,Z,-sub_t/2,,0.1*um
NSEL,R,Loc,X,-length/2+stif_l,length/2-stif_l,0.1*um
*GET,node_gr,node,,num,min
CM,ground1,node
CP,next,volt,all
D,node_gr,volt,0

NSEL,all ! Reselect all the node

! Define the second couple set of the external electrodes, charge (voltage) as o

NSEL,S,LOC,Z,sub_t/2+pzt_t ,,0.1*um
NSEL,A,LOC,Z,-sub_t/2-pzt_t,,0.1*um
NSEL,R,Loc,X,-length/2+stif_l,length/2-stif_l,0.1*um
*GET,node_si,node,,num,min
CM,signal1,node
CP,next,volt,all

NSEL,all ! Reselect all the nodes
```

A.7 Beam footprint optimization model

```
! ******************************
! Simply Supported Bimorph Beam
! ******************************

FINISH
/CLEAR
/CWD,C:\1-Model\ss\20
/FILNAME,20-Harmonic
/TITLE, SSBB-20-Harmonic
/PREP7
/OUTPUT, TERM
```

```
/UNITS, SI
/SHOW

! ***********
! Basic Unit
! ***********

mm = 1e-3
um = 1e-6
eps_0 = 8.854e-12
PI2 = 2*3.14159

! ****************************************
! Define geometrical  structural parameters
! ****************************************

! Beam Geometry

base_w = XX*mm ! beam base width
center_w = XX*mm ! beam center width
mid_w =  (base_w+center_w)/2
length = 100*mm ! beam length
pzt_t = 0.125*mm ! pzt thickness
sub_t = 0.125*mm ! substrate thickness

! Mesh parameters

meshsize = 4*mm
sub_m = 2 ! substrate thickness mesh division number
pzt_m = 2 ! piezo thickness mesh division number

! Loads

BuckLoad = -XX
DestLoad = BuckLoad/100

! Numbers...

Nnodes = (base_w/meshsize)+1

! ***************************
```

```
! Define material parameters
! ***************************

! * PZT  (p=PZT)

dens_p=7800 ! Density in kg/m^3

s11_p = 15.1e-12 ! s11_p in m^2/N
s12_p = -4.5e-12 ! s12_p in m^2/N
s13_p = -9.4e-12  ! s13_p in m^2/N
s33_p = 24.8e-12 ! s33_p in m^2/N
s66_p = 39.2e-12 ! s44_p in m^2/N
s44_p = 37.1e-12 ! s44_p in m^2/N

c11_p = 16.9e10 ! c11_p in N/m^2
c12_p = 11.8e10 ! c12_p in N/m^2
c13_p = 10.9e10 ! c13_p in N/m^2
c33_p = 12.3e10 ! c33_p in N/m^2
c44_p = 2.7e10 ! c44_p in N/m^2
c66_p = 2.5e10 ! c66_p in N/m^2

e31_p = -12 !
e33_p = 18.2 !
e15_p = 21.9 !

eps11_p = 3550 ! In F/m^2
eps33_p = 3850 ! In F/m^2

! * AISI 316 (ss=AISI 316)

dens_ss = 8000 ! Density in kg/m^3
young_ss = 193e9 ! Young's modulus in Pa
poiss_ss = 0.3 ! Poisson ratio

! * POLYIMIDE (pi=Polyimide)

dens_pi = 1400 ! Density in kg/m^3
young_pi = 2.5e9 ! Young's modulus in Pa
poiss_pi = 0.34 ! Poisson ratio

! ******************
```

```
! Element type used
! ******************

ET, 1, PLANE42
ET, 2, SOLID45 ! for mechanical ONLY
ET, 3, SOLID5,3 ! for piezoelectric ONLY
! 2 => only U
! 3 => U and VOLT

! ************************
! material reference number
! ************************

! material 1 = Substrate  ! (Change ss or pi to change the substrate)
! material 2 = Piezoelectric

! *********************
! Material declaration
! *********************

! *** Substrate material *** ! (Change ss or pi to change the substrate)

MP, EX,   1, young_ss
MP, DENS, 1, dens_ss
MP, NUXY, 1, poiss_ss

! *** PZT Material ***

! Density

MP, DENS, 2, dens_p

! Stiffness Matrix

!TB, ANEL,2,1,,1
!TBDATA, 1 , s11_p,s12_p,s13_p
!TBDATA, 7 , s11_p,s13_p
!TBDATA, 12, s33_p
!TBDATA, 16, s66_p
!TBDATA, 19, s44_p
!TBDATA, 21, s44_p
```

```
TB, ANEL,2,1,,0
TBDATA, 1,  c11_p
TBDATA, 2,  c12_p
TBDATA, 3,  c13_p
TBDATA, 7,  c11_p ! c22=c11
TBDATA, 8,  c13_p ! c23=c13
TBDATA, 12, c33_p
TBDATA, 16, c66_p ! C66 goes in 44 position
TBDATA, 19, c44_p
TBDATA, 21, c44_p ! c55=c44

! Piezoelectric Constant Matrix

TB, PIEZ, 2,
TBDATA, 3 , e31_p
TBDATA, 6 , e31_p
TBDATA, 9 , e33_p
TBDATA, 14, e15_p
TBDATA, 16, e15_p

! Permittivity Matrix

EMUNIT,EPZRO,eps_0
MP, PERX, 2, eps11_p
MP, PERY, 2, eps11_p
MP, PERZ, 2, eps33_p

! *********
! Modeling
! *********

! * Draw 2D

k,1,-length/2,-base_w/2,0
k,2,-length/2,base_w/2,0
k,3,0,center_w/2,0
k,4,length/2,base_w/2,0
k,5,length/2,-base_w/2,0
k,6,0,-center_w/2,0
```

```
A,1,2,3,4,5,6

! * Mesh 2D

TYPE,1
ESIZE, meshsize
MSHAPE, 0, 2D ! 0 for square elements
! 1 for triangular elements
AMESH, all

! * Extrude 3D below

! Substrate layer

TYPE,2
MAT,1
ESIZE, , sub_m/2
ASEL, , LOC, Z, 0
VEXT, ALL, , , , ,sub_t/2
ASEL, , LOC, Z, 0
VEXT, ALL, , , , ,-sub_t/2
/VIEW, 1, 1, 1, 1
/VUP, 1, Z
/ANG
/REP

! PZT layer

TYPE,3
MAT,2
ESIZE, , pzt_m
ASEL, , LOC, Z, sub_t/2
VEXT, ALL, , , , , pzt_t

ASEL, , LOC, Z, -sub_t/2
VEXT, ALL, , , , , -pzt_t

NUMMRG, NODE, 1.0E-10

NSEL, ,LOC, x, -meshsize/2, meshsize/2
NSEL,R,LOC, Y, -meshsize/2, meshsize/2
```

```
NSEL,R,LOC, Z, 0
*GET,node_cr,node,,num,min

*GET,ENUM,ELEM,,NUM,MAX

! *********************************************************
!     Define the coupling sets of the electrode
! The PZT are connected in parallel & with same polaities
! *********************************************************

! Define the first couple set of the central electrodes

NSEL,S,LOC,Z,sub_t/2 ,,0.1*um
NSEL,A,LOC,Z,-sub_t/2,,0.1*um
NSEL,R,Loc,X,-length/2,length/2,0.1*um
*GET,node_gr,node,,num,min
CM,ground1,node
CP,next,volt,all
D,node_gr,volt,0

NSEL,all ! Reselect all the node

! Define the second couple set of the external electrodes, charge (voltage) as o

NSEL,S,LOC,Z,sub_t/2+pzt_t ,,0.1*um
NSEL,A,LOC,Z,-sub_t/2-pzt_t,,0.1*um
NSEL,R,Loc,X,-length/2,length/2,0.1*um
*GET,node_si,node,,num,min
CM,signal1,node
CP,next,volt,all

NSEL,all ! Reselect all the nodes
```

Appendix B

Jig Drawings

This section reports the technical drawings realized with I-DEAS 11 for the fabrication of the testing jig.

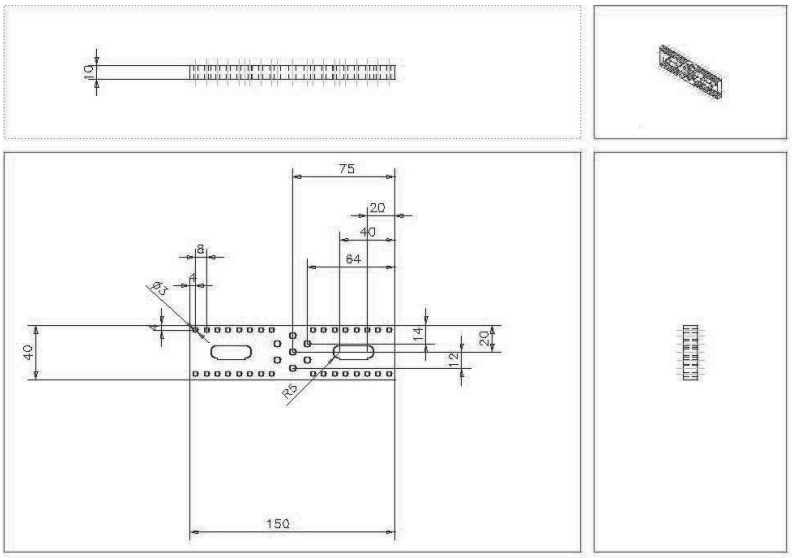

Figure B.1: Connection plate

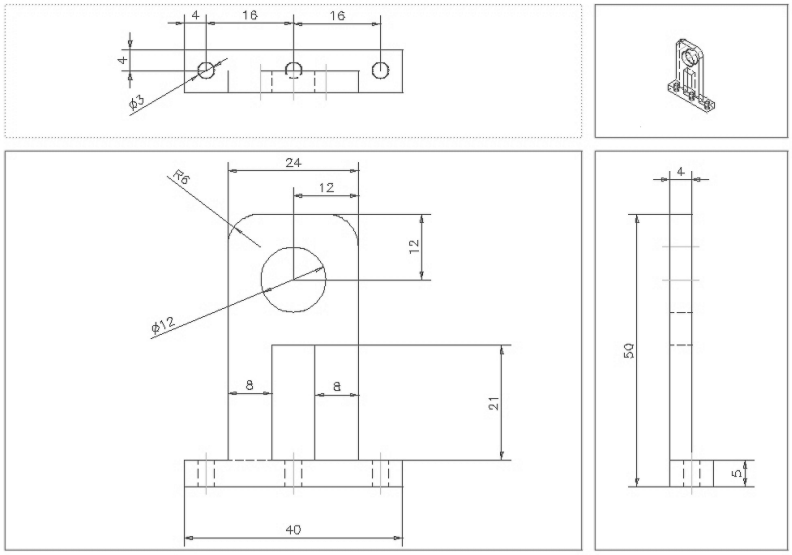

Figure B.2: Short bearing support column

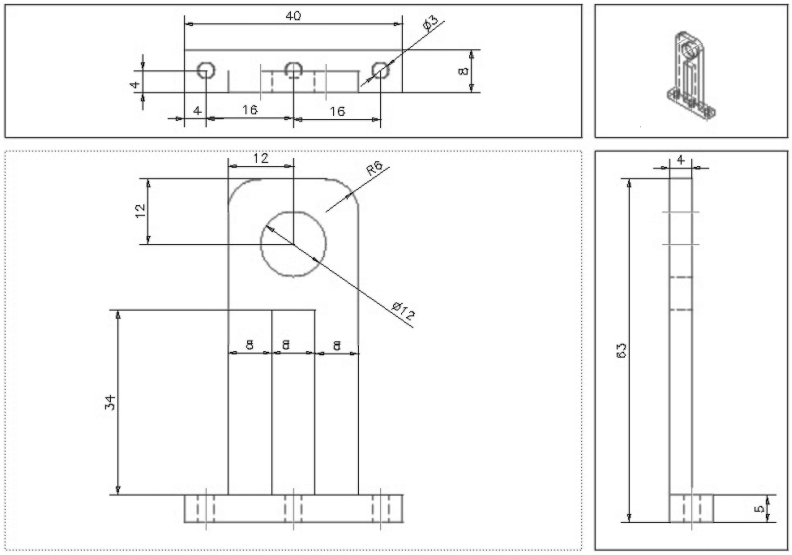

Figure B.3: Long bearing support column

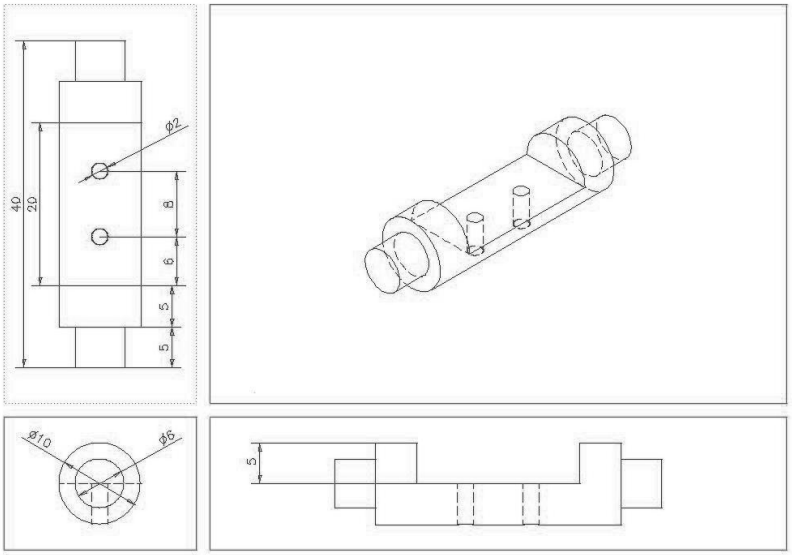

Figure B.4: Beam support rod

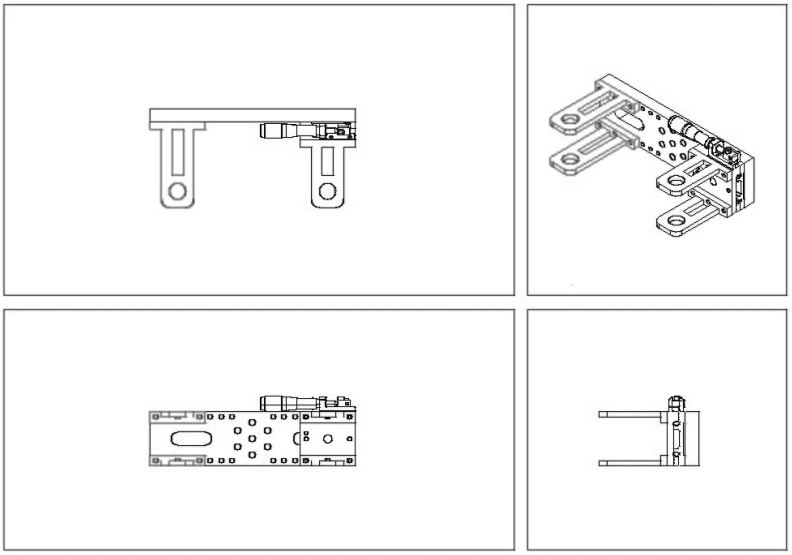

Figure B.5: Testing jig assembly drawing

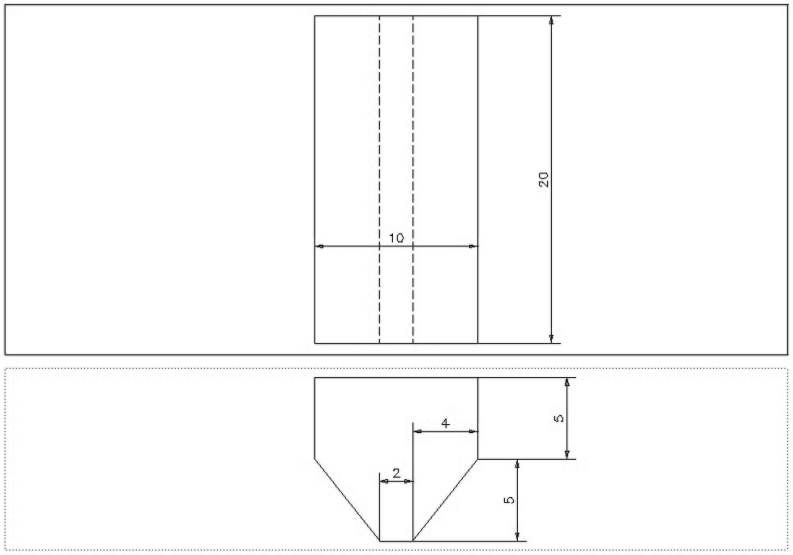

Figure B.6: Mass drawing